Design and fabrication of mid-IR plasmonic materials based on highly doped III-V semiconductors

Mohammad Esmail Aryaee Panah

A dissertation submitted in partial fulfilment of the requirements for the degree of

Doctor of Philosophy to

Department of Photonics Engineering

Technical University of Denmark

DTU Fotonik
Department of Photonics Engineering

Project period:	February 2014 to May 2017
Main supervisor:	Assoc. Prof. Andrei V. Lavrinenko
Co-supervisor:	Dr. Elizaveta S. Semenova
PhD. defense committee:	Assoc. Prof. Kresten Yvind, Department of Photonics Engineering, Technical University of Denmark
	Prof. Nader Engheta, Department of Electrical and Systems Engineering, University of Pennsylvania
	Assoc. Prof. Vladimir Bordo, Mads Clausen Institute, University of Southern Denmark

ABSTRACT

Plasmonics is one of the important fields in photonics which deals with studying and utilizing the collective oscillations of the free electrons' gas in a conductive material. These oscillations, which are known as plasmons, can be excited by an external electromagnetic field, resulting in an enhanced field that is confined to the surface of the conductive material and propagates along it in form of a surface wave which is known as surface plasmon polariton (SPP). Due to the strong enhancement and subwavelength confinement of the electromagnetic field, SPPs have many applications such as SPP enhanced photovoltaics, sensing, Raman spectroscopy and subwavelength waveguiding. Noble metals such as gold and silver are considered as traditional plasmonic materials for the visible range due to their abundant free electrons, but they suffer from high losses and poor confinement to the surface in the infrared (IR) range. Highly doped semiconductors can be considered as alternative plasmonic materials for the IR range which benefit from lower losses and tunability of the optical properties via adjusting the free carrier concentration. InP is one of the most important materials for optoelectronics as a direct bandgap semiconductor, which can also be regarded as a low loss alternative plasmonic material for the mid-IR range.

In this thesis silicon doped indium phosphide (InP:Si) is investigated as an alternative plasmonic material for the mid-IR range. The InP films are grown by metal-organic vapor phase epitaxy (MOVPE). Effect of the growth conditions, namely the precursors' fluxes ratio, on the electrical and optical properties of InP:Si in the wavelength range from 3 to 40 μm is studied. Carrier concentration of up to 3.9×10^{19} cm^{-3} is achieved by optimizing the growth conditions. The dielectric function, effective mass of electrons and the plasma frequency are all determined by Fourier transform infrared spectroscopy (FTIR), for different carrier density levels. The plasma frequency can be tuned effectively via doping from 18.43 to 50.5 THz. Based on the experimental results, a semi-empirical formula for the plasma frequency is derived.

The retrieved permittivity is then used to simulate SPPs propagation on flat and structured surfaces, and the simulation results are verified in direct experiments. SPPs at the top and bottom interfaces of the grown epilayer are excited by the prism coupling method. A high-index Ge hemispherical prism provides efficient coupling conditions of SPPs on flat surfaces and facilitates acquiring their dispersion diagrams. Diffraction into symmetry-prohibited diffraction orders stimulated by the excitation of SPPs is observed

in a periodically structured epilayer. Characterization shows good agreement between the theory and experimental results and confirms that highly doped InP is an effective plasmonic material aiming it for applications in the mid-IR wavelength range. Comparison to other semiconductors shows superior plasmonic performance of InP:Si in terms of the propagation length and confinement.

In order to demonstrate one of the novel applications of semiconductors in the mid-IR range, optically induced forces exerted upon a semi-insulating InP waveguide suspended above a highly doped InP:Si substrate are investigated in three different regimes: in the epsilon-near-zero (ENZ) case, with excitation of SPPs and phonons. An order of magnitude amplification of the force is observed when light is coupled to SPPs, and three orders of magnitude amplification is achieved in the phonon excitation regime. In the ENZ regime, the force is found to be repulsive and higher than that in a dielectric waveguide. Low losses in InP:Si result in a big propagation length. The induced deflection can be detected by measuring the phase change of the light when passing through the waveguide, which enables all-optical functioning, and paves the way towards integration and miniaturization of micro-cantilevers. In addition, tunability of the ENZ and the SPP excitation wavelength ranges, via adjusting the carrier concentration, provides an extra degree of freedom for designing MEMS devices.

Resumé

Plasmonics er et af de vigtige områder inden for fotonik, der beskæftiger sig med at studere og udnytte de kollektive oscillationer af fri elektron gas i et ledende materiale. Disse oscillationer, der er kendt som plasmoner, kan exciteres af et eksternt elektromagnetisk felt, hvilket resulterer i et forstærket felt, som er bundet til overfladen af det ledende materiale og udbredes i form af en overfladebølge, der er kendt som overflade plasmon polariton (SPP). På grund af den udtalte forstærkning og sub-bølgelængde binding af det elektromagnetiske felt har SPP'er mange anvendelser, bland andet SPP forbedret fotovoltaik, sensing, Raman spektroskopi og sub-bølgelængde bølgeledning. Ædelmetaller som guld og sølv betragtes som traditionelle plasmoniske materialer til det synlige område på grund af mængden af deres frie elektroner, men de lider af store optiske tab og et dårligt bindeevne til overfladen i IR-området. Stærkt doterede halvledere kan betragtes som alternative plasmoniske materialer til IR-området, der drager fordel af de lavere optiske tab og evnen til at tune de optiske egenskaber via en justering af den frie bærerkoncentration. InP er et af de vigtigste materialer til optoelektronik som en direkt båndgab halvleder, hvilken også kan betragtes som et alternativt plasmonisk materiale med de lave optiske tab i mid-IR området.

I denne afhandling undersøges siliciumdoteret indiumphosphid (InP:Si) som et alternativt plasmonisk materiale til mid-IR området. InP tynde film dyrkes ved hjælp af metalorganisk dampfase epitaksi (MOVPE). Effekten af vækstbetingelser, nemlig precursor fluxforhold, på InP:Si's optiske og elektriske egenskaber i bølgelængdeområdet fra 3 til 40 μm undersøges. Bærerkoncentration på op til 3,9 × 1019 cm-3 opnås ved at optimere vækstbetingelserne. Den dielektriske funktion, den effektive masse af elektroner og plasmafrekvensen er bestemt ved hjælp af Fourier transform-infrarødspektroskopi (FTIR) for forskellige bærertæthedsniveauer. Plasmafrekvensen kan indstilles effektivt via en dotering fra 18,43 til 50,5 THz. Baseret på eksperimentelle resultater udledes en semi-empirisk formel for plasmafrekvensen.

Den rekonstruerede permittivitet bruges derefter til at simulere SPP'er udbredelse på flade og strukturerede overflader, og simuleringsresultaterne er verificeret i direkte eksperimenter. SPP'er ved top- og bundgrænsefladerne af det dyrkede epilayer exciteres af prismekoblingen. Et højt indeks Ge halvkugleformet prisme giver effektive bindingsbetingelser for SPP'er på flade overflader og letter at skaffe deres

dispersionsdiagrammer. Diffraktion i symmetriforbudte diffraktionsordrer som er stimuleret ved excitation af SPP'er, observeres i et periodisk struktureret epilayer. Karakterisering viser en god overensstemmelse mellem teorien og eksperimentelle resultater og bekræfter, at højdoteret InP er et effektivt plasmonisk materiale, der sigter mod applikationer i mid-IR bølgelængdeområdet. Sammenligning med andre halvledere viser en overlegen plasmonisk optræden af InP:Si med hensyn til udbredelseslængde og bindeevne.

For at demonstrere en af de hidtil ukendte anvendelser af halvledere i mid-IR-området, blev optisk inducerede kræfter, udøvet på en halvisolerende InP-bølgeleder suspenderet over et højt doteret InP:Si-substrat, undersøgt i tre forskellige regimer: i epsilon-nær-Zero (ENZ) tilfælde, med excitation af SPP'er og fononer. En kraft forstærkning af en størrelsesorden observeres, når lyset er bundet til SPP'er, og der opnås en forstærkning i tre størrelsesordener i phonon excitationsregimet. I ENZ-regimet er kraften fundet at være frastødende og højere end den er i en dielektrisk bølgeleder. Lave optiske tab i InP:Si er årsagen til en stor udbredelseslængde. Den inducerede afbøjning kan detekteres ved at måle faseændringen af lyset, når den passerer gennem bølgelederen, hvilket muliggør all-optisk funktionalisering og baner vejen for integration og miniaturisering af mikro-cantilevers. Derudover, giver evnen til at tune ENZ og SPP excitations bølgelængder via justering af bærekoncentrationen, en ekstra grad af friheden til at designe MEMS-strukturer.

PREFACE

This thesis is submitted to the Department of Photonics Engineering, Technical University of Denmark, as partial fulfillment of the requirements for obtaining a Doctor of Philosophy degree in Photonics Engineering. Majority of the content that is presented here is based on the work which was carried out in the Metamaterials group at DTU Fotonik under the supervision of Prof. Andrei V. Lavrinenko and Dr. Elizaveta S. Semenova, from February 2014 to April 2017. The nanofabrication parts were conducted in the cleanroom facility at the National Center for Micro- and Nanofabrication (DTU Danchip). Some of the measurements were performed at the Department of Energy Conversion and Storage of the Technical University of Denmark, as well as St. Petersburg Academic University, Nizhniy Novgorod State University, and the Institute for Physics of Microstructures at Nizhniy Novgorod, Russia.

This project is mainly financed by the internal PhD. scholarship of the Technical University of Denmark and partially supported by the FP7-PEOPLE-2013-IRSES project HyMeCav (No. 612564).

Mohammad E. Aryaee Panah

April 2017, Lyngby, Denmark

ACKNOWLEDGEMENT

First and foremost, I would like to thank my supervisors, Prof. Andrei V. Lavrinenko and Dr. Elizaveta S. Semenova, without whom the accomplishment of this work was not possible. I also would like to appreciate the kind help and support from all of the members of the Metamaterials and Nanophotonic Devices groups, especially Dr. Osamu Takayama for doing the experiments with the Ge prism and for his useful consultations, Prof. Kresten Yvind for his efforts regarding the proper function of the MOVPE system, Dr. Luisa Ottaviano for her valuable suggestions regarding the fabrication of the plasmonic grating, Dr. Evgeniy Shkondin for editing the Danish abstract of the thesis, Prof. Sanshui Xiao and Dr. Bo-Hong Li for their help in FTIR measurements, Dr. Li Han for doing the Hall-effect measurements, Dr. Kion Norrman for doing the TOF-SIMS measurements, Prof. Sergey Morozov and Dr. Konstantin Kudryavtsev for their efforts in doing diffraction measurements on the InP:Si grating, Dr. Alexey Nadtochiy and Prof. Alexey Zhukov for doing Hall-effect measurements, Dr. Peixiong Shi and Jonas Michael-Lindhard for their efforts regarding SIMS measurements, and Dr. Peter Jesper Hanberg for his help in doing ECV measurements. I also would like to thank my friend Dr. Alireza Taghizadeh for the valuable discussions that we had during our coffee breaks.

I wish to use this opportunity to thank the teachers who contributed the most in my life; they taught me to talk, walk and love: my father Ali Mohammad, and my mother Mahboubeh.

Last but not least, I would like to express my special gratitude to my lovely wife Nadia, with whom I shared all my happy and sad moments during the past few years, and she was the one who gave me courage to go on.

List of Publications

Journal publications

1. **M. E. Aryaee Panah**, A. V. Lavrinenko, and E. S. Semenova, "Enhancing optical forces in InP-based waveguides," [Accepted for publication in *Scientific reports*].
2. E. Shkondin, O. Takayama, **M. E. Aryaee Panah**, P. Liu, P. V. Larsen, M. D. Mar, F. Jensen, and A. V. Lavrinenko, "Large-scale high aspect ratio Al-doped ZnO nanopillars arrays as anisotropic metamaterials," *Optical Materials Express* **7**(5), 1606-1627 (2017).
3. **M. E. Aryaee Panah**, O. Takayama, S. V. Morozov, K. E. Kudryavtsev, E. S. Semenova, and A. V. Lavrinenko, "Highly doped InP as a low loss plasmonic material for mid-IR region," *Optics Express* **24**(25), 29078-29089 (2016).
4. **M. E. Aryaee Panah**, L. Han, K. Norrman, N. Pryds, A. Nadtochiy, A. E. Zhukov, A. V. Lavrinenko, and E. S. Semenova "Mid-IR optical properties of silicon doped InP," [Submitted to *Optical Materials Express*].
5. O. Takayama, E. Shkondin, A. Bodganov, **M. E. Aryaee Panah**, K. Golenitskii, P. Dmitriev, T. Repän, R. Malureanu, P. Belov, F. Jensen, and A. V. Lavrinenko, "Mid-infrared directional surface waves on a high aspect ratio nano-trench platform," arXiv:1704.06108v1 [Submitted to *Light: Science & Applications*].

Conference proceedings

1. O. Takayama, E. Shkondin, **M. E. Aryaee Panah**, T. Repän, R. Malureanu, F. Jensen, A. Lavrinenko, "Conductive oxides trench structures as hyperbolic metamaterials in mid-infrared range," *14th International Conference of Near-Field Optics, Nanophotonics and Related Techniques*, Hamamatsu, Japan (2016).
2. **M. E. Aryaee Panah**, L. Han, D. Valbjørn Christensen, N. Pryds, A. Lavrinenko, E. Semenova, "Silicon doped InP as an alternative plasmonic material for mid-infrared," *Proceedings of 41st International Conference on Infrared, Millimeter and Terahertz Waves*, Copenhagen (2016).
3. **M. E. Aryaee Panah**, L. Ottaviano, E. Semenova, A. Lavrinenko, "Surface plasmons on highly doped InP," *Proceedings of 10th International Congress on Advanced Electromagnetic Materials in Microwaves and Optics*, Crete, Greece (2016).
4. O. Takayama, E. Shkondin, **M. E. Aryaee Panah**, T. Repän, R. Malureanu, F. Jensen, A. Lavrinenko, "Surface waves on metal-dielectric metamaterials," *Proceedings of 18th International Conference on Transparent Optical Networks*, Italy (2016). [Invited paper]
5. O. Takayama, E. Shkondin, **M. E. Aryaee Panah**, T. Repän, R. Malureanu, F. Jensen, A. Lavrinenko, "Surface waves on metamaterials interfaces," *Proceedings of 10th International Congress on Advanced Electromagnetic Materials in Microwaves and Optics*, Crete, Greece (2016). [Invited paper]
6. A. V. Lavrinenko, A. Andryieuski, S. Zhukovsky, O. Takayama, E. Skhondin, **M. E. Aryaee Panah**, R. Malureanu, F. Jensen, "Hyperbolic metamaterials with

complex geometry," *The 7th International Conference on Metamaterials, Photonic Crystals and Plasmonics*, Malaga, Spain (2016). [Invited paper]

7. **M. E. Aryaee Panah**, S. Xiao, A. Lavrinenko, E. Semenova, "Overcoming doping limits in MOVPE grown n-doped InP for plasmonic applications," *Proceedings of EWMOVPE XVI*, Lund, Sweden (2015).

Table of contents

1. INTRODUCTION

Human being has always tried to find (or make up) simple answers to complicated questions which either affect or do not have any direct impact on his daily life. The reason for finding (or making up) answers to the questions with no impact on the daily life is "*peace of mind*". Ignorance makes us feel uncomfortable. That is why most of the people always make up simple stories to answer the most complicated (or unanswerable) questions and never challenge their own stories afterwards. This has led to "*religion*"; a collection of reasoning which is based on unexaminable "*facts*". The reason for seeking answers to the questions which can affect our daily life is simple: we want to "*predict*" and "*utilize*" the nature, in order to facilitate our daily life.

"*Natural sciences*" are indeed a collection of "*models*" which are usually based on examinable and observable facts. These models which are developed to answer both of the above mentioned types of questions are valid as long as they can explain the observations and can be replaced with alternative models whenever they fail to do so.

Light is one of the most important constituents of life evolution on earth. Sunlight warms the planet to a proper-to-live temperature, makes weather patterns and helps plants to make food and oxygen for us. Besides, light is our primary tool for understanding the world around us. Human being has always tried to explain light-related phenomena and find out about the nature of light. In other words, he has always been seeking for a proper model for light. Some ancient Greek philosophers believed that the light rays which come out of our eyes help us to see the objects around us, while some others believed that the light which comes from the objects enters our eyes. The first person who is known to study the light using a scientific method is Ibn al-Haytham. He used carefully planned experiments to verify theories and believed that light is an independent part of the vision. He divided the objects into two groups: those which emit light and those which reflect it. This is one of the basics of modern optics. Isaac Newton believed that light is a stream of particles, and his experiments with a

prism revealed that the white light is a mixture of all of the rainbow colors. Thomas Young's experiments on the interference of light in 1800 showed the wave nature of light. He also proposed that different colors of light have different wavelengths. James Clerk Maxwell's studies on the electromagnetic waves predicted that these waves travel with a speed very close to the speed of light, which had already been measured. Based on this, he proposed that light must be an electromagnetic wave. Nevertheless, this could not explain the photoelectric effect, and Albert Einstein in 1905 proposed that the photoelectric effect is caused by absorption of quanta of light which are now known as "*photons*" [1].

Many of the electronic properties of materials can be described by free movement of single electrons in a periodic array of atoms. Another approach is to consider a gas of free electrons and a background of positive ions. In certain conditions, light can transfer its energy to the free electrons' gas resulting in longitudinal density fluctuations of it. These fluctuations which can propagate inside the material are called plasma oscillations and a quantum of these oscillations is called "*plasmon*" [2].

1.1. Plasmonics

Plasmonics is a growing field in photonics which deals with excitation of the collective oscillations of free charges, known as plasmons, in a conductive material, resulting in a drastically enhanced electromagnetic field in the vicinity of the material's interface. Plasmons can be excited by exposing subwavelength conductive particles to an external electromagnetic field, resulting in localized plasmon-polaritons (LPP) or by coupling the external field to the oscillating charges near the surface of the material, resulting in a highly confined surface wave propagating along the interface between the conductive material and the dielectric media, known as surface plasmon-polaritons (SPP) [3]. High confinement of this enhanced field provides higher local optical density of states and leads to applications such as plasmon-enhanced photovoltaics [4], biosensing [5], Raman spectroscopy [6] and photocatalysis [7]. Furthermore, SPP's enable subwavelength spatial confinement of the light, due to the fact that their dispersion curve lies on the right side of the light line. This very important property of SPP's is used in many fields including subwavelength waveguiding [8] and optical superlenses [9].

Plasmons were first studied and utilized in the visible and near-infrared (near-IR) ranges [10]. Similarly mid-IR plasmonics can contribute to many applications by means of intensely localized electric field at the interface and enhanced light-matter interactions. Plasmonics for the mid-IR wavelength region offers unique functionalities for thermal imaging, due to the peak emission wavelength for the temperatures ranging

from 200-1400 K and the atmospheric transmission window both lying in the mid-IR. There are perspective chemo-sensing applications [11-14] owing to the fact that many molecules have vibrational and rotational absorption bands which can serve as fingerprints to detect and determine molecular species in this wavelength range. This is likely to affect all fields from personalized health care to industrial quality control [10]. In addition, the fast growing field of graphene plasmonics and related 2D materials operates in this wavelength regime as well [15,16]. Moreover, mid-IR can be considered as a host for metamaterials as they move from terahertz to visible region, which benefits from easier fabrication of subwavelength structures [10].

1.2. Alternative plasmonic materials

Metals such as Au, Ag and Cu are considered as traditional plasmonic materials for the visible range. However, when it comes to the mid- and far-IR ranges, metals suffer from high optical losses and poor spatial confinement of SPP's. In addition, CMOS incompatibility of metals is a challenge in the fabrication process of the nanophotonic devices.

Alternative plasmonic materials such as graphene, ceramics, conductive oxides and semiconductors are introduced to address these shortcomings [17,18]. Semiconductors play a key role in this context, owing to their high mobilities and low optical losses [19]. In addition, tunability of their optical and plasmonic properties via doping or charge depletion [20] adds an additional degree of freedom for engineering photonic device elements. Indium phosphide (InP) as a direct bandgap III-V semiconductor is one of the most common materials in optoelectronic applications and telecom photonics. Highly doped InP can be considered as a plasmonic material with superior plasmonic properties compared to most other semiconductors in the mid-IR range [21]. Furthermore, easy integration and compatibility with conventional III-V optoelectronic devices and their fabrication processes makes InP a promising candidate as a plasmonic material aiming it for mid-IR.

1.3. Structure of the dissertation

In this thesis, effect of the growth conditions on the free carrier concentration of silicon doped InP is experimentally investigated. Optical and electrical properties of the grown InP:Si is determined and used to simulate the excitation of SPP's on the surface of highly doped InP:Si. Simulations are verified in direct experiments, confirming the existence of SPP's and the accuracy of the retrieved optical properties. Finally, the

retrieved optical properties of InP:Si are used to simulate gigantic optical forces in InP-based waveguides with applications in microelectromechanical systems (MEMS).

The thesis is organized as follows:

Chapter 1 presents the motivation of this work and a short general overview on plasmonics and alternative plasmonic materials.

Chapter 2 starts with a technical review on metal-organic vapor phase epitaxy (MOVPE) technology, and continues to investigation of MOVPE growth of highly doped InP:Si and the effect of growth conditions on the free carrier concentration.

Chapter 3 starts with a technical introduction and literature review on the optical properties of InP from the ultraviolet (UV) to the IR frequency range, and continues with describing the procedure which is used in this work to retrieve the optical properties of InP:Si. Optical properties of the grown samples with different carrier concentrations are presented and the performance of InP:Si as a plasmonic material is compared with other semiconductors.

Chapter 4 starts with a technical introduction and literature review on SPPs and different materials which are studied in this context. Afterwards the excitation of SPPs on InP:Si surface is theoretically studied and the experimental results are presented and compared to the theory.

Chapter 5 starts with a technical introduction to optomechanics and continues with calculating the optically induced forces which are exerted on waveguides adjacent to a substrate. Afterwards, optical properties of InP:Si which are experimentally retrieved in the previous chapters are used to calculate the optically induced forces in InP-based waveguides in different frequency regimes.

Chapter 6 presents a summary of the thesis and gives an outlook on possible directions for further research, based on the results of this dissertation.

Appendix A presents the computer program which is developed to calculate the reflectance spectra of multilayer structures under normal incidence.

Appendix B presents the computer program which is developed to calculate the reflectance spectra of multilayer structures under oblique incidence.

Appendix C presents the computer program which is developed to find the permittivity of InP:Si by fitting the calculated reflectance spectra of the samples to the measured ones.

Appendix D presents the results of optical characterization of hyperbolic metamaterials which is done using the methods which are developed in the previous chapters.

References

1. www.light2015.org
2. H. Raether, *Surface Plasmons on Smooth and Rough Surfaces and on Gratings* (Springer-Verlag, 1988).
3. S. A. Maier, *Plasmonics: Fundamentals and Applications* (Springer, 2007).
4. H. A. Atwater and A. Polman, "Plasmonics for improved photovoltaic devices," Nat. Mater. **9**(3), 205–213 (2010).
5. M. Bauch, K. Toma, M. Toma, Q. Zhang, and J. Dostalek, "Plasmon-enhanced fluorescence biosensors: a review," Plasmonics **9**(4), 781–799 (2014).
6. M. R. Philpott, "Effect of surface plasmons on transitions in molecules," J. Chem. Phys. **62**(5), 1812-1817 (1975).
7. S. Shuang, R. Lv, Z. Xie, and Z. Zhang, "Surface plasmon enhanced photocatalysis of Au/Pt-decorated TiO_2 nanopillar arrays," Sci. Rep. **6**, 26670 (2016).
8. J. A. Dionne, L. A. Sweatlock, H. A. Atwater, and A. Polman, "Planar metal plasmon waveguides: frequency-dependent dispersion, propagation, localization, and loss beyond the free electron model," Phys. Rev. B **72**(7), 075405 (2005).
9. J. B. Pendry, "Negative refraction makes a perfect lens," Phys. Rev. Lett. **85**(18), 3966 (2000).
10. R. Stanley, "Plasmonics in the mid-infrared," Nat. Photon. **6**(7), 409-411 (2012).
11. J. N. Anker, W. P. Hall, O. Lyandres, N. C. Shah, J. Zhao, and R. P. Van Duyne, "Biosensing with plasmonic nanosensors," Nat. Mater. **7**(6), 442-453 (2008).
12. J. Homola, "Surface plasmon resonance sensors for detection of chemical and biological species," Chem. Rev. **108**(2), 462-493 (2008).
13. S. Law, V. Podolskiy, and D. Wasserman, "Towards nano-scale photonics with micro-scale photons: The opportunities and challenges of mid-infrared plasmonics," Nanophotonics **2**(2), 103-130 (2013).
14. D. Rodrigo, O. Limaj, D. Janner, D. Etezadi, F. J. García de Abajo, V. Pruneri, and H. Altug, "Mid-infrared plasmonic biosensing with graphene," Science **349**(6244), 165-168 (2015).
15. A. N. Grigorenko, M. Polini, and K. S. Novoselov, "Graphene plasmonics," Nat. Photon. **6**(11), 749–758 (2012).
16. J. D. Caldwell, I. Vurgaftman, J. G. Tischler, O. J. Glembocki, J. C. Owrutsky, and T. L. Reinecke, "Atomic-scale photonic hybrids for mid-infrared and terahertz nanophotonics," Nat. Nanotech. **11**(1), 9-15 (2016).
17. G. V. Naik, and A. Boltasseva, "Ceramic plasmonic components for optical metamaterials," in *Proceedings of the Conference on Lasers and Electro-Optics: Laser Science to Photonic Applications, CLEO* (2011), 5951597.
18. Y. Zhong, S. D. Malagari, T. Hamilton, and D. Wasserman, "Review of mid-infrared plasmonic materials," J. Nanophotonics **9**(1), 093791 (2015).
19. A. Boltasseva, "Empowering plasmonics and metamaterials technology with new material platforms," MRS Bull. **39**(5), 461-468 (2014).

20. K. Anglin, T. Ribaudo, D. C. Adams, X. Qian, W. D. Goodhue, S. Dooley, E. A. Shaner, and D. Wasserman, “Voltage-controlled active mid-infrared plasmonic devices,” J. Appl. Phys. **109**(12), 123103 (2011).
21. M. E. Aryaee Panah, O. Takayama, S. V. Morozov, K. E. Kudryavtsev, E. S. Semenova, and A. V. Lavrinenko, “Highly doped InP as a low loss plasmonic material for mid-IR region,” Opt. Express **24**(25), 29077-29088 (2016).

2. MOVPE GROWTH OF HIGHLY DOPED InP:Si

2.1. Introduction to MOVPE

Metal-organic vapor phase epitaxy (MOVPE) is a powerful and flexible technology for epitaxial growth of compound semiconductors. In this method, substrate wafers are placed on a heated carrier disk which, in most of the cases, rotates inside the growth reactor chamber. Precursor gasses are injected into the growth chamber, chemically react on the surface of the substrate and afterwards the byproducts are dragged towards the outlet exhaust (Fig. 2.1). MOVPE was introduced at the beginning of 1970s [1] dealing primarily with the deposition of GaAs on insulating substrates and subsequently evolved for deposition of all of the III-V compounds [2]. The term metal-organic (or organo-metallic) is included in the name, since at least one of the constituent materials of the epilayer is transported using room temperature vapors of organometallic compounds. MOVPE has the capability of growing the widest variety of III-V semiconductors among all of the epitaxial growth techniques, including molecular beam epitaxy (MBE), liquid and vapor phase epitaxy (LPE and VPE) [2]. One of the most important features of this technique is the ability of growing different compounds in the same run. MOVPE is now widely used in fabrication of electronic and photonic devices due to the ability of instantaneous control over the partial pressure and flow rates of the precursor gasses which results in well-defined growth of a wide variety of semiconductor materials [3].

Alkyls of group III metals and hydrides of group V elements are used as the precursors for growing III-V semiconductors. A carrier gas (usually H_2 or N_2) containing dilute vapors of these chemicals in near room temperature is injected into the

chamber through the inlet flanges and reacts near the hot surface of the substrate. The general form of the reaction for III-V semiconductors is described by [2]

$$R_3M + EH_3 \rightarrow ME + 3RH \tag{2.1}$$

in which M is the group III metal, R is the alkyl and E is the group V element. If more than one group III alkyls are present in the chamber, for example R_3M', the deposited solid becomes an alloy of the type $M_{1-x}M'_xE$. Composition of the alloy (value of *x*) is determined by the relative reaction rates for the two alkyls.

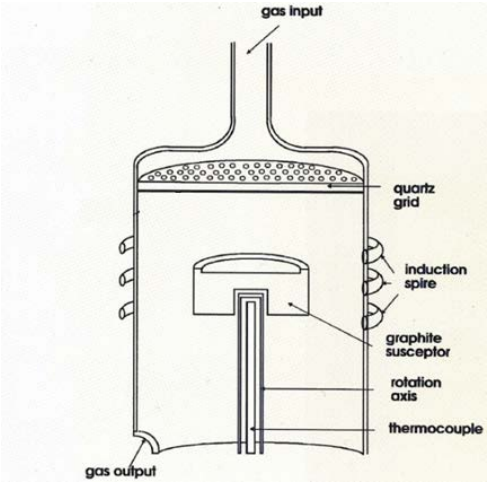

Fig. 2.1 Schematic of the MOVPE growth chamber

The growth process starts with the mass transfer of the precursors towards the growth surface, and proceeds with their reaction on or close to the hot surface, incorporation of the new material on the growth front and removal of the byproducts [4]. There is normally an excess amount of the group V hydride in the growth chamber, therefore the growth rate is mainly dominated by the partial pressure of the group III alkyls and can be expressed by a linear relation as [3]

$$g = A_1 p_{R_3M} + A_2 p_{R_3M'} \tag{2.2}$$

where p_{R_3M} and $p_{R_3M'}$ are the partial pressures of the group III precursors.

One of the problems that may occur during the growth is the reaction between the precursors in the cold gas, before arriving at the substrate. In this case, the reaction (2.1) will proceed as [2]

$$R_3M + EH_3 \rightarrow R_3M - EH_3 \tag{2.3}$$

in which M and E elements have made bonds before dissociation of the precursors. If reaction (2.3) proceeds to form non-volatile compounds, the precursors can be depleted from the reactants which may result in decreasing the growth rate or changing the composition of the deposited alloy [2].

Figure 2.2 shows a schematic of the gas handling system in MOVPE machine. Metal-organic precursors are kept in temperature controlled bubblers. The carrier gas (here Pd-purified hydrogen) is introduced into the precursor's container and leaves it saturated with the precursor's vapor. Mass flow controllers are used to enable instantaneous and continuous control over the flow of the saturated vapor which will be diluted and carried towards the reactor by an H_2 push flow. Hydrides are introduced as pure gasses or as a mixture with H_2. The susceptor can be heated by radio frequency (RF) induction or resistance heating.

Mathematical modelling of the growth process in MOVPE is a very complicated task which involves deep understanding of the interplay between fluid dynamics, heat and mass transfer, chemical kinetics and crystal growth, and is a subject of ongoing research [5-8]. The carrier disk rotates inside the growth reactor chamber, transforming a laminar flow pattern of supplied precursor gasses into the circumferential flows and forms the so called boundary layer on top of the wafer surface. This boundary layer provides diffusion driven transport of precursors to the growing surface which results in uniform growth with a predictable rate. In addition the flow dynamics in a rotating disk reactor (RDR) prevents material from being deposited on the optical access windows of the chamber [3].

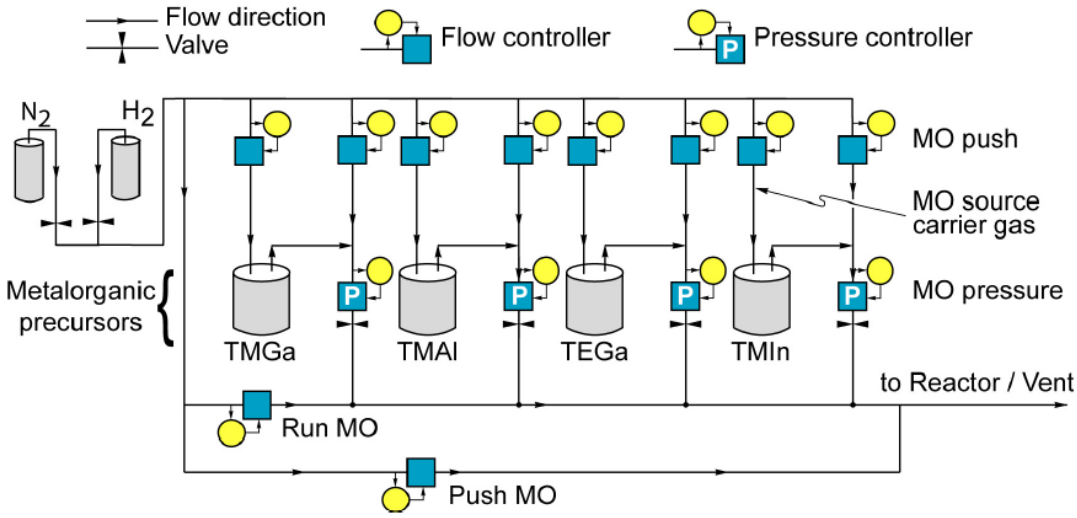

Fig. 2.2 Schematic of the gas handling system in MOVPE [9]

2.2. MOVPE growth of InP:Si

InP is a direct bandgap semiconductor with a face-centered cubic (zincblende) structure (Fig. 2.3), which is widely used in optoelectronic devices, as a platform for photonic integrated circuits [10], novel distributed feedback laser arrays [11], photodetectors

[12], vertical cavity surface emitting lasers (VCSELs) [13,14], and InP-based mid-infrared (mid-IR) light emitting diodes (LEDs) [15]. InP-based quantum well lasers offer spontaneous emission in the range from 2 to 3.9 μm and laser operation up to 2.7 μm [15]. Recently InP is used to fabricate novel single crystal phase nanowire quantum dots for single photon applications and quantum optics [16]. Apart from the above mentioned applications in optoelectronic devices, highly doped InP is recently investigated as an alternative plasmonic material for the mid-IR range, which has superior performance in comparison to traditional plasmonic metals and other semiconductors, owing to its lower losses [17].

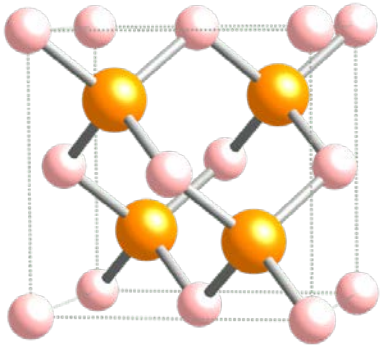

Fig. 2.3 Crystal structure of InP [By Ben Mills, www.wikipedia.org]

The first demonstration of MOVPE grown InP was by Manasevit and Simpson [2] in the early years of the development of this method. Trimethylindium (TMIn) and phosphine (PH_3) are usually used as the precursor gasses with their reaction on the hot surface of the substrate described by

$$In(CH_3)_3 + PH_3 \rightarrow InP + 3CH_4 \, . \qquad (2.4)$$

Existence of the parasitic reaction (2.3) for InP is reported by several authors but not observed by some others. In his review paper published in 1985, Ludowise concluded that this reaction may not be noticeable under the right growth conditions including the proper reactor geometry [2].

Free carrier concentration in the grown semiconductors is an important parameter which needs to be carefully controlled by choosing proper growth conditions such as ratio of the precursor gasses, growth temperature and the overall pressure of the growth chamber. Silicon is commonly used as a donor in MOVPE grown InP and effect of the growth conditions on its incorporation efficiency has been investigated [18-25]. In this regard, to the authors' knowledge, the highest reported carrier concentration in MOVPE grown InP:Si is 2.6×10^{19} cm^{-3} [26].

Nine InP:Si samples are grown on single-side polished (1 0 0) semi-insulating (SI) InP:Fe substrates and two samples are grown on single-side polished (1 0 0) n-

doped InP:S substrates. Low pressure MOVPE is used to grow the samples, with hydrogen (H_2) as the carrier gas, using PH_3, TMIn and disilane (Si_2H_6) as the precursors for phosphorus, indium and silicon respectively. The carrier disk rotates with 1000 rpm inside the growth reactor chamber. The growth conditions, namely the phosphorus to indium precursors' molar ratio and the disilane flux are adjusted, resulting in different free carrier concentrations.

Disilane is commonly used as the precursor for Si doping of MOVPE grown InP whose dissociation is described by a two-step process as

$$Si_2H_6 \rightarrow SiH_2 + SiH_4 \tag{2.5}$$
$$SiH_4 \rightarrow SiH_2 + H_2 \tag{2.6}$$

where Si in SiH_2 will react on the surface of the epilayer and contribute to doping. In temperatures below 700 °C, the decomposition efficiency of silane (SiH_4) is very low and therefore the Si incorporation rate is mainly determined by Eq. (2.5) [22]. The decomposition efficiency of disilane [Eq. (2.5)] is proportional to the temperature up to 610 °C (reported 625 °C in [19]) and mass transport limited above that. At this point increasing the disilane flux will increase the carrier concentration up to a threshold point above which the layer morphology will be deteriorated. The doping efficiency also slightly depends on the phosphine to TMIn molar ratio (V/III ratio). This proportional dependence is assumed to be a consequence of the reaction [22]

$$PH_3 + SiH_2 \leftrightarrows SiH_3PH_2 \tag{2.7}$$

which is dependent on the group V supply and can contribute to doping by incorporation of Si from SiH_3PH_2 into the growing epilayer.

Flux of TMIn, which is supplied from a solid source through a bubbler, is calculated as [3]

$$F_{\mathrm{TMIn}} = \frac{\epsilon\, F_{\mathrm{hydrogen}}\, p_{\mathrm{TMIn}}}{(p_{\mathrm{bubbbler\,total}} - p_{\mathrm{TMIn}})} \tag{2.8}$$

where F_{hydrogen} is the hydrogen flux, $p_{\mathrm{bubbbler\,total}}$ is the total overpressure within the bubbler (500 mbar), ϵ is the efficiency of the bubbler which can be assumed to be unity with a good accuracy and p_{TMIn} is the saturated vapor pressure of TMIn in the bubbler which can be calculated from [27]

$$p_{\mathrm{TMIn}} = 10^{\left(10.52 - \frac{3014}{T}\right)}\ [\mathrm{Torr}] \tag{2.9}$$

in which T is the bubbler temperature in kelvin (291 K for TMIn). Molar flux of TMIn can readily be calculated using F_{TMIn} and the ideal gas law.

Molar flux of PH_3, which is supplied directly from a gas source, is calculated from

$$F_M^{\mathrm{PH_3}} = F_{\mathrm{PH_3}} \frac{\rho_{\mathrm{PH_3}}}{M_{\mathrm{PH_3}}} \tag{2.10}$$

where $F_{\mathrm{PH_3}}$, $\rho_{\mathrm{PH_3}}$ and $M_{\mathrm{PH_3}}$ are the volume flux, density (in the standard temperature and pressure condition) and the molar mass of PH_3 respectively.

Using the appropriate values for the density and molar mass, Eq. (2.10) can also be used to calculate the molar flux of disilane, which is supplied as a 200 ppm diluted gas in hydrogen.

Free carrier concentration of the samples which are grown on a SI substrate (samples 1-9) is determined by Hall-effect measurement which is carried out at room temperature using the van der Pauw method with a variable magnet field (measured up to 1.5 T).

Hall-effect measurement cannot determine the free carrier concentration of an epilayer which is grown on a doped substrate (samples 10 and 11). Therefore for these two samples electrochemical capacitance-voltage (ECV) measurement method is used, in which a small area of the sample (a circle of around 0.5 mm diameter) is exposed to an electrolyte that slowly dissolves the sample by an electrochemical reaction. The free carrier concentration of the sample is consequently measured in different depths. More theoretical details about ECV measurement method can be found in [28].

All the samples are grown at 610 °C and an overall chamber pressure of 60 Torr. Table 2.1 summarizes the growth conditions and the resulting carrier concentration and mobility of the samples 1-9. Figure 2.4 shows the carrier concentration versus disilane to TMIn molar flux ratio for two groups of samples with different V/III molar ratios. Carrier concentration is proportional to disilane to TMIn molar flux ratio up to a threshold point where the excess Si precipitates on the surface of the sample and deteriorates it (Fig. 2.5). As explained above, higher V/III ratio results in slightly higher carrier concentration.

Table 2.2 summarizes the growth conditions and the free carrier concentration for samples 10 and 11. These results are presented separately from the results of samples 1-9 because of the different measurement techniques used.

Table 2.1 Growth parameters and the electrical properties of the samples 1-9

Sample	PH_3 flux [SCCM]	PH_3 flux $\times 10^{-2}$ [mol/min]	TMIn flux [SCCM]	TMIn flux $\times 10^{-5}$ [mol/min]	Disilane flux $\times 10^{-9}$ [mol/min]	Thickness [nm]	Free carrier concentration [$\times 10^{19}$ cm^{-3}]	Mobility [cm^2/V.s]
1	350	1.534	355	6.163	0.769	485	0.35	1490
2	250	1.096	407	7.066	2.696	570	0.86	723
3	250	1.096	407	7.066	4.623	533	1.71	893
4	250	1.096	407	7.066	5.392	531	1.94	901
5	250	1.096	407	7.066	6.164	536	2.35	480
6	350	1.534	347	6.024	5.253	475	2.7	821
7	350	1.534	347	6.024	6.935	651	3.09	689
8	350	1.534	355	6.163	7.319	516	3.39	749
9	350	1.534	347	6.024	7.319	503	3.87	671

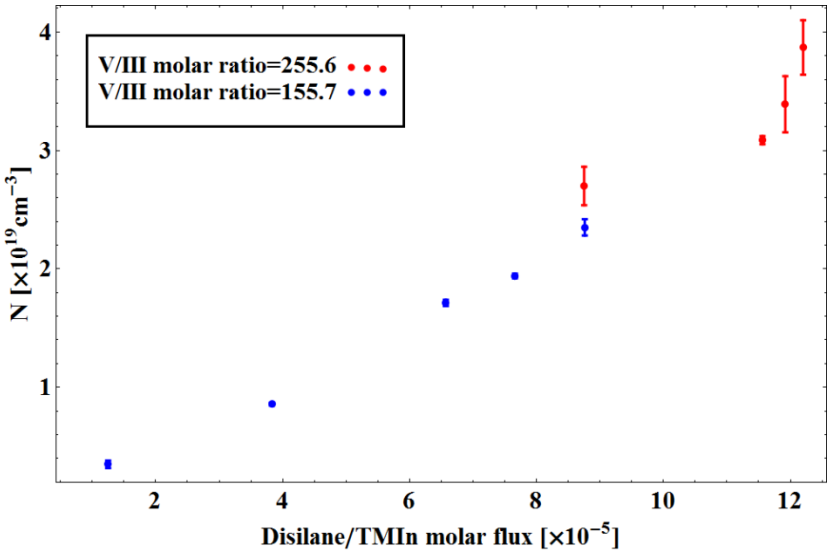

Fig. 2.4 Carrier concentration versus Si_2H_6/TMIn molar ratio for two different V/III molar ratios (samples 1-9)

Fig. 2.5 Differential interference contrast (DIC) optical microscope image of the deteriorated surface of a sample with Si_2H_6/TMIn molar ratio equal to 15.27×10^{-5}

Table 2.2 Growth parameters and the electrical properties of the samples 10 and 11

Sample	PH_3 flux [SCCM]	PH_3 flux $\times10^{-2}$ [mol/min]	TMIn flux [SCCM]	TMIn flux $\times10^{-5}$ [mol/min]	Disilane flux $\times10^{-9}$ [mol/min]	Thickness [nm]	N (ECV) $\times10^{19}$ [1/cm^3]
10	200	0.87	350	6.076	6.935	397	3.15
11	200	0.87	407	7.066	3.852	3080	2.7

2.2.1. Self-compensation in InP:Si

In order for the Si atoms to contribute as donors they should be incorporated into sub-lattice of the IIIrd group, but in some cases, Si atoms may be incorporated to sub-lattice of the Vth group and work as acceptors, or sit in the interstitial sites of the crystal. This phenomenon which is one of the barriers against high doping of InP is known as self-compensation [29].

The concentration of Si atoms is determined using time-of-flight secondary ion mass spectrometry (TOF-SIMS) and subsequently compared to the free carrier concentration in the grown samples. A reference sample with a known amount of ^{28}Si is required to calibrate the TOF-SIMS response to the concentration. In this regard "stopping and range of ions in matter" (SRIM) simulations are done to find the appropriate dose, energy and the resulting concentration profile for implantation of Si ions in an InP:S wafer consisting of 49.992% In, 49.992% P and 0.016% S. Atomic mass of Si is considered to be 27.977 amu. Figure 2.6(a) shows the simulated ions paths for 500 Si ions with 380 KeV energy and 7° tilt angle. Figures 2.6(b) and (c) show the ions range and atoms distribution respectively for 10000 ions considered in the

simulation. According to Fig. 2.6(b), a dose of 2×10^{15} Si atoms/cm^2 will result in the maximum Si concentration of 5.4×10^{19} cm^{-3} at 450 nm depth. An ion implanted sample with the above mentioned parameters is ordered from a commercial supplier, to be used as the reference sample for TOF-SIMS measurements. TOF-SIMS depth profiling analyses are performed on the grown InP:Si samples. The erosion rate is calculated to be 15.6 nm/min by measuring the resulting crater depth for the thickest epilayer using a Dektak 3030 surface profile measuring system (Sloan Technology Corp.) and relating the depth to the sputter time. The Si concentrations are extracted from depth profiles through the entire epilayer and the error bars are typically based on 50–100 in-depth measuring points.

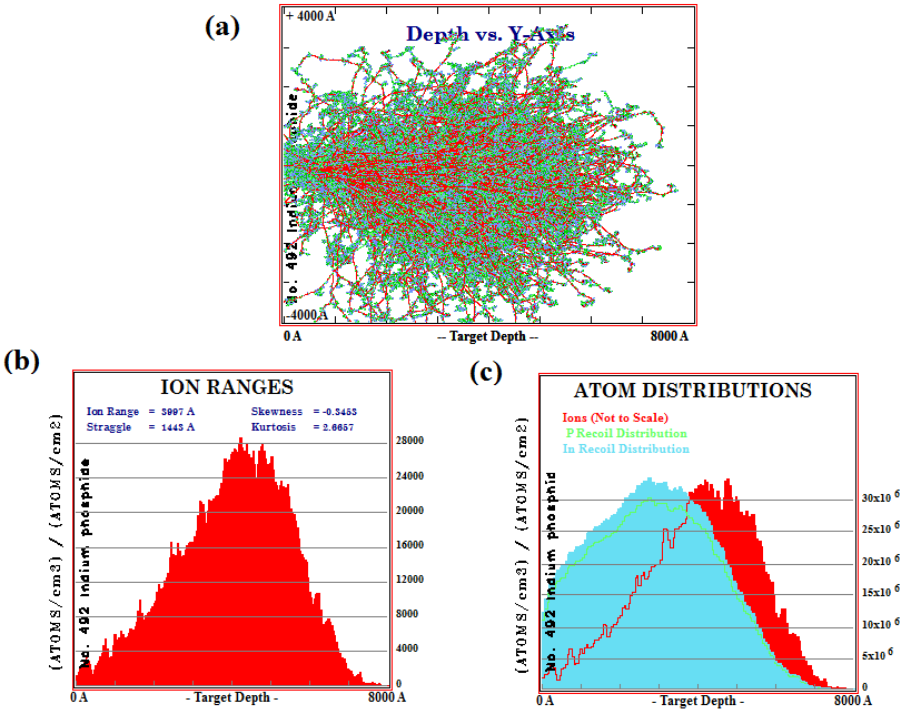

Fig. 2.6 SRIM simulation results for Si implantation in InP:S, (a) Ions paths for 500 ions, (b) ions range for 10000 ions, and (c) atoms distribution for 10000 ions

Figure 2.7 presents the TOF-SIMS depth profiles for all of the grown samples together with the ion implanted reference sample. Figure 2.8 shows the free carrier concentration measured by Hall-effect method versus the disilane to TMIn molar flux ratio, together with the Si concentration measured by TOF-SIMS analysis for samples 1-9. In all cases, the difference between the Si concentration measured by TOF-SIMS and the donors concentration measured by Hall-effect method is smaller than the error bars, which shows that the compensation ratio (ratio of the ionized acceptors to the ionized donor concentration) is smaller than the measurement limit.

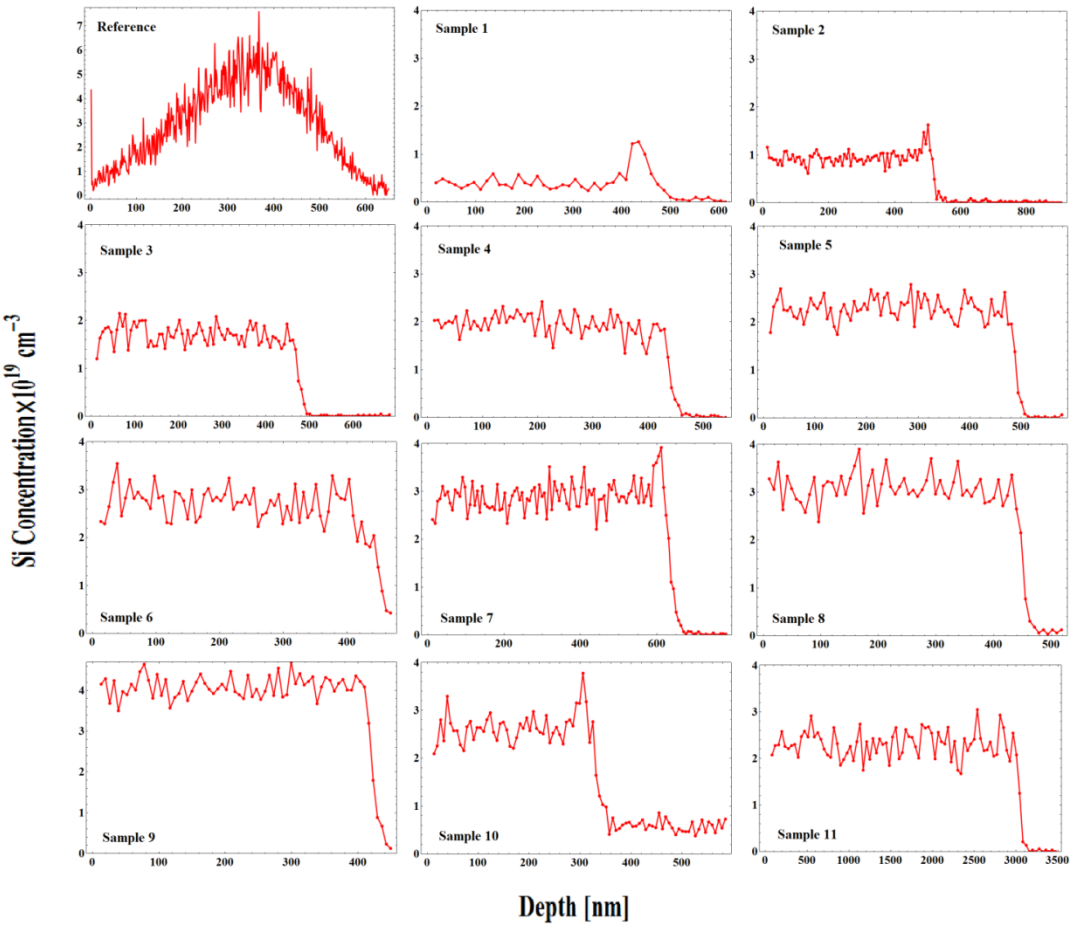

Fig. 2.7 Depth profile of the Si concentration in the samples measured by TOF-SIMS.

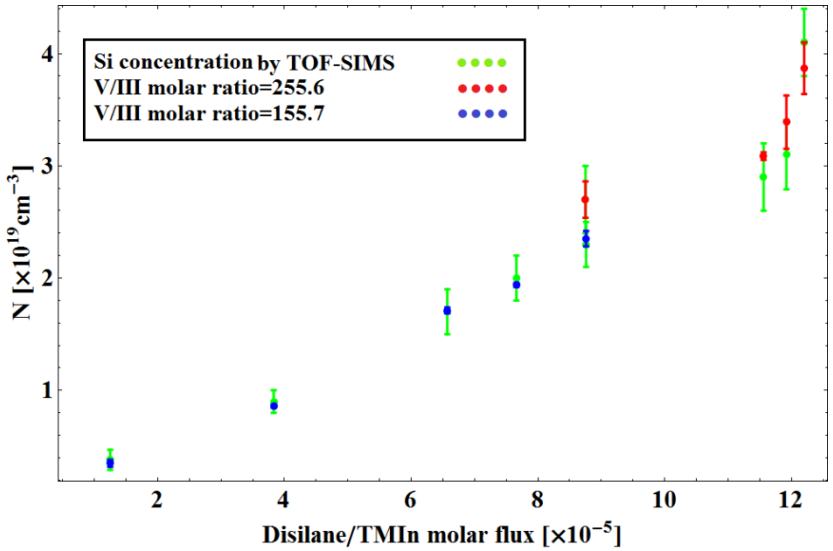

Fig. 2.8 Carrier concentration versus Si_2H_6/TMIn molar ratio together with the TOF-SIMS measurement results (samples 1-9)

2.3. Summary

In this chapter, basics of the MOVPE of III-V semiconductors were explained and afterwards the discussion was narrowed down to the growth of Si doped InP. The growth procedure for 11 InP:Si samples was described and the effect of the growth conditions, namely the dopant flux and the V/III precursors ratio, on the free carrier concentration was studied. The resulting free carrier concentration range of the samples was $0.35\text{-}3.87\times10^{19}$ cm^{-3} which shows an almost linear proportionality with the dopant flux up to a threshold above which the morphology of the sample's surface will be deteriorated. It was observed that higher V/III ratio results in a slightly higher free carrier concentration. Si concentration in the samples was measured by TOF-SIMS analysis and compared with the donors' concentration measured by Hall-effect method in order to find the compensation ratio. It was found that in all cases the difference between TOF-SIMS analysis and Hall-effect measurement results is smaller than the measurement error bars which is an indication of negligible self-compensation.

References

1. H. M. Manasevit and W. I. Simpson, "The use of metal-organics in the preparation of semiconductor materials I. Epitaxial gallium-V compounds," J. Elechtrochem. Soc. **116**(12), 1725-1732 (1969).
2. M. J. Ludowise, "Metalorganic chemical vapor deposition of III-V semiconductors," J. Appl. Phys. **58**(8), R31-R55 (1985).
3. W. G. Breiland, M. E. Coltrin, J. R. Creighton, H. Q. Hou, H. K. Moffat, and J. Y. Tsao, "Organometallic vapor phase epitaxy (OMVPE)," Mater. Sci. Eng., R **24**(6), 241-274 (1999).
4. T. F. Kuech, "Metal-organic vapor phase epitaxy of compound semiconductors," Mater. Sci. Rep. **2**(1), 1-49 (1987).
5. K. L. Schulte, J. Simon, N. Jain, D. L. Young, and A. J. Ptak, "A kinetic model for GaAs growth by hydride vapor phase epitaxy," in *Proceedings of the IEEE Photovoltaics Specialists Conference*, (2016), pp. 1930-1933.
6. T. Momose, T. Kamiya, Y. Suzuki, S. Ravasio, C. Cavallotti, M. Sugiyama, and Y. Shimogaki, "Kinetic analysis of GaN-MOVPE via thickness profiles in the gas flow direction with systematically varied growth conditions," ECS J. Solid State Sci. Technol. **5**(3), P164-P171 (2016).
7. S. H. Othman, S. Abdul Rashid, T. I. M. Ghazi, and N. Abdullah, "3D CFD simulations: effect of operation parameters on the deposition of photocatalytic TiO_2 nanoparticles by MOCVD," Chem. Vap. Deposition **21**, 99-110 (2015).
8. P. George, J. Meng, and Y. Jaluria, "Optimization of gallium nitride metalorganic chemical vapor deposition process," J. Heat Transfer **137**(6), 061007 (2015).
9. Y. Xi, T. Gessmann, and E. F. Schubert, "Solubility and dilution of MO sources,".

10. N. Grote, M. Baier, and F. Soares, “Photonic integrated circuits on InP,” Springer Ser. Opt. Sci. **161**, 799-840 (2017).
11. Z. Wang, B. Tian, M. Pantouvaki, W. Guo, P. Absil, J. Van Campenhout, C. Merckling, and D. Van Thourhout, “Room-temperature InP distributed feedback laser array directly grown on silicon,” Nat. Photon. **9**(12), 837-842 (2015).
12. S. Learkthanakhachon, A. Taghizadeh, G. C. Park, K. Yvind, and I.-S. Chung, “Hybrid III-V/SOI resonant cavity enhanced photodetector,” Opt. Express **24**(15), 16512-16519 (2016).
13. A. Taghizadeh, J. Mørk, and I.-S. Chung, “Vertical-cavity in-plane heterostructures: physics and applications,” Appl. Phys. Lett. **107**(18), 181107 (2015).
14. A. Taghizadeh, J. Mørk, and I.-S. Chung, “Numerical investigation of vertical cavity lasers with high-contrast gratings using the Fourier modal method,” J. Lightwave Technol. **34**(18), 4240-4251 (2016).
15. S. Stephan, D. Frederic and A. Markus-Christian, “Novel InP- and GaSb-based light sources for the near to far infrared,” Semicond. Sci. Technol. **31**(11), 113005 (2016).
16. M. B. Bavinck, K. D. Jöns, M. Zieliński, G. Patriarche, J.-C. Harmand, N. Akopian, and V. Zwiller, “Photon cascade from a single crystal phase nanowire quantum dot,” Nano Lett. **16**(2), 1081-1085 (2016).
17. M. E. Aryaee Panah, O. Takayama, S. V. Morozov, K. E. Kudryavtsev, E. S. Semenova, and A. V. Lavrinenko, “Highly doped InP as a low loss plasmonic material for mid-IR region,” Opt. Express **24**(25), 29077-29088 (2016).
18. P. R. Berger, S. N. G. Chu, R. A. Logan, E. Byrne, D. Coblentz, J. Lee III, N. T. Ha, and N. K. Dutta, “Substrate orientation effects on dopant incorporation in InP grown by metalorganic chemical vapor deposition,” J. Appl. Phys. **73** (8), 4095-4097 (1993).
19. C. Blaauw, F. R. Shepherd, C. J. Miner, and A. J. Springthorpe, “Silicon incorporation in InP during LP-MOCVD using disilane,” J. Electron. Mater. **19**(1), 1-6 (1990).
20. A. R. Clawson, T. T. Vu, and D. I. Elder, “A comparison of IV and VI n-dopants for MOVPE-grown InP,” J. Cryst. Growth **83**(2), 211-218 (1987).
21. M. A. Di Forte-Poisson, C. Brylinski, and J. P. Duchemin, “Growth of ultrapure and Si-doped InP by low pressure metalorganic chemical vapor deposition,” Appl. Phys. Lett. **46**(5), 476-478 (1985).
22. Ch. Giesen, X. G. Xu, R. Hovel, M. Heuken, and K. Heime, “Silicon doping of InP grown by MOVPE using tertiarybutylphosphine,” in *Proceedings of the International Conference on Indium Phosphide and Related Materials* (1997), pp. 47–50.
23. S. Leu, H. Protzmann, F. Höhnsdorf, W. Stolz, J. Steinkirchner, and E. Hufgard, “Si-doping of MOVPE grown InP and GaAs by using the liquid Si source ditertiarybutyl silane,” J. Cryst. Growth **195**(1-4), 91-97 (1998).
24. M. Oishi, S. Nojima, and H. Asahi, “Silicon doping in InP grown by metalorganic vapor phase epitaxy using silane,” Jpn. J. Appl. Phys., Part 2 **24**(5), L380-L382 (1985).
25. E. Woelk, and H. Beneking, “Doping of InP and GaInAs during organometallic vaporphase epitaxy using disilane,” J. Appl. Phys. **63**(8), 2874-2876 (1988).
26. A. R. Clawson, C. M. Hanson, “MOCVD grown Si-doped n+ InP layers for the subcollector region in HBTs,” in *proceedings of the sixth international conference on indium phosphide and related materials* (1994), pp. 114-117.

27. D. V. Shenai-Khatkhate, R. L. DiCarlo Jr., R. A. Ware, “Accurate vapor pressure equation for trimethylindium in OMVPE,” J. Cryst. Growth **310**(7-9), 2395-2398 (2008).
28. *PN4300PC Operator's Manual Issue 2* (Accent Semiconductor Technologies (UK) Ltd., 2000).
29. W. Walukiewicz, J. Lagowski, L. Jastrzebski, P. Rava, M. Lichtensteiger, C. H. Gatos, and H. C. Gatos, “Electron mobility and free-carrier absorption in InP; determination of the compensation ratio,” J. Appl. Phys. **51**(5), 2659-2668 (1980).

3. OPTICAL PROPERTIES OF InP:Si

3.1. Introduction to optical properties of InP:Si

Light, as an electromagnetic wave, interacts with matter in different ways that result in different phenomena including reflection, transmission, absorption, scattering and emission. Considering electrons as oscillators and light as the external driving force, their mutual interaction depends on the frequency of light and the resonance frequency of the electrons inside the atom. In metals and doped semiconductors, where there are plenty of free electrons in the conduction band, the free electrons will vibrate with the same frequency as the incoming light but in the opposite phase. In this case no refracted light can propagate inside the material if the density of free electrons is above a certain limit. When the energy of the incoming photons is equal to the energy difference between the valence band and the conduction band of a semiconductor, photons can be absorbed and move the electrons from the valence band to the conduction band. This is called interband transition. In addition, if the frequency of the incoming photons is equal to the resonance frequency of a mechanical vibration mode of the periodic arrangement of atoms, photons can be absorbed and excite a collective mechanical excitation in the crystal, known as phonon. All these phenomena can be summarized in the permittivity of the material which describes its response to an external electromagnetic field. Since each of these phenomena happens in a particular frequency, permittivity will be a function of the frequency and usually defined for a certain frequency range and referred to as the "*dielectric function*". Dielectric function of a material is the key information to understand its optical and in particular plasmonic behavior.

Figures 3.1(a) and (b) show the band structure of InP and the energy gap narrowing versus carrier concentration respectively. The interband transition energies of InP are 1.344 eV (E_0), 1.45 eV ($E_0+\Delta_0$), 3.10 eV (E_1), 3.25 eV ($E_1+\Delta_1$) and 4.7 eV (E_2) [1]. Optical properties of undoped InP near its interband transition energies in

ultra-violet (UV), visible and near-infrared (near-IR) ranges are investigated by different researchers considering its energy band structure [1-6]. Figure 3.2 shows the dielectric function of InP from near-IR to UV.

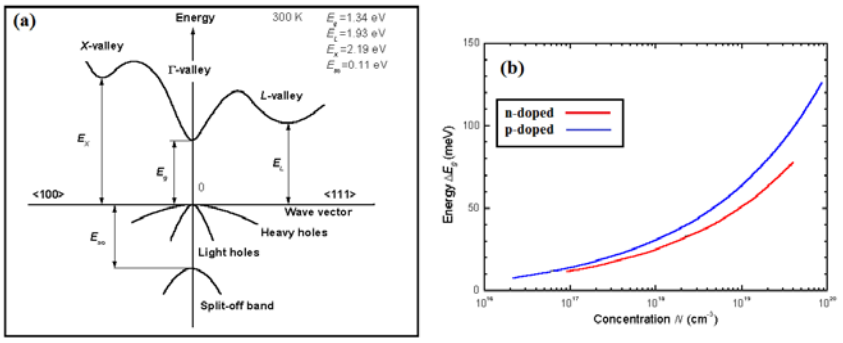

Fig. 3.1 (a) Band structure of InP [7] (b) energy gap narrowing vs carrier concentration for InP [7-9]

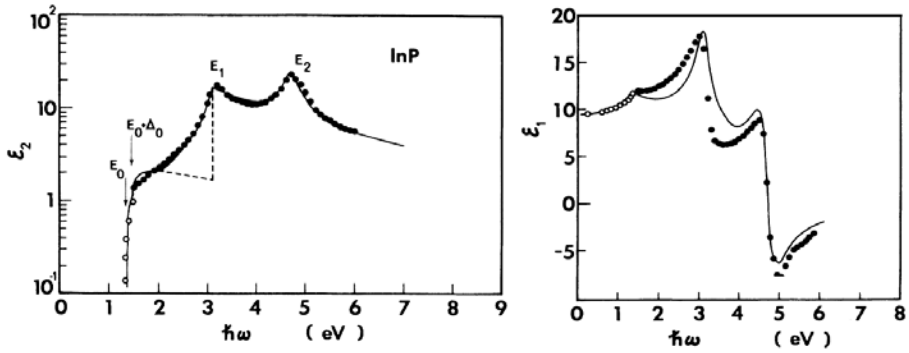

Fig. 3.2 Real and imaginary parts of the permittivity of InP from UV to near-IR [1]

According to Fig. 3.1(b), for an electron concentration of around 4×10^{19} cm^{-3} band gap energy of InP will be around 1.26 eV which corresponds to 984 nm wavelength. Therefore effect of the interband transitions is negligible in the mid-IR range and the free electrons gas oscillations together with the phonon absorptions will be the dominant dispersion phenomena. In this case optical properties of InP can be described by the "*plasma model*" in which the details of the electron-electron interactions and electron-lattice interactions are neglected. The free electrons gas is assumed to oscillate around the fixed positive ions background. The equation of motion for one electron of effective mass m^* under the influence of the external electric field $\mathbf{E}$ is given by [10]:

$$m^*\ddot{\mathbf{X}} + m^*\gamma\dot{\mathbf{X}} = -e\mathbf{E} \tag{3.1}$$

where γ is the free electron's damping and e is the charge of the electron. Assuming a harmonic time dependence for the electric field in form of $\mathbf{E}(t) = \mathbf{E}_0 e^{-i\,\omega t}$, the electron's displacement will also be harmonic, $\mathbf{X}(t) = \mathbf{X}_0 e^{-i\,\omega t}$, which leads to:

$$\mathbf{X}_0 = \frac{e}{m^*(\omega^2 + i\gamma\omega)}\mathbf{E}_0 \,. \tag{3.2}$$

The dielectric displacement field **D**, which accounts for the effect of both free and bound charges inside the material, is related to the external electric field **E,** and the polarization **P** which is the density of electric dipole moments, by

$$\mathbf{D} = \varepsilon_0\mathbf{E} + \mathbf{P} \tag{3.3}$$

in which ε_0 is the electric permittivity of vacuum. For a gas of electrons of density *N*

$$\mathbf{P} = -Ne\mathbf{X} \,. \tag{3.4}$$

Substitution of (3.2) into (3.4) and (3.4) into (3.3) yields

$$\mathbf{D} = \varepsilon_0\left(1 - \frac{\omega_p^2}{\omega^2 + i\gamma\omega}\right)\mathbf{E} \tag{3.5}$$

where ω_p is the "*plasma frequency*", defined as

$$\omega_p = \sqrt{\frac{Ne^2}{\varepsilon_0 m^*}} \,. \tag{3.6}$$

On the other hand **P** and **D** can be related to each other, via electric susceptibility χ, by

$$\mathbf{P} = \varepsilon_0\chi\mathbf{E} \,. \tag{3.7}$$

Using (3.7) in (3.3) and defining the relative permittivity as $\varepsilon = 1 + \chi$, one will get to the constitutive relation

$$\mathbf{D} = \varepsilon_0\varepsilon\mathbf{E} \,. \tag{3.8}$$

Comparison with Eq. (3.5) will give the dielectric function of the free electron gas in form of the "*Drude model*" [10]

$$\varepsilon(\omega) = 1 - \frac{\omega_p^2}{\omega^2 + i\gamma\omega} \,. \tag{3.9}$$

In the free electron model $\varepsilon(\omega) \to 1$ for $\omega \gg \omega_p$. This is not true for real metals and doped semiconductors in which the positive background of the ions affects the polarization. This effect is taken into account by introducing a high frequency permittivity ε_∞ in the Drude model

$$\varepsilon(\omega) = \varepsilon_\infty\left(1 - \frac{\omega_p^2}{\omega^2 + i\gamma\omega}\right) \tag{3.10}$$

and adjusting the plasma frequency accordingly:

$$\omega_p = \sqrt{\frac{Ne^2}{\varepsilon_\infty\varepsilon_0 m^*}} \,. \tag{3.11}$$

In order to account for the contribution of the phonons to the optical dispersion of the material, Drude model is extended to the "*Drude-Lorentz*" model:

$$\varepsilon(\omega) = \varepsilon_\infty \left(1 - \frac{\omega_p^2}{\omega^2 + i\,\omega\gamma}\right) + \sum_j \frac{S_j \omega_{f,j}^2}{\omega_{f,j}^2 - \omega^2 - i\,\omega\Gamma_j}. \quad (3.12)$$

Here S_j, $\omega_{f,j}$ and Γ_j are the strength, resonance frequency and damping for the jth Lorentzian oscillator respectively, describing a phonon absorption at frequency $\omega_{f,j}$.

Optical properties of doped InP in the IR range have been investigated by different research groups. Jayasinghe *et al.* studied dielectric function and plasma frequency of p-doped InP in the IR range. The maximum carrier concentration considered was 2.4×10^{19} cm^{-3} pertaining to a plasma wavelength equal to 15.4 μm [11]. The large plasma wavelength in this case is due to the high effective mass of holes. Zheng *et al.* were able to achieve free electron concentrations as high as 1.1×10^{20} cm^{-3} in InP, using molecular beam epitaxy (MBE) and Si as the dopant. They discussed photoluminescence measurement data for samples with different carrier concentrations [12]. El-Nahass *et al.* measured transmittance and reflectance of sulfur doped InP with a carrier concentration of 3×10^{18} cm^{-3} in the wavelength range of 200-2500 nm in order to derive the absorption coefficient and refractive index [13]. Hua *et al.* measured the IR reflectance of bulk sulfur and tin doped InP samples with a maximum carrier concentration of 1.2×10^{19} cm^{-3}, and studied the position of the reflectance minima for different carrier concentrations [14]. Very recently, Cada *et al.* have used Fourier transform infrared (FTIR) spectroscopy together with Raman scattering measurements to determine the plasma frequency of heavily doped InP [15].

In this chapter reflectance from the samples with an n-doped InP epilayer will be calculated and fitted to the experimentally determined reflectance spectra, in order to restore the dielectric function of n-doped InP for different carrier concentrations. Using the restored dielectric function, plasmonic properties of n-doped InP in the mid-IR range will be compared to other semiconductors.

3.2. Reflectance calculation

3.2.1. Normal incidence

In this section the reflectance spectra from the samples with an InP:Si epilayer on top of a semi-insulating (SI) InP:Fe or InP:S substrate will be calculated.

Consider an electric field linearly polarized in the *x* direction and propagating in an isotropic medium along the *z* direction, defined as $\mathbf{E}(z) = \hat{\mathbf{x}}E_x(z) = \hat{\mathbf{x}}E(z)$, together

with the pertaining magnetic field defined as $\mathbf{H}(z) = \hat{\mathbf{y}}H_y(z) = \hat{\mathbf{y}}H(z)$. The total electric and magnetic fields will be [16]

$$\begin{aligned} E(z) &= E_{0+}e^{ikz} + E_{0-}e^{-ikz} = E_+(z) + E_-(z) \\ H(z) &= \frac{1}{\eta}\left[E_{0+}e^{ikz} - E_{0-}e^{-ikz}\right] = \frac{1}{\eta}\left[E_+(z) - E_-(z)\right] \end{aligned} \tag{3.13}$$

in which the subscripts + and – denote the forward and backward travelling waves respectively, *k* is the wavevector and $\eta = \sqrt{\frac{\mu}{\varepsilon}}$ is the impedance of the medium, where μ denotes the relative permeability of the medium.

The reflection coefficient at position *z* is defined as:

$$\Gamma(z) = \frac{E_-(z)}{E_+(z)} = \frac{E_{0-}e^{-ikz}}{E_{0+}e^{ikz}}. \tag{3.14}$$

Figure 3.3 shows the electric and magnetic fields at positions z_1 and z_2, which can be defined, using Eq. (3.13), as

$$\begin{aligned} E_{2+} &= E_{0+}e^{ikz_2} \\ E_{1+} &= E_{0+}e^{ikz_1} = E_{0+}e^{ik(z_2-l)} = e^{-ikl}E_{2+}. \end{aligned} \tag{3.15}$$

Similarly $E_{1-} = e^{ikl}E_{2-}$. Therefore in matrix form

$$\begin{bmatrix} E_{1+} \\ E_{1-} \end{bmatrix} = \begin{bmatrix} e^{-ikl} & 0 \\ 0 & e^{ikl} \end{bmatrix} \begin{bmatrix} E_{2+} \\ E_{2-} \end{bmatrix}. \tag{3.16}$$

The two by two matrix in Eq. (3.16) is referred to as the propagation matrix, which describes the relation between the electric fields on the left and right sides of the space between z_1 and z_2.

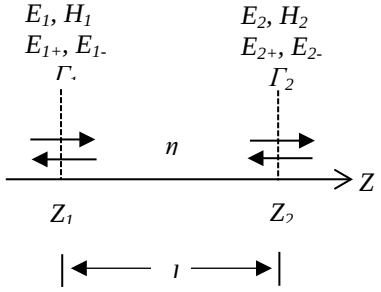

Fig. 3.3 Electric and magnetic fields propagated between points z_1 and z_2 [16]

Consider a planar interface in the *xy* plane at position *z* between two different media with impedances η and η' (Fig. 3.4).

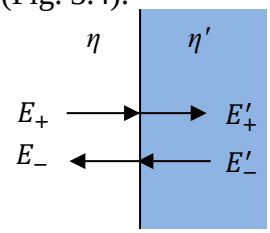

Fig. 3.4 Electric fields across an interface

In case of normal incidence, electric and magnetic fields are tangential to the interface, therefore the boundary conditions require that the total fields be continuous across the interface, which means:

$$\begin{aligned} E &= E' \\ H &= H'. \end{aligned} \tag{3.17}$$

According to (3.13)

$$\begin{aligned} E_+ + E_- &= E'_+ + E'_- \\ \frac{1}{\eta}(E_+ - E_-) &= \frac{1}{\eta'}(E'_+ - E'_-)\,. \end{aligned} \tag{3.18}$$

Equation (3.18) can be rewritten in matrix form:

$$\begin{aligned} \begin{bmatrix} E_+ \\ E_- \end{bmatrix} &= \frac{1}{\tau}\begin{bmatrix} 1 & \rho \\ \rho & 1 \end{bmatrix}\begin{bmatrix} E'_+ \\ E'_- \end{bmatrix} \\ \begin{bmatrix} E'_+ \\ E'_- \end{bmatrix} &= \frac{1}{\tau'}\begin{bmatrix} 1 & \rho' \\ \rho' & 1 \end{bmatrix}\begin{bmatrix} E_+ \\ E_- \end{bmatrix} \end{aligned} \tag{3.19}$$

where τ and ρ are transmission and reflection coefficients from the left side and τ' and ρ' are transmission and reflection coefficients from the right side defined as

$$\begin{aligned} \rho &= \frac{\eta' - \eta}{\eta' + \eta}\,, \quad \tau = \frac{2\eta'}{\eta' + \eta} \\ \rho' &= \frac{\eta - \eta'}{\eta' + \eta}\,, \quad \tau' = \frac{2\eta}{\eta' + \eta}\,. \end{aligned} \tag{3.20}$$

The two by two matrices in Eq. (3.19) are referred to as the matching matrices, which describe the relation between the electric fields on the left and right sides of the interface between the two media.

Regarding that $\eta = \eta_0/n$ and $\eta' = \eta_0/n'$, with n and n' being the refractive indices of the left and right media respectively, Eqs. (3.20) can be rewritten in terms of the refractive indices:

$$\begin{aligned} \rho &= \frac{n - n'}{n + n'}\,, \quad \tau = \frac{2n}{n + n'} \\ \rho' &= \frac{n' - n}{n' + n}\,, \quad \tau' = \frac{2n'}{n' + n}\,. \end{aligned} \tag{3.21}$$

The relation between the electric fields on the left (A_1 and B_1) and right sides (A_2 and B_2) of a slab (Fig. 3.5) is given by the combination of the matching matrix for the left interface, propagation matrix, and the matching matrix for the right interface of the slab as

$$\begin{bmatrix} A_1 \\ B_1 \end{bmatrix} = \frac{1}{\tau_1}\begin{bmatrix} 1 & \rho_1 \\ \rho_1 & 1 \end{bmatrix}\begin{bmatrix} e^{-ikl} & 0 \\ 0 & e^{ikl} \end{bmatrix}\frac{1}{\tau_2}\begin{bmatrix} 1 & \rho_2 \\ \rho_2 & 1 \end{bmatrix}\begin{bmatrix} A_2 \\ B_2 \end{bmatrix} = \mathbf{T}\begin{bmatrix} A_2 \\ B_2 \end{bmatrix} \tag{3.22}$$

in which k is the wavevector inside the slab defined as $k = nk_0$, where n is the refractive index of the material inside the slab and k_0 is the wavevector of the light in

vacuum. **T** is known as the "*transfer matrix*" of the slab. Same procedure can be applied in order to find the transfer matrix for a cascade of optical elements.

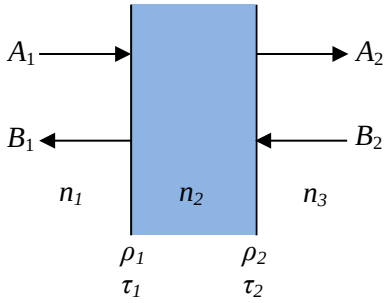

Fig. 3.5 Electric fields across a slab

Using transfer matrix approach, transmission T defined as the ratio of the transmitted optical power to the incident optical power, and reflection R defined as the ratio between the reflected optical power and the incident optical power are given by [17]

$$R = \left|\frac{\boldsymbol{T}_{21}}{\boldsymbol{T}_{11}}\right|^2$$
$$T = \left|\frac{1}{\boldsymbol{T}_{11}}\right|^2 \qquad (3.23)$$

For a lossless medium where there is no absorption $R + T = 1$.

Using the transfer matrix method and the Drude-Lorentz dielectric function with its parameters listed in Table 3.1 and 3.2, reflectance spectrum of a 350 μm thick SI InP:Fe wafer is calculated. Figure 3.6 shows the calculated reflectance spectrum together with the reflectance spectrum measured by FTIR. The details of FTIR measurements will be given in section 3.4.

Table 3.1 Parameters of the Lorentzian terms for the dielectric function of SI InP:Fe

j	1	2	3	4	5	6
S_j	1.7×10^{-4}	1.19×10^{-4}	6.13×10^{-5}	1.78×10^{-3}	1.56	2.85
Γ_j[THz]	0.51	0.4	0.28	1.33	1282.89	4.63×10^{-3}
$\omega_{f,j}$[THz]	18.73	19.76	20.49	14.74	14.82	9.08

Table 3.2 Parameters of the Drude term for the dielectric function of SI InP:Fe

ω_p[THz]	γ[THz]	ε_∞
3.77×10^{-5}	3	9.55

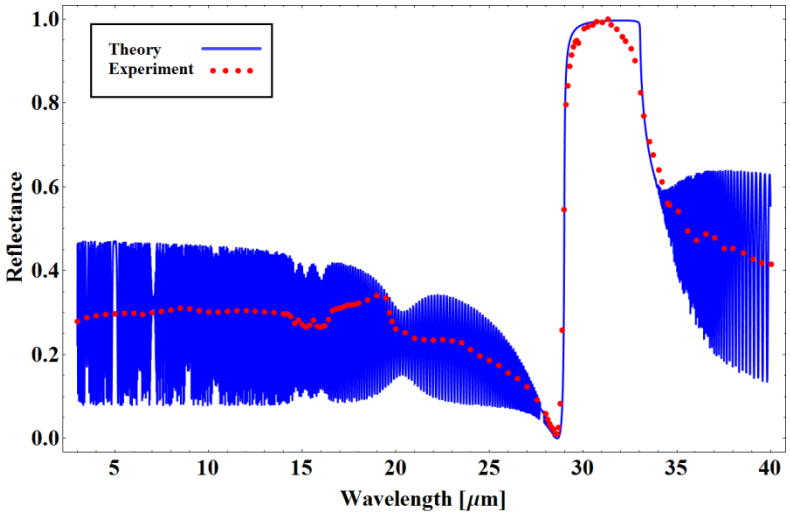

Fig. 3.6 Reflectance spectrum of a 350 μm thick InP:Fe slab, measured using FTIR and calculated using the transfer matrix method

As it can be seen in Fig. 3.6, there are oscillations in the calculated reflectance spectrum which originate from constructive and destructive interferences in the InP:Fe slab. These oscillations which are known as Fabry-Perot fringes, are not observed in the measured reflectance spectrum due to the deviations from the ideal conditions. These deviations can be attributed to the light source, method of observation or small misalignments between the interfaces [18,19]. Fabry-Perot fringes will be suppressed more in case of thicker layers, therefore in order to calculate the reflectance spectra of our samples comprising a thin epilayer on top of a thick substrate, an alternative method called "*intensity transfer matrix*" is used which eliminates the Fabry-Perot fringes from the thick substrate but retains the fringes from the thin epilayers [18]. Figure 3.7 depicts a schematic of a thin film on top of a thick substrate together with light beams reflected from and transmitted through different interfaces. R_a and T_a are the reflectance and transmittance of the light coming from the left side, considering an infinitely thick substrate. R'_a and T'_a are the reflectance and transmittance of the light coming from the right side, considering an infinitely thick substrate. R_b and T_b are the reflectance and transmittance of the light from the interface at the right side of the substrate. The total reflectance of the epilayer/substrate system will be obtained by adding the intensity of light travelling in different paths [18]:

$$\mathcal{R} = R_a + T_a T'_a R_b e^{-2\alpha d} + T_a T'_a R'_a R_b^2 e^{-4\alpha d} + \cdots = R_a + \frac{T_a T'_a R_b e^{-2\alpha d}}{1 - R'_a R_b e^{-2\alpha d}} \qquad (3.24)$$

where d is the thickness of the substrate and $\alpha = 4\pi \frac{\omega}{c} \mathrm{Im}\left[\sqrt{\varepsilon_s}\right]$, in which c is the speed of light and ε_s is the permittivity of the substrate.

Transmittance through the epilayer/substrate system can also be calculated in a similar way:

$$\mathcal{T} = \frac{T_a T_b e^{-\alpha d}}{1 - R'_a R_b e^{-2\alpha d}} \tag{3.25}$$

More detailed derivation of transmittance and reflectance is given in [18].

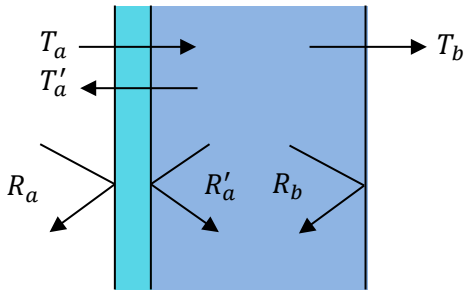

Fig. 3.7 Schematic of the reflectance and transmittance from different interfaces, used in the intensity transfer matrix method

Figure 3.8 shows the reflectance spectrum calculated for the InP:Fe slab using the intensity transfer matrix method, which shows a good agreement with the experimentally determined reflectance.

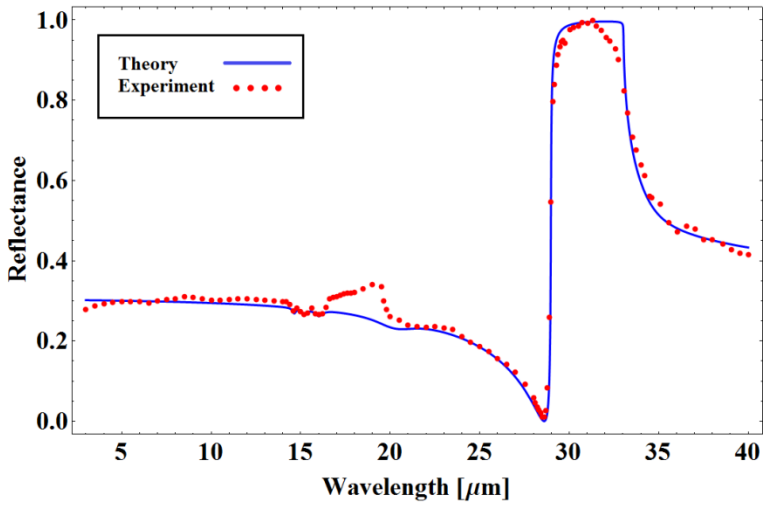

Fig. 3.8 Reflectance spectrum of a 350 μm thick InP:Fe slab, measured using FTIR and calculated using intensity transfer matrix method

The computer program developed for calculation of the reflectance spectra of a multilayer structure, using the intensity transfer matrix method, is presented in Appendix A.

3.2.2. Oblique incidence

Polarization of the incoming light becomes important in the case of oblique incidence, and waves with different polarizations will have different reflection and transmission coefficients. Figure 3.9 shows a schematic of the transverse electric (TE) and transverse magnetic (TM) polarized light obliquely incident on the interface between two materials. In TM polarization, the magnetic field is perpendicular and the electric field is parallel to the plane of incidence. In TE polarization, the electric field is perpendicular and the magnetic field is parallel to the plane of incidence.

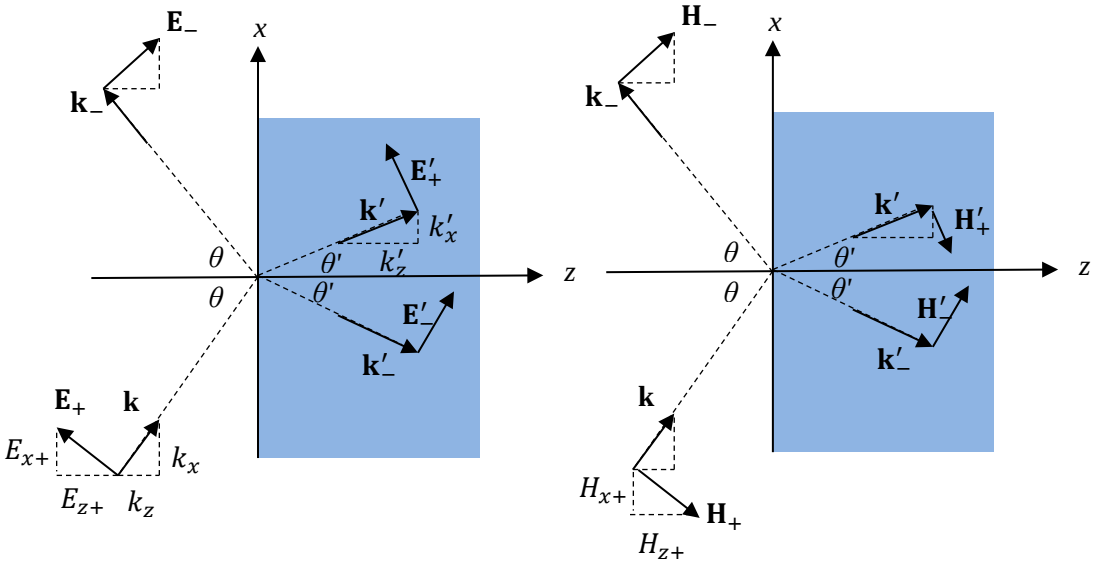

Fig. 3.9 TM (left) and TE (right) polarized waves in oblique incidence [16]

The electric and magnetic fields can be separated into transverse and longitudinal components with respect to the direction that the layers are stacked i.e. z direction. The transfer matrix relations for normal incidence, that were explained in section 3.2.1, also apply for the transverse component provided that proper reflection and transmission coefficients are used.

The incident and reflected electric fields at the two sides will have the form [16]

$$\mathbf{E}_+ e^{i\mathbf{k}_+.\mathbf{r}}\,,\mathbf{E}_- e^{i\mathbf{k}_-.\mathbf{r}}\,,\mathbf{E}'_+ e^{i\mathbf{k}'_+.\mathbf{r}}\,,\mathbf{E}'_- e^{i\mathbf{k}'_-.\mathbf{r}} \tag{3.26}$$

where the wavevector is

$$\mathbf{k}_\pm = \hat{\mathbf{x}}k_{x\pm} + \hat{\mathbf{y}}k_{y\pm} + \hat{\mathbf{z}}k_{x\pm}\,. \tag{3.27}$$

$\mathbf{k}'_\pm$ is also defined in a similar way.

According to the boundary condition, the net transverse component of the electric field must be continuous across the interface:

$$\mathbf{E}_{T+} e^{i\mathbf{k}_+.\mathbf{r}} + \mathbf{E}_{T-} e^{i\mathbf{k}_-.\mathbf{r}} = \mathbf{E}'_{T+} e^{i\mathbf{k}'_+.\mathbf{r}} + \mathbf{E}'_{T-} e^{i\mathbf{k}'_-.\mathbf{r}} \quad \text{at } z=0 \tag{3.28}$$

where the subscript T denotes the transverse part of a vector with respect to z direction. Setting $z = 0$, Eq. (3.28) yields

$$\begin{aligned} &\mathbf{E}_{T+}e^{i(k_{x+}x+k_{y+}y)} + \mathbf{E}_{T-}e^{i(k_{x-}x+k_{y-}y)} \\ &= \mathbf{E}'_{T+}e^{i(k'_{x+}x+k'_{y+}y)} + \mathbf{E}'_{T-}e^{i(k'_{x-}x+k'_{y-}y)}. \end{aligned} \tag{3.29}$$

For the two sides of Eq. (3.29) to match at all points on the interface, the exponential phase factors in this equation must be equal for all x and y. Therefore

$$\begin{aligned} k_{x+} = k_{x-} = k'_{x+} = k'_{x-} \\ k_{y+} = k_{y-} = k'_{y+} = k'_{y-}\,. \end{aligned} \tag{3.30}$$

If the plane of incidence lies in the xz plane, then all of the wavevector components in the y direction will be zero. Equation (3.30) for the x components gives

$$k\sin\theta_+ = k\sin\theta_- = k'\sin\theta'_+ = k'\sin\theta'_-\ , \tag{3.31}$$

which implies the *Snel's law of reflection*:

$$\begin{aligned} \theta_+ = \theta_- = \theta \\ \theta'_+ = \theta'_- = \theta'\,, \end{aligned} \tag{3.32}$$

and the *Snel's law of refraction*, regarding that $k = nk_0$ and $k' = n'k_0$:

$$\frac{\sin\theta}{\sin\theta'} = \frac{n'}{n}\,. \tag{3.33}$$

If A_+ and B_+represent the TM and TE components of the electromagnetic field respectively, the total electric and magnetic fields incident from the left side will be

$$\begin{aligned} \mathbf{E}_+(\mathbf{r}) &= [(\hat{\mathbf{x}}\cos\theta - \hat{\mathbf{z}}\sin\theta)A_+ + \hat{\mathbf{y}}B_+]e^{i\mathbf{k}_+\cdot\mathbf{r}} \\ \mathbf{H}_+(\mathbf{r}) &= \frac{1}{\eta}[\hat{\mathbf{y}}A_+ - (\hat{\mathbf{x}}\cos\theta - \hat{\mathbf{z}}\sin\theta)B_+]e^{i\mathbf{k}_+\cdot\mathbf{r}}\,. \end{aligned} \tag{3.34}$$

The total reflected electric and magnetic fields will be

$$\begin{aligned} \mathbf{E}_-(\mathbf{r}) &= [(\hat{\mathbf{x}}\cos\theta + \hat{\mathbf{z}}\sin\theta)A_- + \hat{\mathbf{y}}B_-]e^{i\mathbf{k}_-\cdot\mathbf{r}} \\ \mathbf{H}_-(\mathbf{r}) &= \frac{1}{\eta}[-\hat{\mathbf{y}}A_- + (\hat{\mathbf{x}}\cos\theta + \hat{\mathbf{z}}\sin\theta)B_-]e^{i\mathbf{k}_-\cdot\mathbf{r}}\,. \end{aligned} \tag{3.35}$$

The transverse amplitudes and the transverse impedances are defined as

$$\begin{aligned} A_{T\pm} = A_\pm\cos\theta\ , B_{T\pm} = B_\pm \\ \eta_{TM} = \eta\cos\theta\ , \eta_{TE} = \frac{\eta}{\cos\theta} \end{aligned} \tag{3.36}$$

Using (3.36), the transverse components of the electric and magnetic fields are given by

$$\begin{aligned} \mathbf{E}_{T+}(x,z) &= [\hat{\mathbf{x}}A_{T+} + \hat{\mathbf{y}}B_{T+}]e^{i(k_x x+k_z z)} \\ \mathbf{H}_{T+}(x,z) &= \left[\hat{\mathbf{y}}\frac{A_{T+}}{\eta_{TM}} - \hat{\mathbf{x}}\frac{B_{T+}}{\eta_{TE}}\right]e^{i(k_x x+k_z z)} \\ \mathbf{E}_{T-}(x,z) &= [\hat{\mathbf{x}}A_{T-} + \hat{\mathbf{y}}B_{T-}]e^{i(k_x x-k_z z)} \\ \mathbf{H}_{T-}(x,z) &= \left[-\hat{\mathbf{y}}\frac{A_{T-}}{\eta_{TM}} + \hat{\mathbf{x}}\frac{B_{T-}}{\eta_{TE}}\right]e^{i(k_x x-k_z z)}\,. \end{aligned} \tag{3.37}$$

Adding the relations for the incident and reflected waves and ignoring the factor $e^{ik_x x}$ which is equal on both sides of the interface we will get

$$\begin{aligned}\mathbf{E}_T(z) &= \hat{\mathbf{x}}E_{TM}(z) + \hat{\mathbf{y}}E_{TE}(z)\\ \mathbf{H}_T(z) &= \hat{\mathbf{y}}H_{TM}(z) - \hat{\mathbf{x}}H_{TE}(z)\,.\end{aligned} \tag{3.38}$$

Using the transverse impedance:

$$\begin{aligned}E_{TM}(z) &= A_{T+}e^{ik_z z} + A_{T-}e^{-ik_z z}\\ H_{TM}(z) &= \frac{1}{\eta_{TM}}\left[A_{T+}e^{ik_z z} - A_{T-}e^{-ik_z z}\right]\\ E_{TE}(z) &= B_{T+}e^{ik_z z} + B_{T-}e^{-ik_z z}\\ H_{TE}(z) &= \frac{1}{\eta_{TE}}\left[B_{T+}e^{ik_z z} - B_{T-}e^{-ik_z z}\right].\end{aligned} \tag{3.39}$$

The above equations can be written in compact form:

$$\begin{aligned}E_T(z) &= E_{T+}e^{ik_z z} + E_{T-}e^{-ik_z z}\\ H_T(z) &= \frac{1}{\eta_T}\left[E_{T+}e^{ik_z z} - E_{T-}e^{-ik_z z}\right]\end{aligned} \tag{3.40}$$

where E_T stands for both E_{TM} or E_{TE}.

Equation (3.40) will be similar to Eq. (3.13) if we substitute

$$\eta \to \eta_T\,, e^{\pm ikz} \to e^{\pm ik_z z} = e^{\pm ikz\cos\theta}\,. \tag{3.41}$$

The transverse reflection coefficient reads

$$\Gamma_T(z) = \frac{E_{T-}(z)}{E_{T+}(z)} = \frac{E_{T-}e^{-ik_z z}}{E_{T+}e^{ik_z z}} = \Gamma_T(0)e^{-2ik_z z}\,. \tag{3.42}$$

Hence, the propagation matrix will be

$$\begin{bmatrix}E_{T1+}\\ E_{T1-}\end{bmatrix} = \begin{bmatrix}e^{-ik_z l} & 0\\ 0 & e^{ik_z l}\end{bmatrix}\begin{bmatrix}E_{T2+}\\ E_{T2-}\end{bmatrix} \tag{3.43}$$

where $k_z = k\cos\theta$ and $l = z_2 - z_1$ (Fig. 3.3).

The matching matrix will be

$$\begin{bmatrix}E_{T+}\\ E_{T-}\end{bmatrix} = \frac{1}{\tau_T}\begin{bmatrix}1 & \rho_T\\ \rho_T & 1\end{bmatrix}\begin{bmatrix}E'_{T+}\\ E'_{T-}\end{bmatrix}. \tag{3.44}$$

Using the Snel's law together with the second equation of (3.36), the reflection coefficients for TM and TE polarizations are found to be [16]

$$\rho_{TM} = \frac{\sqrt{\left(\frac{n'}{n}\right)^2 - \sin^2\theta} - \left(\frac{n'}{n}\right)^2 \cos\theta}{\sqrt{\left(\frac{n'}{n}\right)^2 - \sin^2\theta} + \left(\frac{n'}{n}\right)^2 \cos\theta}$$
$$\rho_{TE} = \frac{\cos\theta - \sqrt{\left(\frac{n'}{n}\right)^2 - \sin^2\theta}}{\cos\theta + \sqrt{\left(\frac{n'}{n}\right)^2 - \sin^2\theta}}. \quad (3.45)$$

The transmission coefficients can be found from (3.45), using the relation $\tau = \sqrt{1-\rho^2}$.

For a multilayer structure under oblique incidence, first the angle of incidence for each layer should be calculated using Snel's law. The calculated angle of incidence should then be used in Eqs. (3.43), (3.44) and (3.45) to find the transfer matrix. Finally, the reflectance for both polarizations should be added in order to find the total reflectance. In case of multilayers on top of a thick substrate, in order to eliminate Fabry-Perot fringes originating from the substrate, the transfer matrix should be used in conjunction with the Eq. (3.24).

The computer program developed for calculation of the oblique reflectance spectra of a multilayer structure, using the intensity transfer matrix method, is presented in Appendix B.

3.3. Levenberg-Marquardt method

In order to find the dielectric function of InP:Si with different carrier concentrations, reflectance spectra of the epilayer/substrate system are calculated using the intensity transfer matrix method and the Drude-Lorentz dielectric function for InP. The calculated reflectance spectra are then fitted to the experimentally determined one to find the parameters of the Drude-Lorentz function for InP with different carrier concentrations. In this section, details of the used nonlinear curve fitting algorithm, known as the Levenberg-Marquardt method, will be explained.

Consider a nonlinear function of x which depends on the set of unknown parameters $a_k, k = 1, 2, \dots, M$:

$$y = y(x; \mathbf{a}) \quad (3.46)$$

in which **a** is the set of a_k in vector form. The goal is to fit y to a set of experimental points $y_i, i = 1, 2, \dots, N$, and minimize an error function χ^2, defined as

$$\chi^2(\mathbf{a}) = \sum_{i=1}^{N} \left[\frac{y_i - y(x_i; \mathbf{a})}{\sigma_i} \right]^2 \tag{3.47}$$

where σ_i is the standard deviation corresponding to a number of measurements at x_i.

Taylor expansion of the function $\chi^2(\mathbf{a})$ at $\mathbf{a} = \mathbf{a}_0$ gives

$$\begin{aligned} \chi^2(\mathbf{a}) &= \chi^2(\mathbf{a}_0) + \sum_i \frac{\partial \chi^2}{\partial a_i} a_i + \frac{1}{2} \sum_{i,j} \frac{\partial^2 \chi^2}{\partial a_i \partial a_j} a_i a_j + \cdots \\ &\cong \chi^2(\mathbf{a}_0) - \mathbf{d}.\mathbf{a} + \frac{1}{2} \mathbf{a}.\mathbf{D}.\mathbf{a} \end{aligned} \tag{3.48}$$

in which $\mathbf{d}$ and $\mathbf{D}$ are the M-vector gradient and $M \times M$ Hessian matrix of χ^2 at $\mathbf{a}_0$ respectively**,** defined as

$$\begin{aligned} \mathbf{d} &= -\nabla \chi^2 |_{\mathbf{a}_0} \\ \mathbf{D} &= \left. \frac{\partial^2 \chi^2}{\partial a_i \partial a_j} \right|_{\mathbf{a}_0} . \end{aligned} \tag{3.49}$$

Using (3.48), gradient of χ^2 is found to be

$$\nabla \chi^2 = \mathbf{D}.\mathbf{a} - \mathbf{d} . \tag{3.50}$$

If $\mathbf{a}_{min}$ corresponds to a minimizing set of parameters for χ^2

$$\mathbf{D}.\mathbf{a}_{min} = \mathbf{d} . \tag{3.51}$$

On the other hand, at the current trial set of parameters $\mathbf{a}_{cur}$

$$\mathbf{D}.\mathbf{a}_{cur} = \nabla \chi^2 + \mathbf{d} . \tag{3.52}$$

If the approximation (3.48) is good enough, subtracting (3.52) from (3.51) gives us the step that we need to take in order to jump from $\mathbf{a}_{cur}$ to $\mathbf{a}_{min}$**,** namely

$$\mathbf{a}_{min} - \mathbf{a}_{cur} = \mathbf{D}^{-1}.[-\nabla \chi^2(\mathbf{a}_{cur})] . \tag{3.53}$$

Otherwise, if we are far from the minimum of χ^2 and (3.48) is not a good approximation, we should take a step down the gradient according to the steepest descent method [20]. In other words

$$\mathbf{a}_{next} = \mathbf{a}_{cur} - \text{constant} \times \nabla \chi^2(\mathbf{a}_{cur}) \tag{3.54}$$

where the constant should be small enough not to spoil the downhill direction.

The gradient of χ^2 with respect to $\mathbf{a}$ is

$$\frac{\partial \chi^2}{\partial a_k} = -2 \sum_{i=1}^{N} \frac{y_i - y(x_i; \mathbf{a})}{\sigma_i^2} \frac{\partial y(x_i; \mathbf{a})}{\partial a_k} \quad , \qquad k = 1, 2, \ldots, M \tag{3.55}$$

The Hessian matrix of χ^2 with respect to $\mathbf{a}$ is

$$[\mathbf{D}]_{kl} = \frac{\partial^2 \chi^2}{\partial a_k \partial a_l} = 2\sum_{i=1}^{N} \frac{1}{\sigma_i^2}\left[\frac{\partial y(x_i;\mathbf{a})}{\partial a_k}\frac{\partial y(x_i;\mathbf{a})}{\partial a_l} - [y_i - y(x_i;\mathbf{a})]\frac{\partial^2 y(x_i;\mathbf{a})}{\partial a_l \partial a_k}\right]. \quad (3.56)$$

Defining

$$\begin{aligned} \beta_k &= -\frac{1}{2}\frac{\partial \chi^2}{\partial a_k} \\ \alpha_{kl} &= \frac{1}{2}\frac{\partial^2 \chi^2}{\partial a_k \partial a_l} \\ \delta a_l &= \mathbf{a}_{min} - \mathbf{a}_{cur} \ , \end{aligned} \quad (3.57)$$

one can rewrite (3.53) as a set of linear equations

$$\sum_{l=1}^{M} \alpha_{kl}\delta a_l = \beta_k \ . \quad (3.58)$$

Solving the set of equations for δa_l in (3.58), we will find the value that added to the current approximation, gives the next approximation.

Equation (3.54) can be written as

$$\delta a_l = \text{constant} \times \beta_l \ . \quad (3.59)$$

The second order derivatives in Eq. (3.56) can be neglected if they are very small in comparison to the term involving the first derivative. In fact, inclusion of the second derivative terms may destabilize the iterative fitting process [20]. Therefore, the second equation in (3.57) can be written as

$$\alpha_{kl} = \sum_{i=1}^{N} \frac{1}{\sigma_i^2}\left[\frac{\partial y(x_i;\mathbf{a})}{\partial a_k}\frac{\partial y(x_i;\mathbf{a})}{\partial a_l}\right]. \quad (3.60)$$

In order for the iterative fitting process to proceed, one needs to know the "constant" value in Eq. (3.59). χ^2 is nondimensional and β_l has the dimension $\frac{1}{a_k}$. Hence, the "constant" in (3.59) should have the dimension a_k^2. The reciprocal of the diagonal elements of $[\alpha]_{kl}$ also have the dimension a_k^2. This information helps to define the "constant" value in (3.59), using a nondimensional fudge factor λ which can adjust the iteration step. Equation (3.59) now reads [20]

$$\delta a_l = \frac{1}{\lambda \alpha_{ll}}\beta_l \ . \quad (3.61)$$

Equations (3.58) and (3.61) can be combined as

$$\sum_{l=1}^{M} \alpha'_{kl}\delta a_l = \beta_k \quad (3.62)$$

in which the new matrix α' is defined by

$$\alpha'_{jj} = \alpha_{jj}(1 + \lambda)$$
$$\alpha'_{jk} = \alpha_{jk} \quad (j \neq k) \tag{3.63}$$

When the fudge factor λ is very large, α becomes diagonally dominant and the Eq. (3.62) will become almost identical to the Eq. (3.61). When λ approaches zero, Eq. (3.62) will become almost identical to the Eq. (3.58). Therefore, the equation which determines the next iterative step will be smoothly varying between (3.58) and (3.62), depending on how close we are to the minimum value of χ^2. The iteration continues until the error function becomes smaller than a minimum value χ_{min} in the last few iterations. χ_{min} can be chosen differently for different problems, depending on the order of the standard deviation of the experimental data σ_i. Figure 3.10 shows the flowchart for the Levenberg-Marquardt method [20].

The computer program developed for fitting the reflectance spectra of the epilayer/substrate system, based on the Levenberg-Marquardt method, is presented in Appendix C.

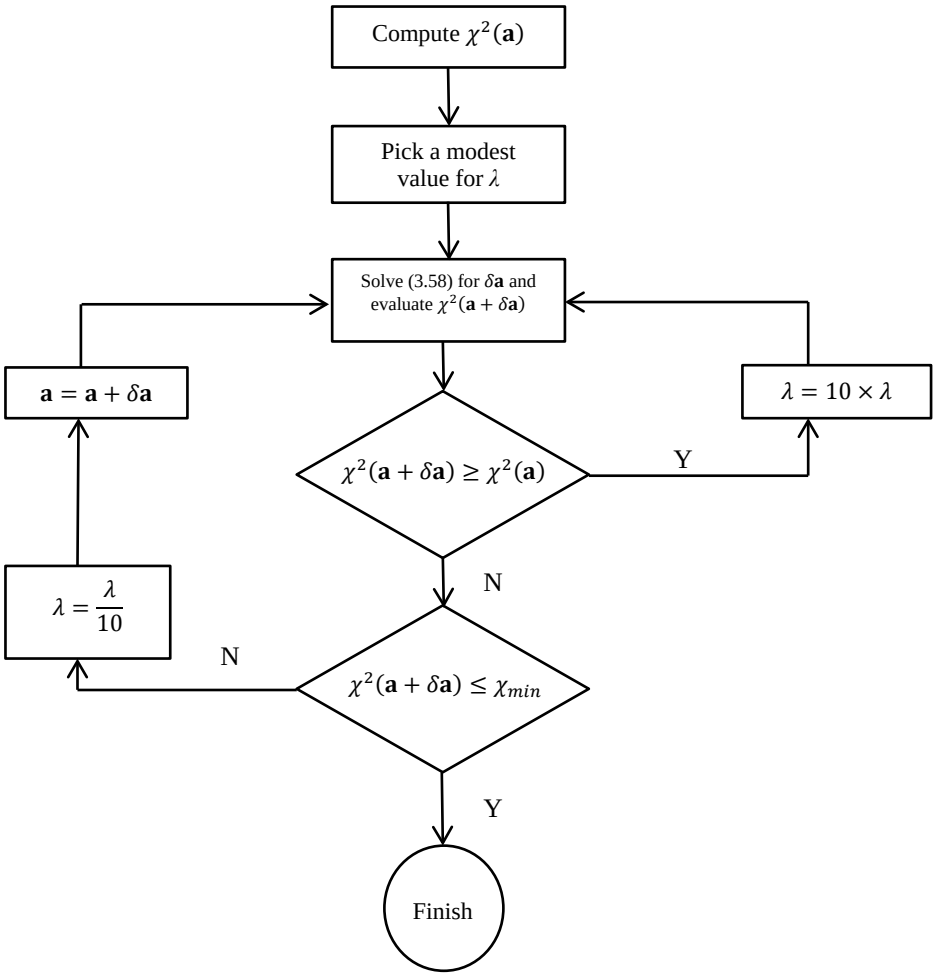

Fig. 3.10 Flowchart of the Levenberg-Marquardt algorithm for nonlinear curve fitting

3.4. Dielectric function of InP:Si in the mid-infrared range

In this section, details of the FTIR reflectance measurements will be explained. The measured reflectance spectra will be used to restore the dielectric function of InP:Si for samples with different free carrier concentrations.

Reflectance spectra of the grown InP:Si samples and their substrates are measured in the wavelength range of 3-40 μm, using a VERTEX 70 FTIR spectrometer from Bruker. Figure 3.11 shows the top view of the beam path inside the spectrometer. A reflection measurement accessory can be placed and fixed in the sample compartment. Figure 3.12 shows a schematic of the side view of the beam path through the reflection accessory. After passing through a wire-grid polarizer and being guided by the flat mirrors of the reflection accessory, incident light will be focused on the sample by a curved mirror (input mirror). The reflected light from the sample will be collected and sent towards the detector by another curved mirror (output mirror). The angle of incidence can be adjusted from 12° to 86° by rotating the curved mirrors. The input aperture's diameter can be controlled by computer. Decreasing the aperture's diameter will decrease the angular variation of the focused light, in expense of increasing the measurement's noise.

Measurement is performed on five different points for each sample, using an aperture diameter of 6 mm, 12° angle of incidence, and without using a polarizer. Measured reflectance spectra are normalized to the reflection from the aluminum mirror of the reflection accessory.

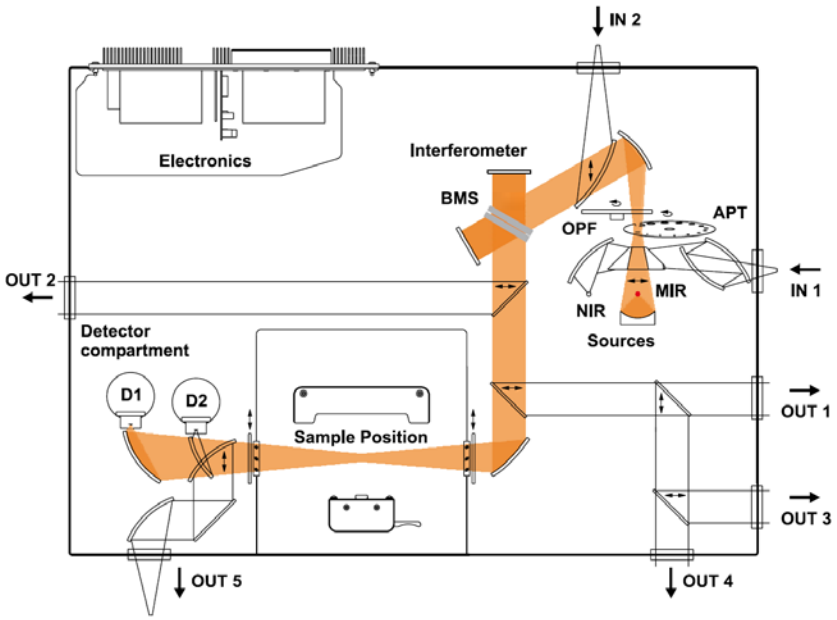

Fig. 3.11 Schematic top view of the beam path in VERTEX 70 spectrometer [21]

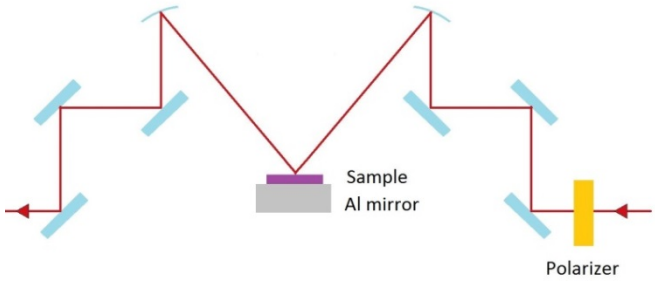

Fig. 3.12 Schematic side view of the beam path in the reflection accessory

The normal incidence reflectance spectra of the samples are calculated using the intensity transfer matrix method. Drude-Lorentz model (3.12) is used as the dielectric function of both doped and SI InP. Afterwards, in order to find the parameters of the Drude-Lorentz function for samples with different carrier concentrations, the calculated reflectance spectra are fitted to the measured ones using the Levenberg-Marquardt algorithm weighted with the inverse of the standard deviation of the measurements. In this regard, the measurement and the fitting process are first performed for the SI InP:Fe or n-doped InP:S substrates. The retrieved dielectric functions of the substrates are then used in the reflectance calculations and the fitting process for the epilayer/substrate system.

In all of the cases, the high frequency permittivity ε_∞ is considered to have a constant value equal to 9.55 [22]. Figure 3.8, which is repeated below for convenience, shows the measured and the fitted reflectance spectra of the SI InP:Fe substrate which is used to grow samples 1-9. Six Lorentzian terms, which account for the contribution of phonons to the optical dispersion, are considered for this case. The retrieved parameters of the dielectric function for SI InP:Fe are given in Tables 3.1 and 3.2, which are repeated below for convenience.

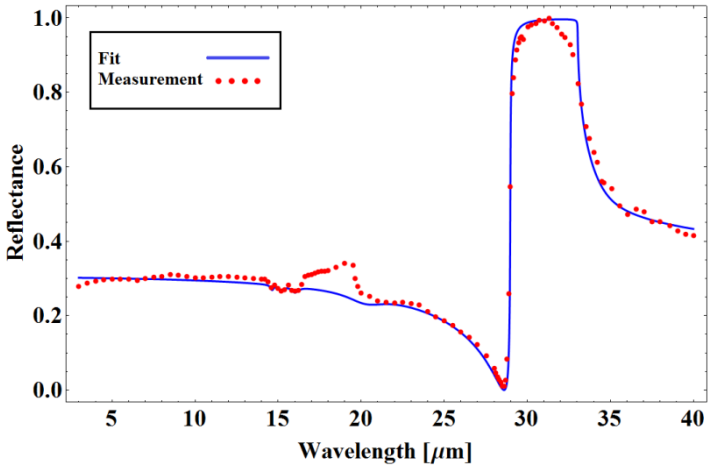

Fig. 3.8 (repeated) Measured and fitted reflectance spectra of SI InP:Fe substrate of samples 1-9

Table 3.1 (repeated) Parameters of the Lorentzian terms for the dielectric function of SI InP:Fe substrate of samples 1-9

j	1	2	3	4	5	6
S_j	1.7×10^{-4}	1.19×10^{-4}	6.13×10^{-5}	1.78×10^{-3}	1.56	2.85
Γ_j[THz]	0.51	0.4	0.28	1.33	1282.89	4.63×10^{-3}
$\omega_{f,j}$[THz]	18.73	19.76	20.49	14.74	14.82	9.08

Table 3.2 (repeated) Parameters of the Drude term for the dielectric function of SI InP:Fe substrate of samples 1-9

ω_p[THz]	γ[THz]	ε_∞
3.77×10^{-5}	3	9.55

Figure 3.13 shows the measured and the fitted reflectance spectra of the InP:S substrates which are used to grow samples 10 and 11. As it can be observed in the figure, only one Lorentzian dip at around 33 μm, which corresponds to a transverse optical (TO) phonon absorption [23], remains effective for these two cases where we have moderately n-doped InP. The retrieved dielectric function parameters together with the free carrier concentration measured by electrochemical capacitance voltage (ECV) measurements and also Hall method are given in Table 3.3.

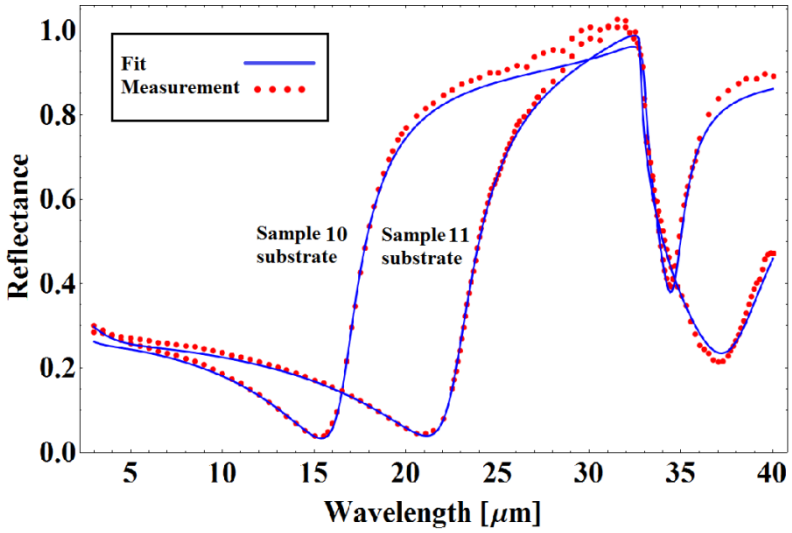

Fig. 3.13 Measured and fitted reflectance spectra of InP:S substrates of samples 10 and 11

Table 3.3 Parameters of the Drude-Lorentz dielectric function of InP:S substrate of samples 10 and 11

Substrate of sample	N (ECV) $\times10^{18}$ [cm^{-3}]	N (Hall) $\times10^{18}$ [cm^{-3}]	ω_p[THz]	γ[THz]	$\omega_{f,1}$[THz]	Γ_1[THz]	S_1
10	5.4	5.48	17.3	2.17	9.09	0.05	2.62
11	1.5	1.428	11.49	2.16	9.15	0.01	2.8

Using the parameters from Tables 3.1 and 3.2 for the SI InP:Fe substrate, the normal incidence reflectance spectra are calculated and fitted to the experimentally determined reflectance spectra for samples 1 to 9 as it is shown in Fig. 3.14. Similar to the case of moderately doped InP:S (substrates of samples 10 and 11), only one phonon absorption at around 33 μm remains effective and the others are overshadowed by the plasma resonance. Therefore, for the case of highly doped InP:Si only one Lorentzian term is considered in the Drude-Lorentz dielectric function. The thickness of the epilayer is also fitted for these samples in order to have more accurate results. The retrieved parameters for samples 1 to 9 are given in Table 3.4.

The reflectance spectra measurement and the fitting process are also done for samples 10 and 11 using the parameters given in Table 3.3 for their substrates. The measured and fitted reflectance spectra are shown in Fig. 3.15 and the retrieved parameters are given in Table 3.5. Since these two samples are grown on a doped substrate, their results are shown in a separate figure from samples 1 to 9 which are grown on a SI substrate. Fabry-Perot oscillations from the 3 μm thick epilayer of sample 11 can be observed below the plasma wavelength at 7.4 μm.

Figure 3.16 depicts real and imaginary parts of the permittivity of all the samples. As it can be seen in the figure, the crossover wavelength of InP:Si, where the permittivity becomes negative, can be tuned from 5.93 μm to 16.26 μm by changing the carrier concentration.

Figure 3.17 shows the retrieved plasma frequency versus the carrier concentration for samples 1 to 9. It includes the results from both Hall-effect and time-of-flight secondary ion mass spectrometry (TOF-SIMS) measurements together with their error bars. For all samples, the difference between the Si concentration measured by TOF-SIMS and the donors concentration measured by Hall-effect method is smaller than the error bars, which shows that the compensation ratio (ratio of the ionized acceptors to the ionized donor concentration) is smaller than the measurement limit. The theoretical plasma frequency is calculated from (3.11). The theoretical value of m^* for n-type InP proposed in [24] is used to calculate ω_p.

Based on the experimental results, a semi-empirical formula is derived for the plasma frequency of InP:Si as a function of the free carrier concentration (N) in the range between 0.35-4×10^{19} cm^{-3}:

$$\omega_p = \sqrt{AN\left(1 - \frac{B}{1.344 - CN^{\frac{1}{3}}}\right)} \tag{3.64}$$

in which $A = 918.43$ m^3/s^2, $B = 3.7 \times 10^{14}$, $C = 6.6 \times 10^5$ m and the units for N and the resulting ω_p are in m^{-3} and rad/s respectively. Here the term in the parenthesis

accounts for the changes in the band structure of InP when it is highly doped with Si. ω_p calculated from the Eq. (3.64) is also presented in Fig. 3.17.

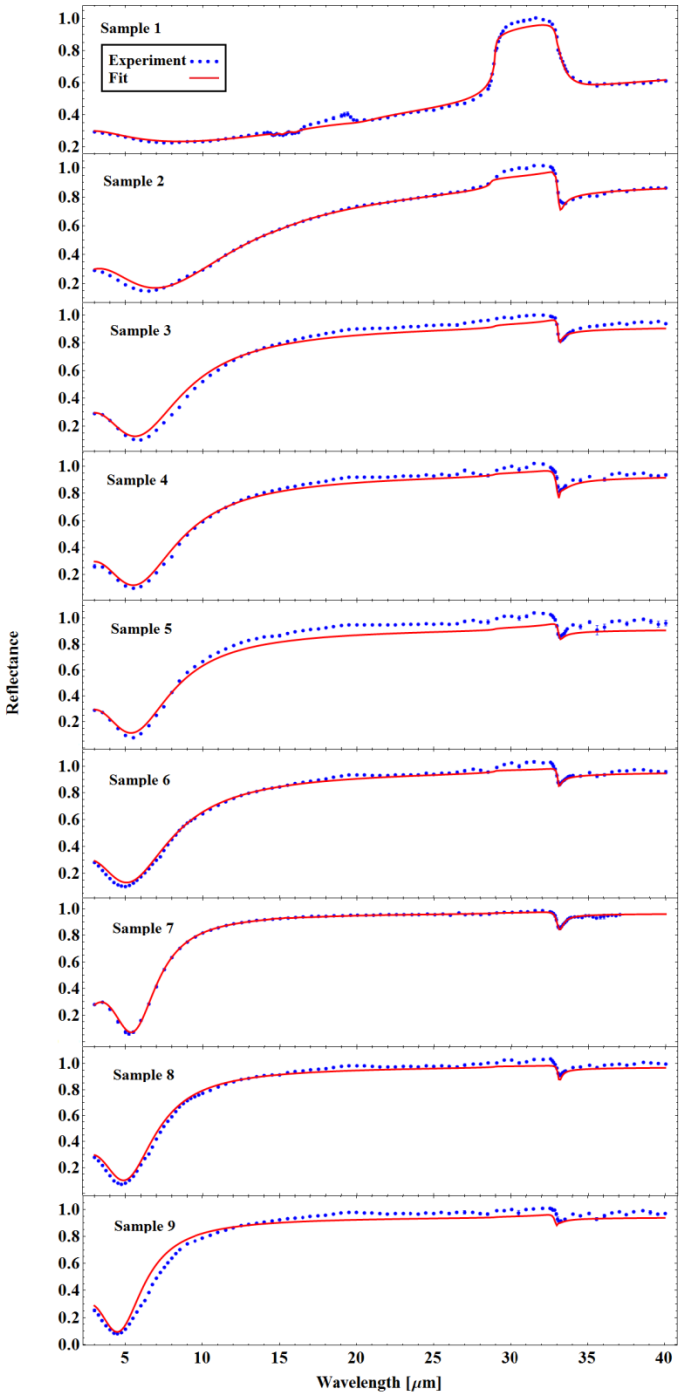

Fig. 3.14 Measured and fitted reflectance spectra of samples 1-9

Figure 3.18 shows the effective mass of electrons as a function of the carrier concentration calculated from Eq. (3.11) using the fitted values for ω_p, versus the

theoretically calculated effective mass from [24]. The discrepancy between the fitted and the theoretical values for ω_p in Fig. 3.17 can be attributed to the flaws in the theoretical formula for m^*, for example the effect of non-parabolicity of the conduction band [24], together with the fitting errors and also the errors in the Hall-effect measurements. These sources of error also explain the discrepancies in Fig. 3.18. Free electrons plasma damping (γ) is related to the mobility (μ) by

$$\gamma = \frac{e}{m^* \mu}. \tag{3.65}$$

Therefore, fluctuations in the values of γ with respect to the free carrier concentration (Table 3.4) are correlated with the fluctuations in the mobility values measured by the Hall-effect (Table 2.1).

The above mentioned method is also used to restore the ordinary and extraordinary permittivities of metamaterials which is presented in Appendix D.

Table 3.4 Parameters of the Drude-Lorentz dielectric function for samples 1-9

Sample	N (Hall) $\times 10^{19}$ [cm^{-3}]	ω_p[THz]	γ[THz]	$\omega_{f,1}$[THz]	Γ_1[THz]	S_1	Fitted thickness [nm]
1	0.35	18.43	1.45	9.09	0.081	2.18	485
2	0.858	28	1.91	9.09	0.032	1.52	570
3	1.71	37.12	2.85	9.08	0.04	1.91	533
4	1.94	38.17	2.36	9.12	0.07	3.66	531
5	2.35	39.87	3.45	9.07	0.056	1.89	536
6	2.7	41.41	1.38	9.08	0.036	1.52	475
7	3.09	43.57	1.71	9.11	0.082	2.86	651
8	3.39	45.6	1.09	9.08	0.045	1.72	516
9	3.87	50.5	3.49	9.12	0.082	2.52	503

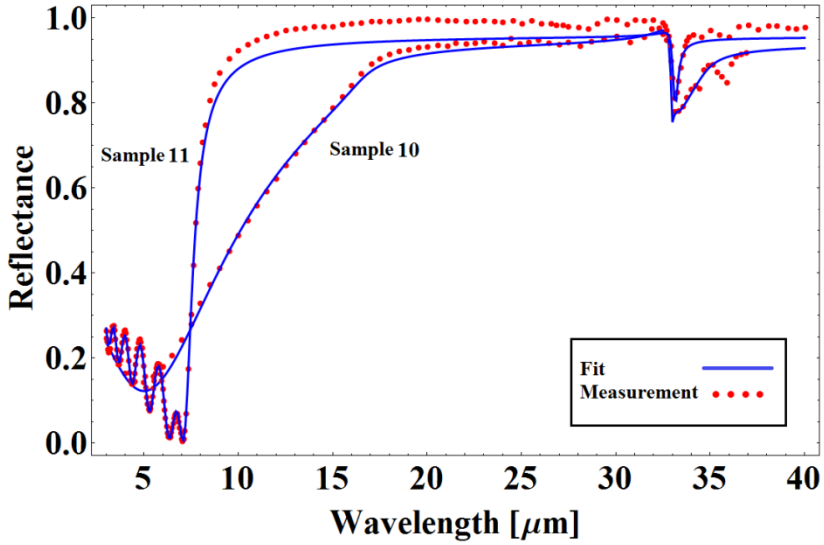

Fig. 3.15 Measured and fitted reflectance spectra of samples 10 and 11

Table 3.5 Parameters of the Drude-Lorentz dielectric function for samples 10 and 11

Sample	N (ECV) $\times 10^{19}$ [1/cm^3]	ω_p[THz]	γ[THz]	$\omega_{f,1}$[THz]	Γ_1[THz]	S_1	Thickness [nm]
10	3.15	39.27	2.76	9.13	0.036	3.83	400
11	2.7	40.47	2.82	9.09	0.048	1.91	3000

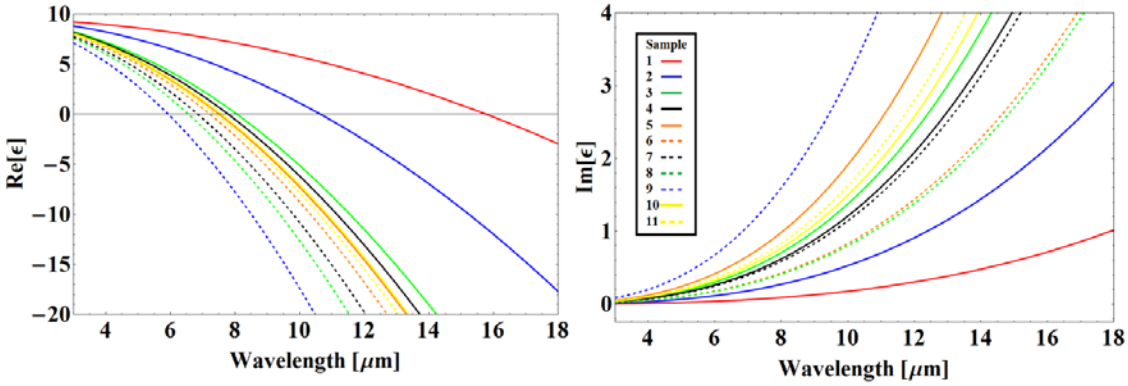

Fig. 3.16 Real and imaginary parts of the permittivity of all the samples

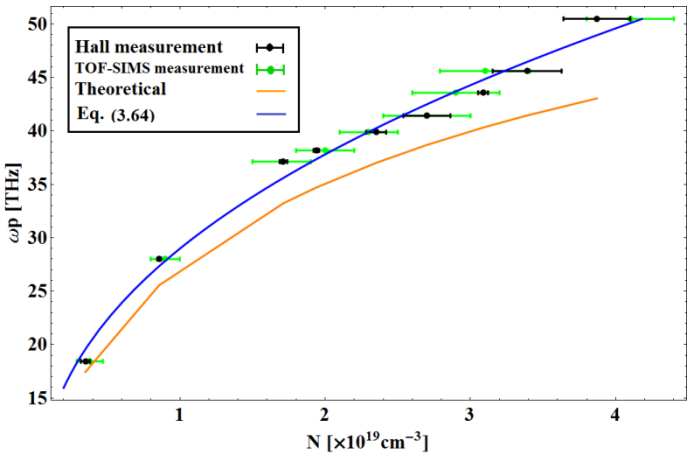

Fig. 3.17 ω_p versus carrier concentration from Hall and TOF-SIMS measurements and theoretical calculation for samples 1-9

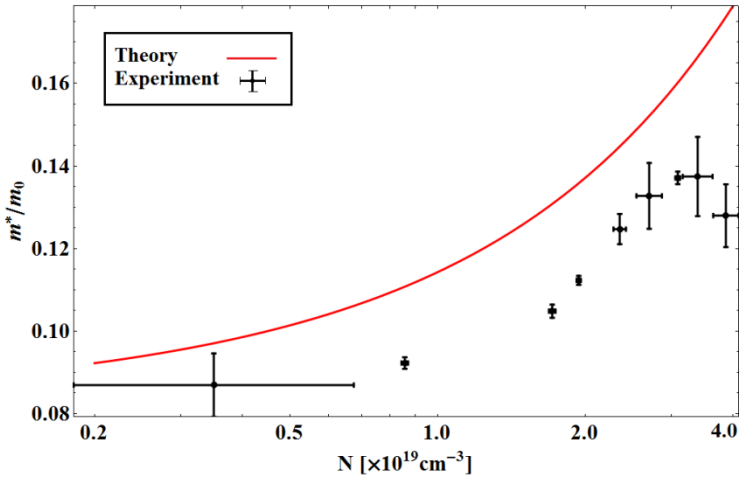

Fig. 3.18 Effective mass of electrons in InP:Si as a function of the carrier concentration

3.5. Comparison to other semiconductors

Having studied the optical properties of InP:Si in the mid-IR, we can compare its performance to other semiconductors, from plasmonic applications point of view. One of the unique properties of surface plasmon polaritons (SPPs) is the subwavelength spatial confinement of the electromagnetic field, which has led to many applications such as subwavelength waveguiding [25] and superlensing [26]. However, there is a tradeoff between spatial confinement and propagation length of SPPs: the better the confinement, the higher the losses and therefore the lower the propagation length. A good plasmonic material is the one with lower losses, better spatial confinement and longer propagation length.

According to the Drude model, even if two materials have the same plasma damping, the imaginary part of the permittivity, and consequently the optical losses, will be larger for the one with a shorter plasma wavelength. Therefore in order to be able to compare the plasmonic properties of two different materials, they need to have the same working range i.e. almost the same crossover wavelength. In this regard, four different semiconductor materials, whose data were available in the literature, namely n-doped Si (λ_p=5.54 µm), p-doped Si (λ_p=5.90 µm) [27], n-doped InSb (λ_p=6.84 µm) [28] and n-doped InAs (λ_p=6.3 µm) [29] are compared with sample 9 (λ_p=5.93 µm). Figure 3.19 shows real and imaginary parts of the permittivity for the above mentioned materials. Re[ε] for InP:Si is very close to that of n-InSb and in the same order with n-InAs, but Im[ε] for InP:Si is lower than the other semiconductors, thanks to the lower plasma damping and higher mobility of InP:Si.

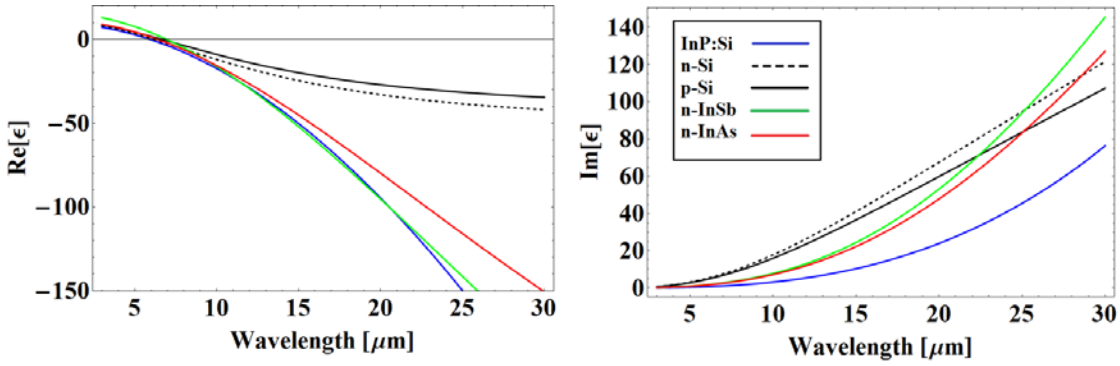

Fig. 3.19 Real and imaginary parts of the permittivity of the selected semiconductors together with sample 9

The dispersion relation for SPPs propagating at the interface between two media with opposite signs of the real parts of the dielectric functions ε_m and ε_d (e.g. a highly doped semiconductor and air) is given by

$$k_{spp} = k_0 \sqrt{\frac{\varepsilon_m \varepsilon_d}{\varepsilon_m + \varepsilon_d}} \tag{3.66}$$

where $k_0 = \frac{\omega}{c}$ is the wavevector of light in air [10].

Propagation length of surface plasmons L_p, is given by

$$L_p = \left(2\,\mathrm{Im}[k_{spp}]\right)^{-1}. \tag{3.67}$$

Localization (confinement factor) in air δ_d and in doped semiconductor δ_m are given by

$$\delta_{d/m} = \mathrm{Re}\left[\left(2\pi\sqrt{k_{spp}^2 - \varepsilon_{d/m}k_0^2}\right)^{-1}\right]. \tag{3.68}$$

The total SPP localization is defined as $\delta_{spp} = \delta_m + \delta_d$. Figure 3.20 shows the propagation lengths of surface plasmons, their localization, and figures of merit (FOMs) for sample 9 compared to other semiconductors. We use two figures of merits defined as [30]

$$\mathrm{FOM}_1 = L_p/\delta_{spp} \tag{3.69}$$

$$\mathrm{FOM}_2 = \mathrm{Re}[\varepsilon]^2/\mathrm{Im}[\varepsilon] \tag{3.70}$$

in order to quantify the tradeoff between the confinement and the propagation loss.

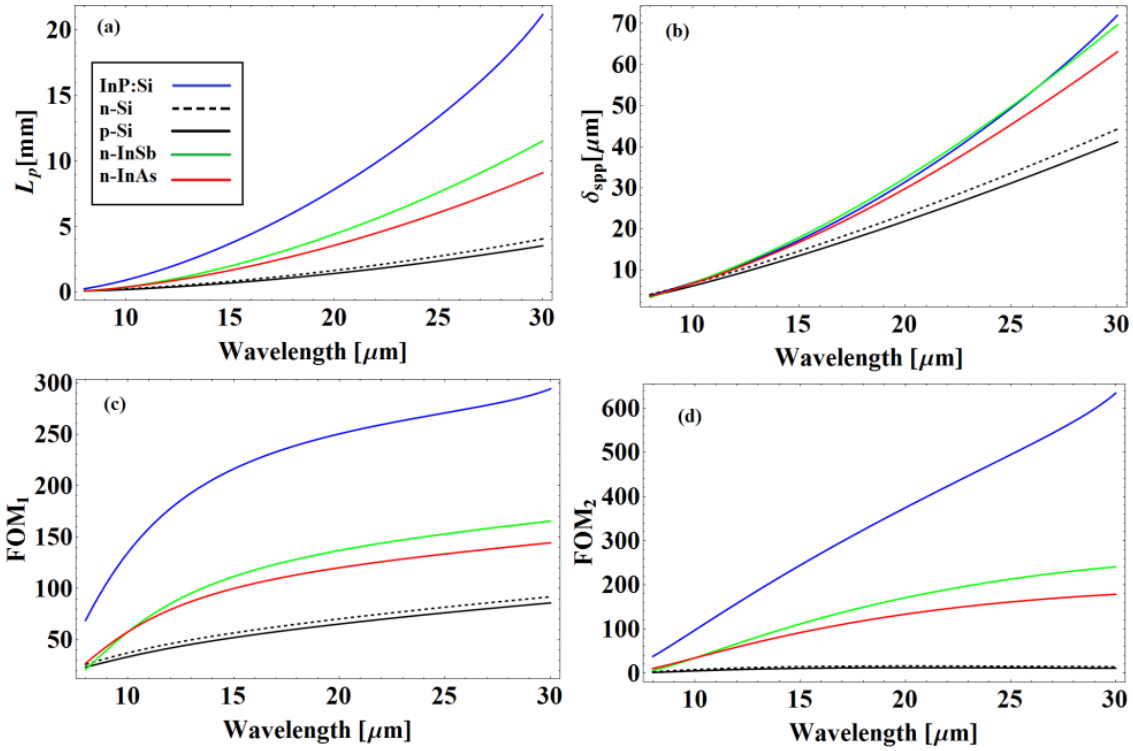

Fig. 3.20 (a) Propagation length, L_p, (b) localization, δ_{spp}, (c) figure of merit, L_p/δ_{spp} and (d) figure of merit $\mathrm{Re}[\varepsilon]^2/\mathrm{Im}[\varepsilon]$, for InP:Si in comparison with other selected semiconductors

From Figs. 3.20(a) and (b), we can see that the SPP propagation length in InP:Si is higher than the other semiconductors presented here thanks to the lower losses, and the localization of SPP's is among the others and very close to n-InSb. Both FOM_1 and FOM_2 which quantify the tradeoffs between localization and propagation length, strength and loss of SPP's respectively are higher for InP:Si.

In comparison to noble metals, in the mid-IR range, both real and imaginary parts of the permittivity of InP:Si are two orders of magnitude smaller which leads to better confinement of SPP's in expense of shorter propagation length. Nevertheless, tuanability of the plasma wavelength and damping is a very important feature of semiconductors which cannot be achieved in metals.

3.6. Summary

In this chapter, first a short literature review about the UV, visible and near-IR optical properties of InP is presented. Afterwards the Drude-Lorentz dielectric function is introduced as a suitable model for permittivity of InP in the mid-IR range. Transfer matrix of a slab for both normal and oblique incidence is derived and used to calculate the reflectance spectra of the samples with a highly doped InP:Si epilayer and a SI (or

low doped) InP substrate. The calculated reflectance spectra are then fitted to the measured ones in order to retrieve the parameters of the Drude-Lorentz dielectric function for samples with different free carrier concentrations. Experimentally determined plasma frequency and the effective mass of electrons are presented versus the free carrier concentration, and a semi-empirical formula for calculating the plasma frequency of InP:Si is derived. In comparison to other semiconductors, InP:Si is found to have superior plasmonic properties, in terms of surface confinement and propagation length, owing to the lower losses, which makes it a promising candidate for mid-IR plasmonics where noble metals suffer from high losses.

References

1. S. Adachi, "Model dielectric constants of GaP, GaAs, GaSb, InP, InAs, and Insb," Phys. Rev. B. **35**(14), 7454-7463 (1987).
2. D. E. Aspnes, and A. A. Studna, "Dielectric functions and optical parameters of Si, Ge, GaP, GaAs, GaSb, InP, InAs, and InSb from 1.5 to 6.0 eV," Phys. Rev. B. **27**(2), 985-1009 (1982).
3. H. Burkhard, H. W. Dinges, and E. Kuphal, "Optical properties of $In_{1-x}Ga_xP_{1-y}As_y$, InP, GaAs, and GaP determined by ellipsometry," J. Appl. Phys. **53**(1), 655-662 (1982).
4. A. De, and C. E. Pryor, "Optical dielectric functions of III-V semiconductors in wurtzite phase," https://arxiv.org/abs/1011.3081.
5. A. B. Djurišić, Y. Chan, and E. H. Li, "The model dielectric function: application to GaSb and InP," Semicond. Sci. Technol. **16**, 902-908 (2001).
6. S. M. Kelso, D. E. Aspnes, M. A. Pollack, and R. E. Nahory, "Optical properties of $In_{1-x}Ga_xAs_yP_{1-y}$ from 1.5 to 6.0 eV determined by spectroscopic ellipsometry," Phys. Rev. B **26**(12), 6669-6681 (1982).
7. www.ioffe.ru.
8. M. Bugajski, and W. Lewandowski, "Concentration-dependent absorption and photoluminescence of n-type InP," J. Appl. Phys. **57**(2), 521-530 (1985).
9. S. C. Jain, J. M. M. Gregor, and D. J. Roulston, "Band-gap narrowing in novel III-V semiconductors," J. Appl. Phys. **68**(7), 3747-3749 (1990).
10. S. A. Maier, Plasmonics: Fundamentals and Applications (Springer, 2007).
11. R. C. Jayasinghe, Y. F. Lao, A. G. U. Perera, M. Hammar, C. F. Cao, and H. Z. Wu, "Plasma frequency and dielectric function dependence on doping and temperature for p-type indium phosphide epitaxial films," J. Phys.: Condens. Matter **24**(43), 435803 (2012).
12. H. Q. Zheng, K. Radahakrishnan, S. F. Yoon, and G. I. Ng, "Electrical and optical properties of Si-doped InP grown by solid source molecular beam epitaxy using a valved phosphorus cracker cell," J. Appl. Phys. **87**(11), 7988-7993 (2000).
13. M. M. El-Nahass, S. B. Youssef, and H. A. M. Ali, "Optical properties of sulfur doped InP single crystals," Physica A: Statistical Mechanics and its Applications **402**, 216–223 (2014).

14. Q. H. Hua, G. P. Li, X. K. He, Q. Wang, and T.N. Sun, “Infrared reflectance study of n-type InP grown by the LEC method,” Mater. Lett. **3**(3), 93-97 (1985).
15. M. Cada, D. Blazek, J. Pistora, K. Postava, and P. Siroky, “Theoretical and experimental study of plasmonic effects in heavily doped gallium arsenide and indium phosphide,” Opt. Mater. Express **5**(2), 340-352 (2015).
16. S. J. Orfanidis, Electromagnetic Waves and Antennas (Rutgers University, 2014).
17. L. A. Coldren, S. W. Corzine, and M. L. Mašanović, Diode Lasers and Photonic Integrated Circuits (John Wiley & Sons, 2012).
18. C. J. Gabriel, and A. Nedoluha, “Transmittance and Reflectance of Systems of Thin and Thick Layers,” Opt. Acta, **18**(6), 415-423 (1971).
19. T. W. Noh, P. H. Song, S. Lee, D. C. Harris, J. R. Gaines, and J. C. Garland, “Far-infrared studies of two-dimensional random metal-insulator composites”, Phys. Rev. B **46**(7), 4212-4222.
20. W. H. Press, B. P. Flannery, S. A. Teukolsky, and W. T. Vetterling, Numerical Recipes (Cambridge University, 1986).
21. www.bruker.com
22. W. Walukiewicz, J. Lagowski, L. Jastrzebski, P. Rava, M. Lichtensteiger, C. H. Gatos, and H. C. Gatos, “Electron mobility and free-carrier absorption in InP; determination of the compensation ratio,” J. Appl. Phys. **51**(5), 2659-2668 (1980).
23. G. F. Alfrey, and P. H. Borcherds, “Phonon frequencies from the Raman spectrum of indium phosphide,” J. Phys. C: Solid State Phys. **5**, L275-L278 (1972).
24. M. Cardona, “Temperature dependence of the refractive index and the polarizability of free carriers in some III-V semiconductors,” in *proceedings of the international conference on semiconductor physics* (1960), pp. 388-394.
25. J. A. Dionne, L. A. Sweatlock, H. A. Atwater, and A. Polman, “Planar metal plasmon waveguides: frequency-dependent dispersion, propagation, localization, and loss beyond the free electron model,” Phys. Rev. B **72**(7), 075405 (2005).
26. J. B. Pendry, “Negative refraction makes a perfect lens,” Phys. Rev. Lett. **85**(18), 3966 (2000).
27. J. C. Ginn, R. L. Jarecki Jr., E. A. Shaner, and P. S. Davids, “Infrared plasmons on heavily-doped silicon,” J. Appl. Phys. **110**(4), 043110 (2011).
28. S. Law, R. Liu, and D. Wasserman, “Doped semiconductors with band-edge plasma frequencies,” J. Vac. Sci. Technol. B **32**(5), 052601 (2014).
29. S. Law, D. C. Adams, A. M. Taylor, and D. Wasserman, “Mid-infrared designer metals,” Opt. Express **20**(11), 12155-12165 (2012).
30. G. V. Naik, V. M. Shalaev, and A. Boltasseva, “Alternative Plasmonic Materials: Beyond Gold and Silver,” Adv. Mater. **25**(24), 3264-3294 (2013).

4. SURFACE PLASMON POLARITONS ON InP:Si SURFACE

4.1. Introduction to surface plasmon polaritons

Surface plasmon polaritons (SPPs) are surface waves confined to the interface between a dielectric and conductive materials as a result of coupling of an external electromagnetic field with the collective oscillation of free conduction electrons. Mathematical descriptions of these phenomena date back to early 1900's, but it was not until the middle of the 20th century when the experimental observations were linked to the theory [1]. Boosted by advances in nanofabrication techniques, the field of plasmonics was reborn in the second half of the 20th century [2]. Publication of Ebbesen *et al*. [3] in 1998 on extraordinary optical transmission propelled the interest to this field, and plasmonics quickly became one of the main research topics in nanophotonics due to broad potential applications. Unique properties of SPPs such as the subwavelength spatial confinement and high sensitivity of the dispersion to the surrounding dielectric material are exploited in subwavelength waveguides [4], surface plasmon lasers (spasers) [5], photovoltaics [6], optical superlenses [7] and plasmonic sensors [8].

Traditionally noble metals are used as plasmonic materials due to their abundant free electrons in the conduction band. However, their large real and imaginary parts of the permittivity, especially in the infrared (IR) range, result in high loss and weak confinement to the surface (see section 3.5). Apart from these material shortcomings, technological limitations pose an obstacle to integrating metals in conventional CMOS fabrication processes. During the last several years, alternative plasmonic materials such as conductive oxides, polar materials, graphene and doped semiconductors have become an emerging research field [9-13]. Each group of alternatives has its own preferential

wavelength range due to the available free carrier concentrations and mobilities. Semiconductors benefit from lower optical losses resulting from their high mobilities [14], drastic tunability of plasmonic properties via doping, the possibility of active control of the carrier concentration by charge depletion [15] and full CMOS compatibility. In this regard doped Si [16,17], Ge [18], InAs:Si [19], InGaAsBi:Si [20] and InAsSb:Si [21] have been challenged for plasmonic properties.

InP as a direct bandgap III-V semiconductor is one of the most common materials in optoelectronic applications which has the advantages of easy integration and being compatible with conventional III-V optoelectronic devices and their fabrication processes. The InP based material system is conventionally used for telecom applications at 1300 and 1550 nm wavelengths. However, in spite of being the workhorse of the telecom photonics, literature on plasmonic properties of InP is scarce.

Mid-IR optical properties of InP:Si for different carrier concentrations, which are retrieved in the previous chapter, will be used in this chapter to simulate the excitation of SPPs. Simulation results will be verified by experiments.

Maxwell equations of macroscopic electromagnetism should be used to study SPP's at the interface between a dielectric and a conductive material. These equations describe how the electric and magnetic fields are related to the charges and currents and the changes in each other [2]:

$$\nabla . \mathbf{D} = \rho_{ext} \tag{4.1a}$$

$$\nabla . \mathbf{B} = 0 \tag{4.1b}$$

$$\nabla \times \mathbf{E} = -\frac{\partial \mathbf{B}}{\partial t} \tag{4.1c}$$

$$\nabla \times \mathbf{H} = \mathbf{J}_{ext} + \frac{\partial \mathbf{D}}{\partial t} \tag{4.1d}$$

in which **E** and **H** are the electric and the magnetic fields respectively, **D** is the dielectric displacement, **B** is the magnetic flux density, ρ_{ext} and $\mathbf{J}_{ext}$ are the external charge and current densities respectively.

The constitutive relations are also defined as:

$$\mathbf{D} = \varepsilon_0 \varepsilon \mathbf{E} \tag{4.2a}$$

$$\mathbf{B} = \mu_0 \mu \mathbf{H} \tag{4.2b}$$

where ε_0 and μ_0 are the electric permittivity and the magnetic permeability of vacuum respectively and ε and μ are the relative permittivity and permeability of the material respectively.

In the absence of external current and charge densities, (4.1c) and (4.1d) can be combined to give

$$\nabla \times \nabla \times \mathbf{E} = -\mu_0 \frac{\partial^2 \mathbf{D}}{\partial t^2}. \tag{4.3}$$

Using the "curl of the curl" identity, $\nabla \times \nabla \times \mathbf{E} \equiv \nabla(\nabla . \mathbf{E}) - \nabla^2 \mathbf{E}$, in (4.3) together with $\nabla . (\varepsilon \mathbf{E}) \equiv \mathbf{E} . \nabla \varepsilon + \varepsilon \nabla . \mathbf{E}$, keeping in mind that in the absence of external charges $\nabla . \mathbf{D} = 0$, one will get to

$$\nabla \left(-\frac{1}{\varepsilon} \mathbf{E} . \nabla \varepsilon \right) - \nabla^2 \mathbf{E} = -\mu_0 \varepsilon_0 \varepsilon \frac{\partial^2 \mathbf{E}}{\partial t^2}. \tag{4.4}$$

If the relative permittivity of the material be spatially constant over a wavelength, $\nabla \varepsilon = 0$ and (4.4) reduces to the wave equation

$$\nabla^2 \mathbf{E} - \frac{\varepsilon}{c^2} \frac{\partial^2 \mathbf{E}}{\partial t^2} = 0 \tag{4.5}$$

in which c is the speed of light defined as $c^2 = \frac{1}{\mu_0 \varepsilon_0}$.

Assuming a harmonic time dependence in form of $e^{-i\omega t}$ for the electric field, equation (4.5) can be written in form of a Helmholtz equation [2]

$$\nabla^2 \mathbf{E} + k_0^2 \varepsilon \mathbf{E} = 0 \tag{4.6}$$

in which $k_0 = \frac{\omega}{c}$ is the wavevector of light in vacuum.

Consider the interface between a dielectric material with permittivity ε_d and a conductive material with permittivity ε_m as in Fig. 4.1. An electric field propagating in the x direction, with no spatial variation in the y direction will have the form $\mathbf{E}(x, y, z) = \mathbf{E}(z) e^{i\beta x}$, with the complex $\beta = k_x$ called the propagation constant or the wavenumber in the x direction. Using this expression in (4.6) yields

$$\frac{\partial^2 \mathbf{E}(z)}{\partial z^2} + (k_0^2 \varepsilon - \beta^2) \mathbf{E} = 0 . \tag{4.7}$$

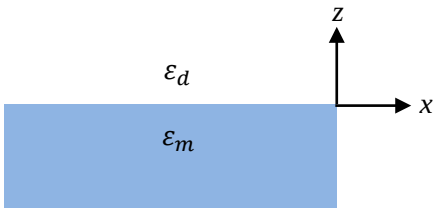

Fig. 4.1 Geometry of the SPP propagation problem

Regarding the harmonic time dependence of the electric field ($\frac{\partial}{\partial t} = -i\omega$) and the homogeneity in the y direction ($\frac{\partial}{\partial y} = 0$), for propagation along the x direction ($\frac{\partial}{\partial x} = i\beta$), the Maxwell curl equations (4.1c) and (4.1d) read

$$\frac{\partial E_y}{\partial z} = -\mu_0 i\omega H_x \tag{4.8a}$$

$$\frac{\partial E_x}{\partial z} - i\beta E_z = \mu_0 i\omega H_y \tag{4.8b}$$

$$i\beta E_y = \mu_0 i\omega H_z \tag{4.8c}$$

$$\frac{\partial H_y}{\partial z} = \varepsilon_0 \varepsilon i\omega E_x \tag{4.8d}$$

$$\frac{\partial H_x}{\partial z} - i\beta H_z = -\varepsilon_0 \varepsilon i\omega E_y \tag{4.8e}$$

$$i\beta H_y = -\varepsilon_0 \varepsilon i\omega E_z \, . \tag{4.8f}$$

Equations (4.8b), (4.8d) and (4.8f) correspond to the transverse magnetic (TM) polarization in which only the field components E_x, E_z and H_y are nonzero, and the other three equations correspond to the transverse electric (TE) polarization where only the field components H_x, H_z and E_y are nonzero. Starting from TM modes and rearranging (4.8d) and (4.8f) as

$$\begin{aligned} E_x &= -i\frac{1}{\omega\varepsilon_0\varepsilon}\frac{\partial H_y}{\partial z} \\ E_z &= -\frac{\beta}{\omega\varepsilon_0\varepsilon}H_y \end{aligned} \tag{4.9}$$

and using them in (4.8b) yields the wave equation for the TM modes

$$\frac{\partial^2 H_y}{\partial z^2} + (k_0^2\varepsilon - \beta^2)H_y = 0 \, . \tag{4.10}$$

Rearranging (4.8a) and (4.8c) for TE modes as

$$\begin{aligned} H_x &= i\frac{1}{\omega\mu_0}\frac{\partial E_y}{\partial z} \\ H_z &= \frac{\beta}{\omega\mu_0}E_y \end{aligned} \tag{4.11}$$

and using them in (4.8e) yields the wave equation for TE modes

$$\frac{\partial^2 E_y}{\partial z^2} + (k_0^2\varepsilon - \beta^2)E_y = 0 \, . \tag{4.12}$$

As it is implied in the definition of the SPP's as surface waves, we are looking for solutions that correspond to propagating waves in the *x* direction which are confined to the interface, or in other words, solutions with evanescent decay in the *z* direction. Therefore, for TM modes, solution of (4.9) and (4.10) for $z>0$ will be

$$H_y(z) = A_2 e^{i\beta x} e^{-k_2 z}$$
$$E_x(z) = iA_2 \frac{1}{\omega \varepsilon_0 \varepsilon_d} k_2 e^{i\beta x} e^{-k_2 z} \tag{4.13}$$
$$E_z(z) = -A_1 \frac{\beta}{\omega \varepsilon_0 \varepsilon_d} e^{i\beta x} e^{-k_2 z}$$

and for $z<0$

$$H_y(z) = A_1 e^{i\beta x} e^{k_1 z}$$
$$E_x(z) = -iA_1 \frac{1}{\omega \varepsilon_0 \varepsilon_m} k_1 e^{i\beta x} e^{k_1 z} \tag{4.14}$$
$$E_z(z) = -A_1 \frac{\beta}{\omega \varepsilon_0 \varepsilon_m} e^{i\beta x} e^{k_1 z} .$$

k_i (i=1,2) is the component of the wavevector in the z direction. Continuity of H_y and $\varepsilon_i E_z$ at the interface requires that $A_1 = A_2$ and [2]

$$\frac{k_2}{k_1} = -\frac{\varepsilon_d}{\varepsilon_m} . \tag{4.15}$$

According to (4.13) and (4.14), considering the requirement for evanescent decay of the surface waves in the z direction, both k_1 and k_2 should have positive signs which implies that $\mathrm{Re}[\varepsilon_m]$ and ε_d should have opposite signs. This is the basic condition for existence of SPP's at the interface between two materials. Inserting H_y from (4.13) and (4.14) in (4.10) yields

$$k_1^2 = \beta^2 - k_0^2 \varepsilon_m$$
$$k_2^2 = \beta^2 - k_0^2 \varepsilon_d . \tag{4.16}$$

Using (4.15) and (4.16), we get to the "*dispersion*" relation for SPP's:

$$\beta = k_{SPP} = k_0 \sqrt{\frac{\varepsilon_m \varepsilon_d}{\varepsilon_m + \varepsilon_d}} . \tag{4.17}$$

For TE modes, solution of (4.11) and (4.12) for $z>0$ will be

$$E_y(z) = A_2 e^{i\beta x} e^{-k_2 z}$$
$$H_x(z) = -iA_2 \frac{1}{\omega \mu_0} k_2 e^{i\beta x} e^{-k_2 z} \tag{4.18}$$
$$H_z(z) = A_2 \frac{\beta}{\omega \mu_0} e^{i\beta x} e^{-k_2 z}$$

and for $z<0$

$$E_y(z) = A_1 e^{i\beta x} e^{k_1 z}$$
$$H_x(z) = iA_1 \frac{1}{\omega \mu_0} k_1 e^{i\beta x} e^{k_1 z} \tag{4.19}$$
$$H_z(z) = A_1 \frac{\beta}{\omega \mu_0} e^{i\beta x} e^{k_1 z} .$$

Continuity of E_y and H_x at the interface yields

$$A_1(k_1 + k_2) = 0\,. \tag{4.20}$$

Requirement for the evanescent decay of the surface waves in the z direction implies that both k_1 and k_2 be positive. Therefore (4.20) holds only if $A_1 = A_2 = 0$, which means that no SPP exist for TE polarization.

Figure 4.2 shows the dispersion graph for SPP's on the interface between highly doped InP:Si (sample 7: Chapter 3) and air, together with the dispersion graph for the same sample when the free carrier and phonon damping mechanisms are ignored. In the transparency regime where the frequency is higher than the plasma frequency of the conductive material, light can pass through the material and the dispersion curve lies on the left side of the light line of air. In lower frequencies, the dispersion curve lies on the right side of the light line which shows the bound nature of SPPs. In order to couple photons to SPPs, both need to have the same frequency and momentum, but according to the dispersion relation, for a given frequency, momentum of photons is smaller than that for SPPs. Consequently, light cannot directly couple to SPPs and special phase-matching techniques are required to excite them.

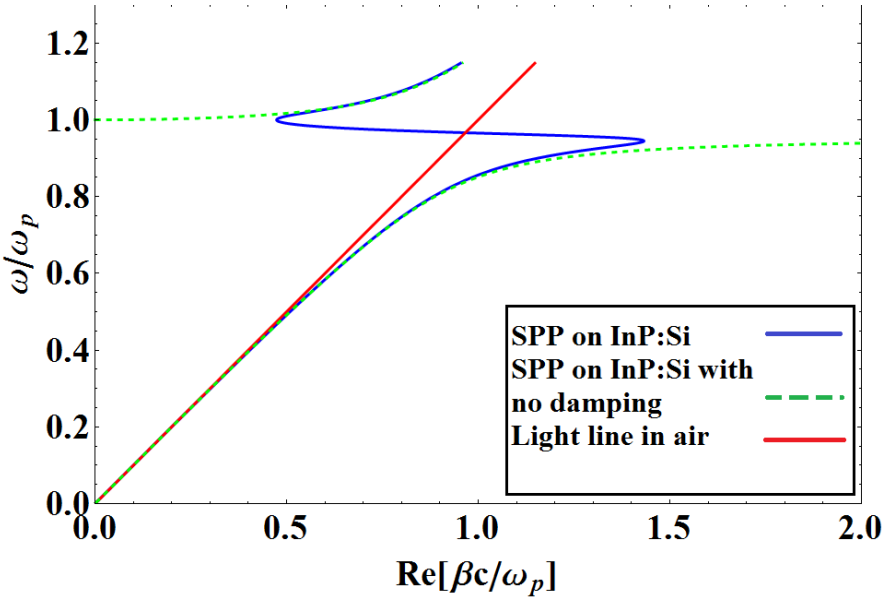

Fig. 4.2 SPP dispersion curves on the interface between InP:Si and air together with the light line

4.2. Prism coupling

4.2.1. Theory

One of the techniques that can be used to match the momentum of light and SPPs is prism coupling. In this method a prism with refractive index n_p is placed above the surface of the conductive sample, separated with an airgap smaller than the wavelength of light [Fig. 4.3(a)]. Light that passes through the prism with an angle of incidence φ_i larger than the critical angle between air and the prism ($\varphi_c = \arcsin\frac{n_{air}}{n_p}$) undergoes total internal reflection. The evanescent tail of the reflected light leaks through the airgap and reaches to the surface of the sample, with its parallel to the surface component of the wavevector given by

$$k_x = n_p k_0 \sin\varphi_i \,, \tag{4.21}$$

which is able to excite SPPs. The above mentioned method is called Otto configuration [22] and its drawback is the difficulty in maintaining a subwavelength airgap between the sample and the prism. There is another geometry, called Kretschmann configuration [23], in which a thin film of the conductive material is directly deposited on the bottom of the prism. Evanescent tail of the light passes through the film and couples to SPPs on the interface between air and the conductive material.

4.2.2. Experiment

Sample 10 (see Chapter 3) with a 400 nm thick highly doped InP:Si epilayer (N=3.15×10^{19} cm^{-3}) on top of low doped InP:S substrate (N=5.4×10^{18} cm^{-3}) is used for this experiment. To elucidate the excitation of plasmons on the highly doped layer of InP:Si, we employ a high refractive index hemi-spherical germanium prism ($n_p = 4$). The reflection spectra in such configuration are theoretically analyzed using the transfer-matrix formalism [24]. In the analyzed configuration, a four-layer structure of Ge prism/Air gap/InP:Si/InP:S substrate is assumed as illustrated in Fig. 4.3(a). The Drude-Lorentz model (3.12) with the sample 10 parameters for the epilayer and its substrate is exploited.

In Fig. 4.3(b), numerical results are shown for TM-polarized incident light. The dispersion of SPPs on air/InP:Si and InP:Si/InP:S substrate interfaces is calculated by using Eq. (4.17). These dispersions are also plotted in Fig. 4.3(b) to give an insight into two kinds of plasmons existing in our system, namely one supported at the air/InP:Si interface (blue diamonds) and another at the InP:Si/InP:S (red circles) interface. From the dispersion of a semi-infinite arrangement and the simulation of reflectance, we can deduce that for $\lambda > 8$ μm a SPP on the air/InP:Si interface emerges until around $\lambda = 14$ μm, and from $\lambda = 11$ μm another SPP supported at the InP:Si/InP:S substrate interface appears. Note that the second plasmon mode disappears around $\lambda = 15$ μm because the

permittivity of the InP:S substrate also becomes negative at λ = 16.6 μm and plasmons at the InP:Si/InP:S interface cannot be supported anymore.

In our experimental setup based on the Otto-Kretschmann configuration [Fig. 4.3(a)], a hemi-spherical Ge prism is placed on the sample with some air gap between the prism and InP:Si layer. The thickness of the air gap $d_c = 400$ nm is evaluated by fitting the experimental results with the simulated reflection spectra. The hemi-spherical Ge prism is adopted for its high refractive index and transparency in the mid-IR region. A wire-grid polarizer is used in the Fourier transform infrared spectrometer (FTIR) setup (See Section 3.4 for details of the setup) in order to provide TM-polarized incident light, which is focused on the structure through a parabolic mirror and the Ge prism. Incident light is directed onto the surface with angle of incidence φ_{in} which is manually controlled by using a goniometer with the increment of 2°. Series of reflection spectra are joined to form a reflectance map as shown in Fig. 4.3(c). Note that the critical angle between the Ge prism and air is 14.47°, therefore the simulation and experiment are conducted well above this angle.

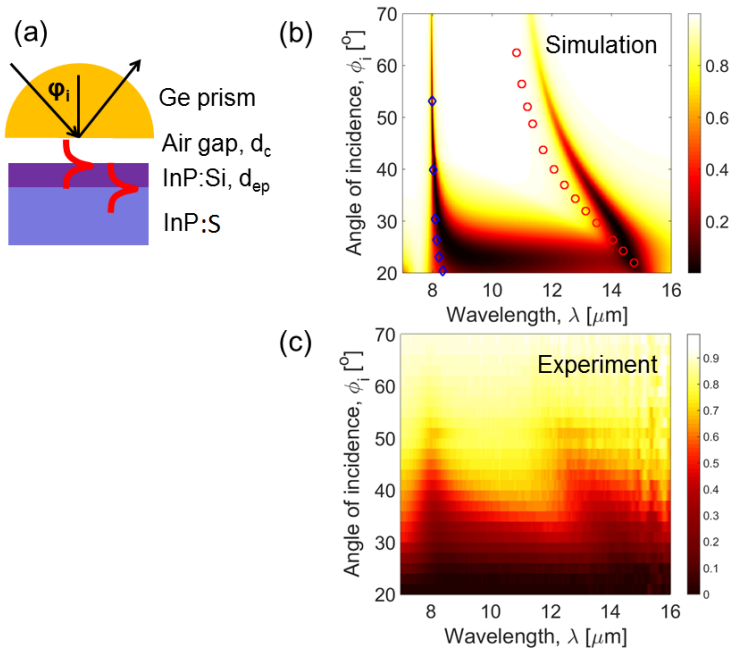

Fig. 4.3 Illustration of Ge prism/Air gap/InP:Si/InP:S substrate structure with air gap of 400 nm and 400 nm thick InP:Si layer. (b) Simulated and (c) measured reflectance from the structure under consideration. In (b), the dispersion of plasmons supported at the air gap/InP:Si interface (blue diamond) and those at the InP:Si/InP:S substrate interface (red circle) are shown to clarify the origin of two plasmons.

The acquired reflection data as shown in Fig. 4.3(c) reproduces the theoretical predictions for plasmons on two different interfaces, showing two corresponding reflection bands. All measured reflection dips agree with the theoretical expectations in

the wavelength range of λ = 8 – 15 μm. Importantly, the agreement between the observed and theoretical expectations demonstrates that the highly doped InP is an effective plasmonics material for the mid-IR region, as well as the validity of our fitting method to determine the permittivity of the plasmonic layer. The difference between simulations and experiment in Figs. 4.3(b) and 4.3(c) is mainly due to the measurement uncertainties in the FTIR setup including inherent noise of the system, angular uncertainty and polarization mixture at high angles of incidence. Calculation of the beam path in the FTIR setup shows that there is an angular variation of around ±1.75° in the incident light beam which can widen the observed SPP coupling dips in the reflectance spectra. In addition, even though only TM polarized light passes through the polarizer at the input, a small portion of it will be converted to TE polarized light after focusing by the parabolic mirrors of the FTIR reflection accessory. This effect, which is more pronounced at bigger incident angles, will decrease the intensity of the SPP coupling dips in the reflectance spectra.

4.3. Grating coupling

4.3.1. Theory

Diffraction of light from a periodic grating is governed by Bragg's law

$$k_{out} = mk_g - k_{in}\,, \tag{4.22}$$

where $k_{out} = k_0 \sin\theta_{out}$, $k_{in} = k_0 \sin\theta_{in}$ and $k_g = \frac{2\pi}{\Lambda}$ are the wave vectors of the diffracted wave, incident wave and grating respectively, Λ is the grating period and *m* is the diffraction order.

Efficiency of the diffraction orders which is defined as the ratio of the intensity of diffracted light to the intensity of the incident light is given by [25]

$$I = \frac{\sin^2(m\pi D)}{m^2\pi^2} \tag{4.23}$$

in which *D* is the duty cycle of the grating. Figure 4.4 shows the efficiency of diffraction orders as a function of the duty cycle.

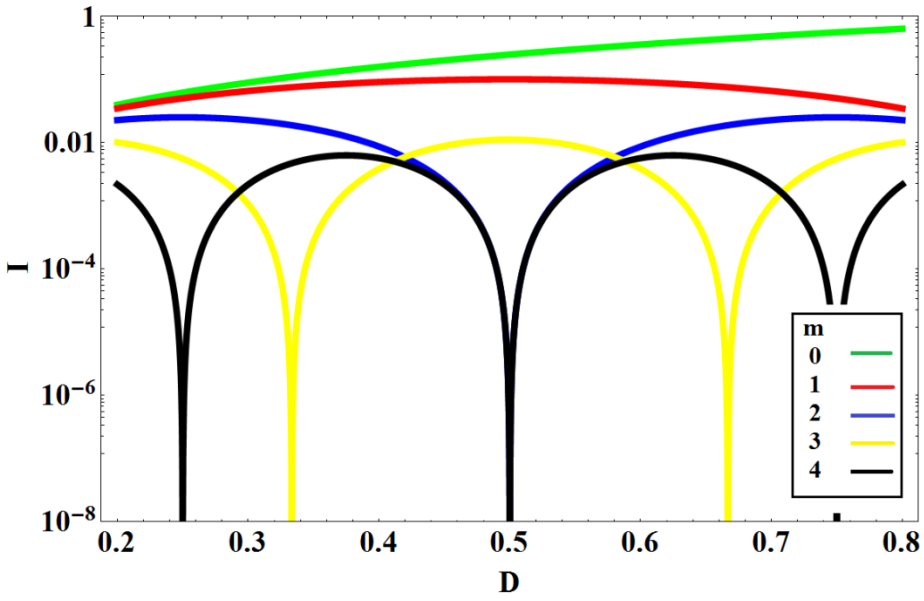

Fig. 4.4 Efficiency of the diffraction orders as a function of the duty cycle

According to the efficiency of the diffraction orders, for a grating with a duty cycle of 50% all even diffraction orders must vanish and *m* will be an odd integer.

On the other hand, light can couple to SPPs by the grating if the momentum matching condition is satisfied [2]

$$k_{SPP} = nk_g + k_{in} \, . \tag{4.24}$$

As explained above, for a grating with a duty cycle of 50%, *n* will also be an odd integer.

The excited SPP wave can reversely be diffracted by the grating into free space, with a wave vector given by

$$k_{out} = mk_g - k_{SPP} \, . \tag{4.25}$$

Applying Eq. (4.24) in Eq. (4.25) yields a modified diffraction law [26]

$$k_{out} = (m - n)k_g - k_{in} \, , \tag{4.26}$$

where $(m - n)$ is now an even integer. This manifests the emerging of even diffraction orders banned by Bragg's law. Such process, when prohibited diffraction orders are facilitated by assistance of SPPs is currently considered as a very promising direction in sensing and new grating functionalities [27,28]. Figure 4.5 shows the coupling condition in terms of the wavelength and the angle of incidence for different modes of SPPs, plotted using (4.24) and the Drude-Lorentz model with material parameters of sample 11 (see Chapter 3).

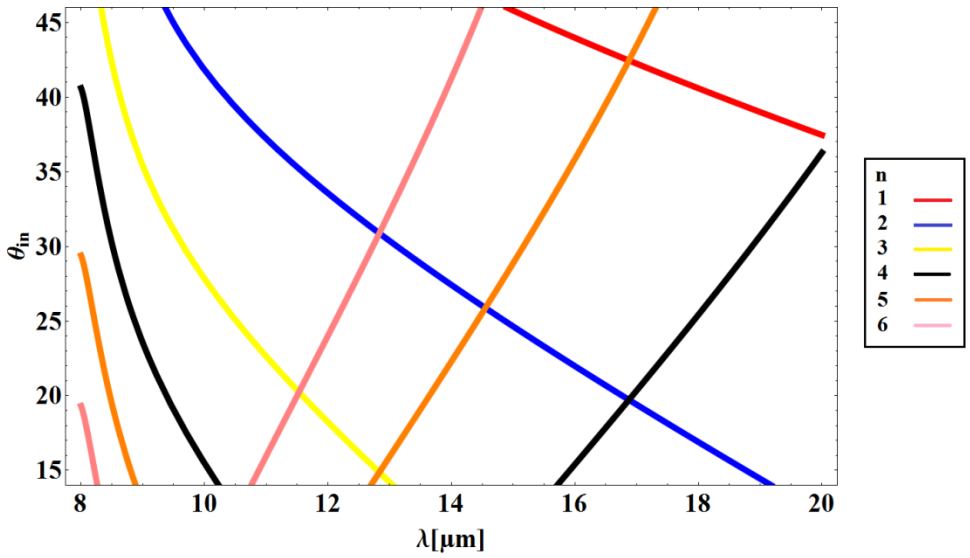

Fig. 4.5 Grating coupling condition for different modes

The reflectance spectra from the grating are simulated by the "Radio frequency: Electromagnetic wave, frequency domain" module of COMSOL [29] using the Drude-Lorentz dielectric function (3.12) and parameters found in the previous chapter for sample 11 and its substrate together with the periodic boundary conditions in direction of the periods. The minimum and maximum mesh element sizes in the simulations are set to 30 nm and 1 μm respectively. The simulated electric field norm for $\theta_{in} = 32°$ is shown in the inset of Fig. 4.7. Simulation and experimental results are compared in section 4.3.3.

4.3.2. Fabrication of the grating

Sample 11 (see Chapter 3) with a 3 μm thick highly doped InP:Si epilayer ($N=2.7\times10^{19}$ cm^{-3}) on top of low doped InP:S substrate ($N=1.5\times10^{18}$ cm^{-3}) is used to fabricate a diffraction grating with a period of 50 μm and duty cycle of 50%. In this regard a SiO_2 layer with a thickness of 187 nm is deposited on top of the sample using plasma-enhanced chemical vapor deposition (PECVD) [Fig. 4.6(b)]. The exact thickness of the glass layer is measured by ellipsometry. Afterwards the sample is prebaked at 120 °C on a hot plate for 30 minutes in order to remove the moisture. To increase the adhesion between the sample and the photoresist, which will be spin-coated in the next step, AP3000 adhesion promoter is spin-coated on the sample and baked at 160 °C for one minute. Afterwards 1.4 μm of the negative photoresist nLOF2020 is spin-coated on the sample and baked at 110 °C for one minute [Fig. 4.6(c)]. The sample with the photoresist on top is exposed to UV light with the wavelength 365 nm for 11 seconds through a chromium mask with the grating pattern. The exposure is done using the "hard contact" program of the mask aligner, followed by a post-exposure bake at 110 °C for 1 minute. Afterwards the sample is immersed in AZ726MIF developer for 50

seconds in order to dissolve the unexposed parts of the photoresist followed by 75 seconds plasma exposure in plasma asher machine with 40% power in order to remove any polymer contamination from surface of the sample [Fig. 4.6(d)]. In this step surface profile of the sample is measured by Dektak 8 stylus profiler in order to make sure that the depth of the developed photoresist is 1.4 µm and all of the unexposed parts of the resist are removed. After post-baking the sample at 110 °C for 2 minutes, III-V reactive ion etching (RIE) machine is used to dry-etch parts of the glass layer with no photoresist on top [Fig. 4.6(e)]. According to the selected program for etching SiO_2, 4 minutes of etching is enough to etch 187 nm of glass. Afterwards the remaining photoresist is removed by immersing the sample in a 70 °C 5% KOH solution for 5 minutes. Sample is cleaned in the plasma asher machine for 90 seconds with 100% power and afterwards 2 µm of the highly doped InP:Si epilayer is dry-etched using 21 etch cycles in the III-V RIE machine [Fig. 4.6(f)]. In this step remaining glass on top of the sample works as a mask for dry etching of InP:Si. Finally the glass mask is removed by immersing the sample in buffered hydrofluoric acid (BHF) for four minutes [Fig. 4.6(g)]. In this way a 1 µm thick highly doped InP:Si layer is kept under the 2 µm high grating in order to support SPPs. The height of the grating is checked by Dektak 8 stylus profiler and scanning electron microscope (SEM). Figure 4.7 shows the SEM image of the fabricated grating structure.

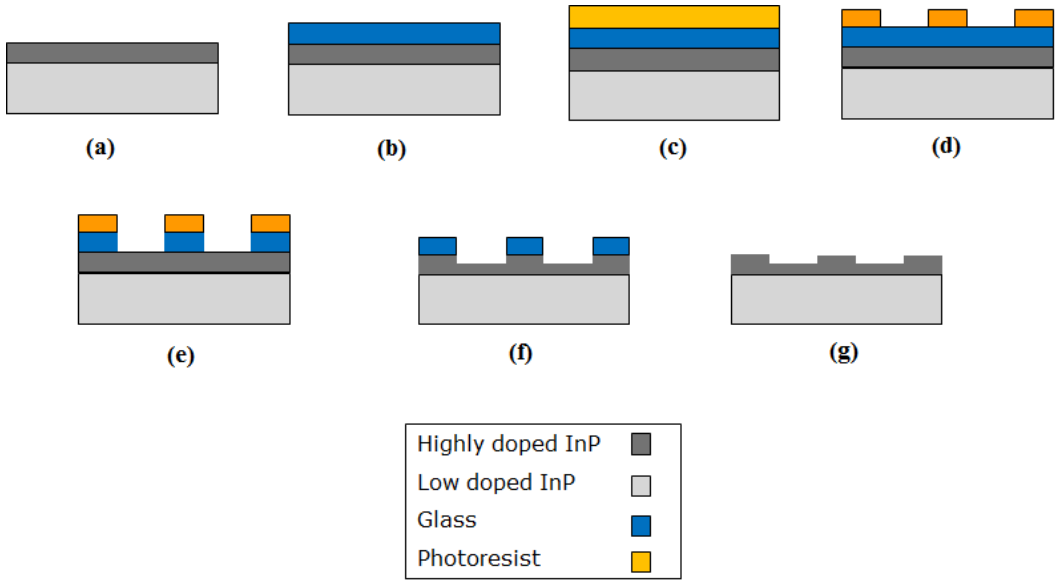

Fig. 4.6 Fabrication steps of the plasmonic grating

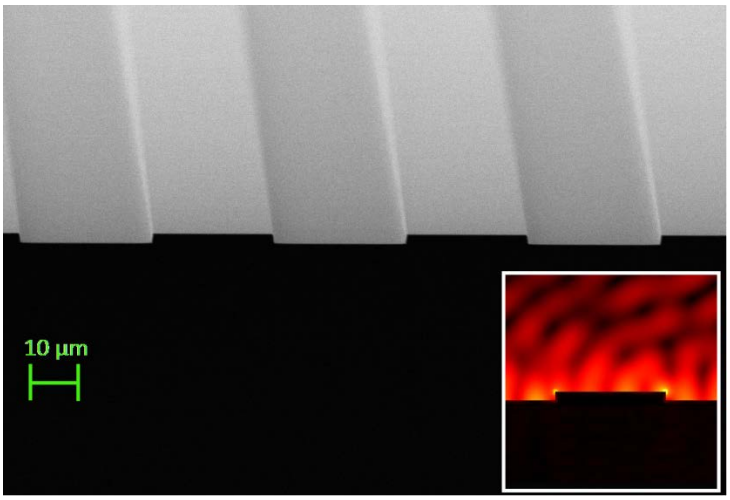

Fig. 4.7 SEM image of the fabricated grating structure, inset: simulated electric field map for $\theta_{in} = 32°$.

4.3.3. Experiment

The FTIR setup with a wire grid polarizer is used to measure TM polarized light reflected from the grating. The reflectance is normalized to the reflectance from plain sample 11, and an aperture with 2 mm diameter is used to constrain the angular variation of the focused incident beam. Measurements are repeated three times and then averaged for each incidence angle in order to suppress the noise. Figure 4.8(a) shows the specular (mode 0) reflectance map where the angle of incidence on the grating is swept from 14° to 46° with an increment of 2°.

The reflectance spectra from the grating are simulated by the finite element method (COMSOL Multiphysics 5.0 [29]) using the Drude-Lorentz dielectric function and parameters found in chapter 3 for sample 11 and its substrate together with periodic boundary conditions in direction of the periods. The simulated reflection spectrum for each incidence angle θ_{in} is actually the averaged reflection spectra from $\theta_{in} - 1.75°$ to $\theta_{in} + 1.75°$ with increments of 0.25° in order to imitate the angle uncertainty in the FTIR setup. As it is shown in Fig. 4.8, the results exhibit good agreement between the simulations and the experiment. The dip starting from around 13 µm at $\theta_{in} = 14°$ and continuing up to around 17.5 µm at $\theta_{in} = 46°$ shows the SPP coupling corresponding to $n = 5$ [(Eq. (4.24)] which is anti-crossed by SPP coupling dips corresponding to $n = 3$, $n = 2$ and $n = 1$ at 13 µm, 15 µm and 17 µm respectively (Fig. 4.5). The dip starting from around 11 µm at $\theta_{in} = 14°$ and continuing up to around 13 µm at $\theta_{in} = 46°$ shows the SPP coupling corresponding to $n = 6$ [Eq. (4.24)] which is anti-crossed by SPP coupling dips corresponding to $n = 3$ and $n = 2$ at 11.5 µm and 12 µm respectively (Fig. 4.5). SPP coupling dips which happen at lower wavelengths are less pronounced due to the fact that the real part of the permittivity has less contrast with the permittivity of air on these wavelengths.

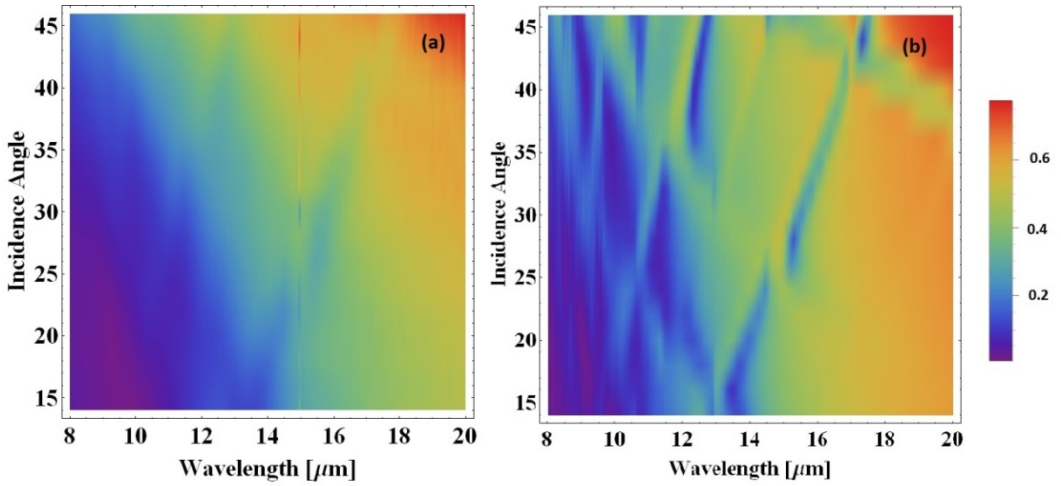

Fig. 4.8 (a) Experimental and (b) simulated reflectance map from the grating

Figure 4.9(a) shows the simulated and measured specular reflectance spectra for the angle of incidence $\theta_{in} = 32°$. According to Eq. (4.24), at this angle, light couples to SPPs at $\lambda = 15.45$ μm for $n = 5$ and according to Eq. (4.26), when the incident light couples to the SPP, the previously vanishing mode $m - n = -2$ emerges as a reflected beam with $\theta_{out} = 5°$. Figure 4.9(b) shows the simulated and measured reflected light at the output angle of 5°, apparently as mode -2. The slight deviation between the SPP coupling wavelength predicted by Eq. (4.24) and observed in the simulation and experiment is believed to be mainly due to the uncertainties in the FTIR setup as explained in section 4.2.2, namely inherent noise of the system, angular uncertainty and polarization conversion. These uncertainties which are an inseparable part of FTIR diffraction experiments tend to diminish the SPP coupling features in the reflection spectra from the grating as was observed before [28]. This also explains visible deviations in the resonances parameters in simulations and characterization in Figs. 4.9(a) and 4.9(b). The sharp peak observed at around 15 μm, also visible as a vertical line in Fig. 4.8(a) for all angles is attributed to the measurement system's noise and thus should be ignored.

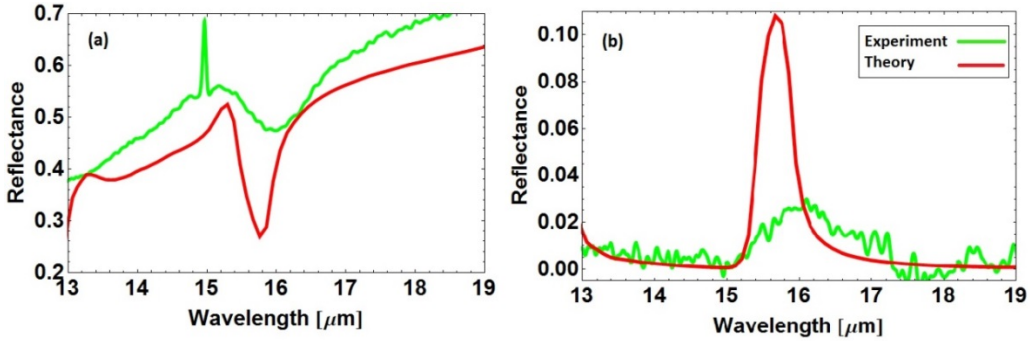

Fig. 4.9 (a) Mode 0 reflection from the grating. $\theta_{in} = -\theta_{out} = 32°$ (b) mode -2 reflection from the grating. $\theta_{in} = 32°$ and $\theta_{out} = 5°$.

4.4. Summary

In this chapter we first solved Maxwell equations in order to find solutions in form of a surface wave which propagates at the interface between a dielectric and a conductive material. It was shown that these surface waves which are confined to the interface, and are called surface plasmon polaritons, only exist for TM polarization and cannot be directly excited by free-space light. Drude-Lorentz dielectric function with the parameters found in chapter 3 for InP:Si was used to simulate excitation of SPPs by both prism coupling and grating coupling techniques. Using a Ge hemispherical prism, we experimentally confirmed existence of mid-IR SPPs at highly doped InP:Si/air and highly doped InP:Si/low doped InP:S interfaces. Measured SPPs dispersion is in a good agreement with simulations. We fabricated an InP:Si grating and characterized diffraction of light in different orders. Appearance of the orders prohibited by the conventional Bragg law manifests the efficient SPPs assistance in light diffraction on plasmonic gratings.

Good agreement between the experiments and the simulations confirms the validity of our fitting method to determine the permittivity of the plasmonic layer and demonstrates that highly doped InP is an effective plasmonics material for the mid-infrared region.

References

1. U. Fano, “The theory of anomalous diffraction gratings and of quasi-stationary waves on metallic surfaces (Sommerfeld’s waves),” J. Opt. Soc. Am. **31**(3), 213-222 (1941).
2. S. A. Maier, Plasmonics: Fundamentals and Applications (Springer, 2007).
3. T. W. Ebbesen, H. J. Lezec, H. F. Ghaemi, T. Thio, and P. A. Wolff, “Extraordinary optical transmission through sub-wavelength hole arrays,” Nature **391**, 667-669 (1998).
4. J. A. Dionne, L. A. Sweatlock, H. A. Atwater, and A. Polman, “Planar metal plasmon waveguides: frequency-dependent dispersion, propagation, localization, and loss beyond the free electron model,” Phys. Rev. B **72**(7), 075405 (2005).
5. D. J. Bergman, and M. I. Stockman, “Surface plasmon amplification by stimulated emission of radiation: quantum generation of coherent surface plasmons in nanosystems,” Phys. Rev. Lett. **90**(2), 027402 (2003).
6. H. A. Atwater and A. Polman, “Plasmonics for improved photovoltaic devices,” Nat. Mater. **9**(3), 205–213 (2010).
7. J. B. Pendry, “Negative refraction makes a perfect lens,” Phys. Rev. Lett. **85**(18), 3966 (2000).
8. R. Ma, S. Ota, Y. Li, S. Yang, and X. Zhang, “Explosives detection in a lasing plasmon nanocavity,” Nat. Nanotech. **9**, 600–604 (2014).

9. S. Law, V. Podolskiy, and D. Wasserman, “Towards nano-scale photonics with micro-scale photons: The opportunities and challenges of mid-infrared plasmonics,” Nanophotonics **2**(2), 103-130 (2013).
10. A. Boltasseva, “Empowering plasmonics and metamaterials technology with new material platforms,” MRS Bull. **39**(5), 461-468 (2014).
11. Y. Zhong, S. D. Malagari, T. Hamilton, and D. Wasserman, “Review of mid-infrared plasmonic materials,” J. Nanophotonics **9**(1), 093791 (2015).
12. E. Sachet, C. T. Shelton, J. S. Harris, B. E. Gaddy, D. L. Irving, S. Curtarolo, B. F. Donovan, P. E. Hopkins, P. A. Sharma, A. L. Sharma, J. Ihlefeld, S. Franzen, and J. Maria, “Dysprosium-doped cadmium oxide as a gateway material for mid-infrared plasmonics,” Nat. Mater. **14**(4), 414-420 (2015).
13. P. Biagioni, J. Frigerio, A. Samarelli, K. Gallacher, L. Baldassarre, E. Sakat, E. Calandrini, R. W. Millar, V. Giliberti, G. Isella, D. J. Paul, and M. Ortolanie, “Group-IV midinfrared plasmonics,” J. Nanophotonics **9**(1), 093789 (2015).
14. P. R. West, S. Ishii, G. V. Naik, N. K. Emani, V. M. Shalaev, and A. Boltasseva, “Searching for better plasmonic materials,” Laser Photon. Rev. **4**(6), 795-808 (2010).
15. K. Anglin, T. Ribaudo, D. C. Adams, X. Qian, W. D. Goodhue, S. Dooley, E. A. Shaner, and D. Wasserman, “Voltage-controlled active mid-infrared plasmonic devices,” J. Appl. Phys. **109**(12), 123103 (2011).
16. M. Shahzad, G. Medhi, R. E. Peale, W. R. Buchwald, J. W. Cleary, R. Soref, G. D. Boreman, and O. Edwards, “Infrared surface plasmons on heavily doped silicon,” J. Appl. Phys. **110**(12), 123105 (2011).
17. J. C. Ginn, R. L. Jarecki Jr., E. A. Shaner, and P. S. Davids, “Infrared plasmons on heavily-doped silicon,” J. Appl. Phys. **110**(4), 043110 (2011).
18. W. Streyer, S. Law, G. Rooney, T. Jacobs, and D. Wasserman, “Strong absorption and selective emission from engineered metals with dielectric coatings,” Opt. Express **21**(7), 9113-9122 (2013).
19. S. Law, L. Yu, A. Rosenberg, and D. Wasserman, “All-semiconductor plasmonic nanoantennas for infrared sensing,” Nano Lett. **13**(9), 4569–4574 (2013).
20. Y. Zhong, P. B. Dongmo, L. Gong, S. Law, B. Chase, D. Wasserman, and J. M. O. Zide, “Degenerately doped InGaBiAs:Si as a highly conductive and transparent contact material in the infrared range,” Opt. Mater. Express **3**(8), 1197-1204 (2013).
21. V. N'Tsame Guilengui, L. Cerutti, J. B. Rodriguez, E. Tournié, and T. Taliercio, “Localized surface plasmon resonances in highly doped semiconductors nanostructures,” Appl. Phys. Lett. **101**(16), 161113 (2012).
22. A. Otto, “Excitation of nonradiative surface plasma waves in silver by the method of frustrated total reflection,” Z. Physik **216**, 398–410 (1968).
23. E. Kretschmann, and H. Raether, “Radiative decay of non-radiative surface plasmons excited by light,” Z. Naturforschung **23A**, 2135–2136 (1968).
24. I. J. Hodgkinson, S. Kassam, and Q. H. Wu, “Eigenequations and Compact Algorithms for Bulk and Layered Anisotropic Optical Media: Reflection and Refraction at a Crystal-Crystal Interface,” J. Comput. Phys. **133**(1), 75-83 (1997).

25. M. Sánchez-López, I. Moreno and A. Martínez-García, “Teaching diffraction gratings by means of a phasor analysis,” in *Proceedings of Education and Training in Optics and Photonics* (2009), pp. 1-12.
26. I. Epstein, I. Dolev, D. Bar-Lev, and A. Arie, “Plasmon-enhanced Bragg diffraction,” Phys. Rev. B **86**(20), 205122 (2012).
27. I. Avrutsky, C. W. Smith, J. W. Cleary, and J. R. Hendrickson, “Resonant diffraction into symmetry-prohibited orders of metal gratings,” IEEE J. Quant. Electr. **51**(12), 6600209 (2015).
28. A. S. Kuznetsov, P. Schäfer, W. John, D. Prasai, S. Sadofev, and S. Kalusniak, “Enabling novel functionality in heavily doped ZnO:Ga by nanostructuring: an efficient plasmonic refractive index sensor,” Nanotechnology **27**(2), 02LT02 (2016).
29. COMSOL Multiphysics® v. 5.0. www.comsol.com. COMSOL AB, Stockholm, Sweden.

5. OPTICAL FORCES IN InP-BASED WAVEGUIDES

5.1. Introduction to optomechanics

Microelectromechanical systems (MEMS) are microscopic devices with moving parts which deflect or vibrate upon applying a force. They have been studied and utilized during the last three decades for commercial applications such as controlling fluid jets in inkjet printers, acceleration sensors for deploying car airbags [1], fine-pointing mirrors for intersatellite optical links [2] and tunable vertical-cavity surface-emitting lasers (VCSELs) [3]. Among various MEMS devices, cantilever sensors have attracted considerable attention due to their applications in ultra-sensitive mass sensing [4, 5] and label-free detection of biological molecules [6]. Adsorption of molecules on the surface of a deformable micro-cantilever beam will change its mass and stiffness and consequently its mechanical resonance frequency. Selective detection of different molecules can be realized by functionalizing the surface of the cantilever with specific receptors. MEMS systems are evolving with improvements in fabrication processes in order to shrink the size and reduce the mass and increase the resonance frequency. Most of the currently available MEMS devices are actuated by electrostatic forces, piezoelectric elements or bilayers of different thermal expansions. The induced motion in micro-cantilevers is usually detected by optical interference or deflection of a laser beam reflected from their surface [1].

Well-developed microfabrication techniques for silicon have made it the key material for making MEMS devices, while other materials such as InP can potentially be useful for MEMS technology due to their special properties. In this chapter we investigate the optically induced forces in an InP waveguide which lies above an InP:Si substrate in different frequency ranges, namely the epsilon-near-zero (ENZ) regime, the

surface plasmon polariton (SPP) resonance regime, and the phonon resonance regime. It is shown that the induced attractive forces can be drastically increased upon coupling to the surface plasmons or phonons. The working wavelength range for the ENZ regime and SPP coupling regime can be effectively tuned by changing the carrier concentration of InP (Chapter 3). Deflection of the waveguide can be determined by measuring the phase change of the light when travelling through the deflected waveguide [7]. Simultaneous on-chip optical actuation and detection paves the way towards miniaturization and integration of cantilever sensing devices, which are of great interest for industrial applications.

Light-induced forces were first mentioned by Johannes Kepler in 1619 when he explained the observation that the tail of a comet always points away from the sun.

In his famous paper, published in 1862, James Clerk Maxwell mentioned that electromagnetic radiation can exert pressure upon any surface that it is exerted upon [8]. If the wave is completely absorbed by the surface, the pressure will be equal to

$$P = \frac{\langle \boldsymbol{S} \rangle}{c} = \frac{E_f}{c} \tag{5.1}$$

where $\boldsymbol{S}$ is the Poynting vector which denotes the electromagnetic energy flux density, c is the speed of light and E_f is the energy flux.

If the wave is perfectly reflected from the surface, the pressure will be given by

$$P = \frac{2\,E_f}{c}\cos^2\alpha \tag{5.2}$$

in which α is the angle of incidence.

This phenomenon can also be explained by the quantum theory of light, according to which, each photon carries a momentum equal to $\hbar\omega/c$ that can be transferred to an object when it is hit by the photon.

In 1967 Braginskii and Manukin published a paper and claimed that the radiation force exerted on a mechanical body when it is absorbing or reflecting the light, can be amplified in a Fabry-Perot cavity when the mechanical body serves as one of the mirrors of the cavity [9]. According to their formulation, the radiation pressure of light on a highly absorbing body depends on the velocity of its motion with respect to the light source:

$$F_{em} = \frac{W}{c}\left(1 + \frac{v}{c}\right) = \frac{W}{c} + \frac{Wv}{c^2} \tag{5.3}$$

where F_{em} is the electromagnetc force, W is the power incident on the stationary body and v is the velocity of the body relative to the source and in the radiation direction.

$\Delta F_{em} = Wv/c^2$, therefore the radiation pressure acts as an additional mechanical damping force on the body with the damping constant equal to:

$$H_{em} = \frac{W}{c^2}. \tag{5.4}$$

If the body is perfectly reflecting, H_{em} will be twice as large.

To explain the physics behind this phenomenon, let us imagine that a perfectly reflecting plate on which the power $W_0 = N\hbar\omega_0$ is incident, vibrates in the direction of source with velocity *v* in a half cycle of the vibration. Then the frequency of the reflected photons during this half cycle will be modified as

$$\omega = \omega_0(1 + v/c)(1 - v/c)^{-1} \tag{5.5}$$

Consequently, the power of the light reflected from the plate, averaged over a cycle (considering that $v \ll c$) will be

$$\begin{aligned} W_{ref} &= \frac{1}{2}[N\hbar\omega_0(1 + v/c)(1 - v/c)^{-1} + N\hbar\omega_0(1 - v/c)(1 + v/c)^{-1}] \\ &\cong W_0 + \frac{2W_0v^2}{c^2}. \end{aligned} \tag{5.6}$$

The additional power $\frac{2W_0v^2}{c^2}$ is actually taken from the vibrating mechanical body.

In case of a Fabry-Perot optical resonator with quality factor equal to

$$Q \cong 2\pi l/f\lambda \tag{5.7}$$

where *l* is the length of the cavity, λ is the wavelength and (1-*f*) is the reflection coefficient, the radiation pressure exerted on the mirrors is given by

$$F_{mir} = 2W/f \tag{5.8}$$

in which *W* is the power fed to the resonator. If *Q* is high enough, F_{mir} changes when one of the mirrors is displaced. Therefore the presence of the electric field in the cavity acts like an additional stiffness, which can be negative or positive, to the mechanical stiffness of the moving mirror. The maximum value of this additional stiffness is given by [9]

$$(K_{em})_{max} = Max\left[\frac{\partial F_{mir}}{\partial l}\right] \cong \pm\frac{4\pi W}{cf^2\lambda}. \tag{5.9}$$

The important point is that when the mirror moves, the light pressure changes with a delay equal to $\tau = l/cf$. Consequently K_{em} will also change with the same delay. This time dependent change in the stiffness is equivalent to a damping force given by [9]

$$(H_{em})_{max} = \pm(K_{em})_{max}\,\tau = \pm\frac{W}{c^2}\frac{4\pi l}{f^3\lambda}. \tag{5.10}$$

Therefore in an optical cavity, the damping force if magnified with a factor of $\frac{4\pi l}{f^3\lambda}$ in comparison to a single mirror exposed to radiation pressure.

5.2. Waveguide optomechanics

During the past decade optical forces which arise due to the coupling between the evanescent tail of a guided wave in a waveguide and a substrate or another waveguide have become an interesting subject of research. In 2005 Povinelli *et al.* theoretically investigated the evanescent wave-bonding between dielectric optical waveguides. They reported forces with piconewtons orders of magnitude which are enough to make a deflection around 20 nm in a 30 μm long beam [10]. Afterwards a series of papers were published which experimentally proved this concept. Li *et al.* in 2008 detected the displacement in a silicon waveguide above a SiO_2 substrate due to the optical forces. They used the phase shift of the light when it passes through a deflected waveguide to detect the deflection [7]. The same group in 2009 published a paper in which they investigated the deflection induced in two evanescently coupled micro-cantilevers [11]. They used the change in the transmission through the waveguide system upon deflection of the cantilevers for detecting the deflection.

In order to find the optically induced forces between a waveguide and an adjacent substrate, the first step is to solve the Maxwell equations and determine the electric and magnetic fields around and inside the waveguide and the substrate.

5.2.1. Slab waveguide

Figure 5.1 shows a slab waveguide with refractive index n_2 inside a cladding material with refractive index n_1. The Maxwell curl equations read

$$\nabla \times \mathbf{E} = -\frac{\partial \mathbf{B}}{\partial t} \tag{5.11a}$$

$$\nabla \times \mathbf{H} = \mathbf{J}_{ext} + \frac{\partial \mathbf{D}}{\partial t} \tag{5.11b}$$

in which **E**, **B**, **H**, $\mathbf{J}_{ext}$ and **D** are the electric field, magnetic flux density, magnetic field, external current density and the dielectric displacement field respectively.

The constitutive equations read

$$\mathbf{D} = \varepsilon_0 \varepsilon \mathbf{E} \tag{5.12a}$$

$$\mathbf{B} = \mu_0 \mu \mathbf{H} \tag{5.12b}$$

in which ε_0 and μ_0 are the permittivity and the permeability of vacuum, and ε and μ are the relative permittivity and permeability of the material respectively.

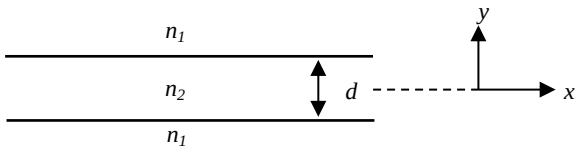

Fig. 5.1 Slab waveguide

Regarding that in the absence of any external current $\mathbf{J}_{ext} = 0$, and for a non-magnetic medium $\mu = 1$, considering a harmonic time dependence in form of $e^{i\omega t}$ for the fields, expanding the Eqs. (5.11) yields

$$\begin{aligned}
\left(\frac{\partial E_z}{\partial y} - \frac{\partial E_y}{\partial z}\right) &= -\mu_0 i\omega H_x \\
\left(\frac{\partial E_x}{\partial z} - \frac{\partial E_z}{\partial x}\right) &= -\mu_0 i\omega H_y \\
\left(\frac{\partial E_y}{\partial x} - \frac{\partial E_x}{\partial y}\right) &= -\mu_0 i\omega H_z \\
\left(\frac{\partial H_z}{\partial y} - \frac{\partial H_y}{\partial z}\right) &= \varepsilon_0 \varepsilon i\omega E_x \\
\left(\frac{\partial H_x}{\partial z} - \frac{\partial H_z}{\partial x}\right) &= \varepsilon_0 \varepsilon i\omega E_y \\
\left(\frac{\partial H_y}{\partial x} - \frac{\partial H_x}{\partial y}\right) &= \varepsilon_0 \varepsilon i\omega E_z \,.
\end{aligned} \tag{5.13}$$

Since the waveguide is infinitely extended along the *x* direction $\frac{\partial}{\partial x} = 0$, and for a propagating wave along the *z* direction $\frac{\partial}{\partial z} = -i\beta$, where β is the wavenumber. Therefore the electric and magnetic fields are given by

$$\begin{aligned}
\mathbf{E}(\mathbf{r}, t) &= \mathbf{E}(y) e^{i(\omega t - \beta z)} \\
\mathbf{H}(\mathbf{r}, t) &= \mathbf{H}(y) e^{i(\omega t - \beta z)} \,.
\end{aligned} \tag{5.14}$$

Using Eqs. (5.14), Eqs. (5.13) read

$$\begin{aligned}
\frac{\partial E_z}{\partial y} + i\beta E_y &= -\mu_0 i\omega H_x \\
i\beta E_x &= \mu_0 i\omega H_y \\
\frac{\partial E_x}{\partial y} &= \mu_0 i\omega H_z \\
\frac{\partial H_z}{\partial y} + i\beta H_y &= \varepsilon_0 \varepsilon i\omega E_x \\
i\beta H_x &= -\varepsilon_0 \varepsilon i\omega E_y \\
\frac{\partial H_x}{\partial y} &= -\varepsilon_0 \varepsilon i\omega E_z \,.
\end{aligned} \tag{5.15}$$

For TE polarization, the electric field is in the *x* direction and the magnetic field has both *y* and *z* components. Therefore

$$E_y = E_z = H_x = 0 \qquad \text{(For TE polarization)}, \tag{5.16}$$

and Eqs. (5.15) reduce to

$$\begin{aligned} E_x &= \frac{\mu_0 \omega}{\beta} H_y \\ \frac{\partial E_x}{\partial y} &= \mu_0 i\omega H_z \\ \frac{\partial H_z}{\partial y} + i\beta H_y &= \varepsilon\varepsilon_0 i\omega E_x \end{aligned} \tag{5.17}$$

Substituting the first two equations of (5.17) in the third one and using the relation $c^2 = \frac{1}{\mu_0 \varepsilon_0}$, where *c* is the speed of light, one will get to the wave equation [12]

$$\frac{\partial^2 E_x}{\partial y^2} + (k_0^2 n_i^2 - \beta^2) E_x = 0 \tag{5.18}$$

in which $k_0 = \frac{\omega}{c}$ is the wavenumber of light in vacuum.

Inside the waveguide, we seek for standing waves in the *y* direction which propagate along the *z* direction:

$$E_x(y) = Ae^{ik_c y} + Be^{-ik_c y} = A\sin(k_c y) + B\cos(k_c y) \tag{5.19}$$

where k_c is the wavenumber inside the waveguide (core), given by

$$k_c = \sqrt{k_0^2 n_2^2 - \beta^2}\,. \tag{5.20}$$

Defining the effective mode index n_{eff} as

$$\beta = k_0 n_{eff}\,, \tag{5.21}$$

knowing that $n_1 < n_{eff} < n_2$, regarding that we are looking for evanescent wave solutions in the *y* direction outside the core

$$E_x(y) = Ce^{-k_a y} \tag{5.22}$$

where k_a, the wavenumber outside the waveguide, is real and positive and defined as

$$k_a = \sqrt{\beta^2 - k_0^2 n_1^2}\,. \tag{5.23}$$

Therefore, the solution of the wave equation for the electric field takes the form

$$E_x(y) = \begin{cases} A\sin(k_c y) + B\cos(k_c y) & |y| < d/2 \\ Ce^{-k_a y} & y > d/2 \\ De^{k_a y} & y < -d/2 \end{cases} \tag{5.24}$$

The unknowns in Eqs. (5.24) are *A*, *B*, *C*, *D*, k_c and k_a. The complete form of solutions for the electric and the magnetic fields will be

$$E_x(\mathbf{r}) = \begin{cases} (A\sin(k_c y) + B\cos(k_c y))e^{-i\beta z} & |y| < d/2 \\ Ce^{(-k_a y - i\beta z)} & y > d/2 \\ De^{(k_a y - i\beta z)} & y < -d/2 \end{cases} \tag{5.25}$$

$$H_z(\mathbf{r}) = \frac{-i}{\mu_0 \omega}\frac{\partial E_x(\mathbf{r})}{\partial y}$$

In order to find the unknowns, we use the continuity of the tangential components of the electric and the magnetic fields across the interfaces as the boundary conditions. For E_x

$$\begin{aligned} @\ y = d/2: &\quad A\sin(k_c\, d/2) + B\cos(k_c\, d/2) = Ce^{(-k_a\, d/2)} \\ @\ y = -d/2: &\quad -A\sin(k_c\, d/2) + B\cos(k_c\, d/2) = De^{(-k_a\, d/2)} \end{aligned} \tag{5.26}$$

For H_z

$$\begin{aligned} @\ y = d/2: &\quad k_c A\cos(k_c\, d/2) - k_c B\sin(k_c\, d/2) = -k_a Ce^{(-k_a\, d/2)} \\ @\ y = -d/2: &\quad k_c A\cos(k_c\, d/2) + k_c B\sin(k_c\, d/2) = k_a De^{(-k_a\, d/2)} \end{aligned} \tag{5.27}$$

Rearranging the above equations yield

$$\begin{aligned} 2A\sin(k_c\, d/2) &= (C - D)e^{(-k_a\, d/2)} \\ 2k_c A\cos(k_c\, d/2) &= k_a(D - C)e^{(-k_a\, d/2)} \\ 2B\cos(k_c\, d/2) &= (D + C)e^{(-k_a\, d/2)} \\ 2k_c B\sin(k_c\, d/2) &= k_a(C + D)e^{(-k_a\, d/2)} \end{aligned} \tag{5.28}$$

Solutions of the above equations can be grouped into two types: symmetric solutions in which $C = D$ and $A = 0$, and anti-symmetric solutions in which $C = -D$ and $B = 0$. For symmetric solutions, the boundary condition equations (5.28) yield

$$k_c \tan\left(\frac{1}{2}k_c d\right) = k_a\,. \tag{5.29}$$

For anti-symmetric solutions

$$k_c \cot\left(\frac{1}{2}k_c d\right) = -k_a\,. \tag{5.30}$$

k_c and k_a are both related to β, therefore the unknowns are *C*, β and *A* or *B*. *A* (or *B*), and *C* are indeed amplitudes of the modes and will be denoted by E_0 and E_1. Combining the solutions for symmetric and anti-symmetric modes, Eqs. (5.25) read

$$E_x(y) = \begin{cases} E_1 e^{-k_a y}e^{-i\beta z} & y > d/2 \\ E_0 \begin{Bmatrix} \sin k_c y \\ \cos k_c y \end{Bmatrix} e^{-i\beta z} & |y| \le d/2 \\ \begin{Bmatrix} - \\ + \end{Bmatrix} E_1 e^{k_a y}e^{-i\beta z} & y < -d/2 \end{cases} \quad \begin{Bmatrix} \text{For} \\ \text{Anti} - \text{symmetric} \\ \text{Symmetric} \end{Bmatrix} \tag{5.31}$$

Solving the boundary condition at $y = d/2$ for E_1 yields

$$E_1 e^{-k_a\, d/2} = E_0 \begin{Bmatrix} \sin(k_c\, d/2) \\ \cos(k_c\, d/2) \end{Bmatrix}, \tag{5.32}$$

therefore

$$E_1 = E_0 e^{k_a\, d/2} \begin{Bmatrix} \sin(k_c\, d/2) \\ \cos(k_c\, d/2) \end{Bmatrix} \tag{5.33}$$

Now, the only unknown is β which will be found by solving the two coupled equations:

$$k_c^2 + k_a^2 = k_0^2(n_2^2 - n_1^2) \tag{5.34a}$$

$$k_c \tan\left(\frac{1}{2}k_c d\right) = k_a \text{ or } k_c \cot\left(\frac{1}{2}k_c d\right) = -k_a \tag{5.34b}$$

These equations are transcendental equations and can only be solved numerically [12]. Figure 5.2 graphically shows the solutions of Eqs. (5.34) as the intersections of the circle corresponding to the Eq. (5.34a) and the curves corresponding to Eq. (5.34b), for $\lambda_0 = 1.55$ µm, $d = 1$ µm, $n_1 = 1$ and $n_2 = 3.5$. A particular β and n_{eff} can be found from (5.21) and (5.23), for each solution of Eqs. (5.34).

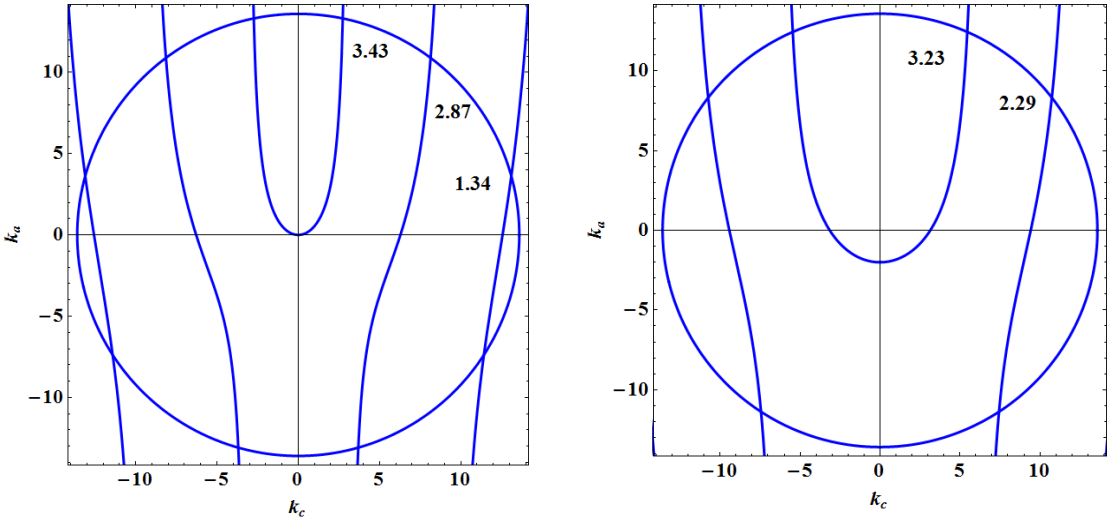

Fig. 5.2 Graphical representation of the solutions of the Eqs. (5.34), for symmetric (left) and anti-symmetric guided modes in a slab waveguide. Values for n_{eff} is shown for each solution.

For TM polarization, the magnetic field is in the *x* direction and the electric field has both *y* and *z* components. Therefore

$$H_y = H_z = E_x = 0 \qquad \text{(For TM polarization)}, \tag{5.35}$$

and Eqs. (5.15) reduce to

$$\begin{aligned} H_x &= \frac{\varepsilon\varepsilon_0\omega}{\beta} E_y \\ \frac{\partial H_x}{\partial y} &= -\varepsilon\varepsilon_0 i\omega E_z \\ \frac{\partial E_z}{\partial y} + i\beta E_y &= -\mu_0 i\omega H_x \end{aligned} \tag{5.36}$$

Therefore, the solution of the wave equation for the magnetic field takes the form

$$H_x(y) = \begin{cases} A\sin(k_c y) + B\cos(k_c y) & |y| < d/2 \\ Ce^{-k_a y} & y > d/2 \\ De^{k_a y} & y < -d/2 \end{cases} \tag{5.37}$$

and the eigen equations become

$$\begin{aligned} k_c \tan\left(\frac{1}{2}k_c d\right) &= \frac{n_2^2}{n_1^2}k_a \\ k_c \cot\left(\frac{1}{2}k_c d\right) &= -\frac{n_2^2}{n_1^2}k_a \,. \end{aligned} \tag{5.38}$$

5.2.2. Slab waveguide near a substrate

When a slab waveguide lies above a substrate, the evanescent tail of the guided modes can couple to the substrate and this will change the effective index of the mode. Figure 5.3 shows a slab waveguide with refractive index n_c, inside a cladding material with refractive index n_a, separated from a substrate with refractive index n_s, where $n_a < n_s < n_c$.

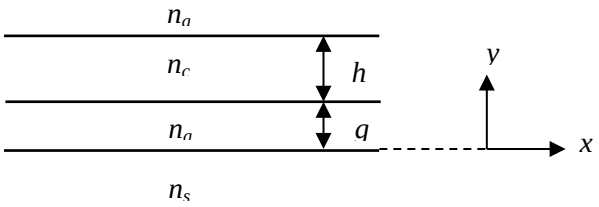

Fig. 5.3 Slab waveguide near a substrate

Starting from Eq. (5.18), for three different material regions we have

$$\begin{aligned} k_s &= \sqrt{\beta^2 - k_0^2 n_s^2} \\ k_a &= \sqrt{\beta^2 - k_0^2 n_a^2} \\ k_c &= \sqrt{k_0^2 n_c^2 - \beta^2}\,. \end{aligned} \tag{5.39}$$

For TE polarization, the electric field takes the form [12]

$$E_x(y) = A\begin{cases} a_1 e^{k_s y} & y < 0 \\ a_2 e^{-k_a y} + a_3 e^{k_a y} & 0 \le y < g \\ \cos(k_c(y-g) + \phi) & g \le y < g + h \\ a_4 e^{-k_a(y-g-h)} & y \ge g + h \end{cases} \tag{5.40}$$

Continuity of E_x and H_z at the boundaries gives

$$
\begin{aligned}
&@\ y = 0 && a_1 = a_2 + a_3 \\
& && a_1 k_s = \frac{k_a}{k_s}(a_3 - a_2) \\
&@\ y = g && a_2 e^{-k_a g} + a_3 e^{k_a g} = \cos\phi \\
& && -k_a a_2 e^{-k_a g} + k_a a_3 e^{k_a g} = -k_c \sin\phi \\
&@\ y = g + h && \cos(k_c h + \phi) = a_4 \\
& && -k_c \sin(k_c h + \phi) = -k_a a_4
\end{aligned}
\tag{5.41}
$$

After some manipulations Eqs. (5.41) yield

$$
\begin{aligned}
a_1 &= 2a_3 \frac{k_a}{k_a + k_s} \\
a_2 &= \frac{a_3(k_a - k_s)}{k_a + k_s} \\
a_4 &= \frac{k_c}{\sqrt{k_a^2 + k_c^2}} \\
\phi &= -\text{Arccot}\left[\frac{k_c(k_a + e^{2gk_a}k_a - k_s + e^{2gk_a}k_s)}{k_a(-k_a + e^{2gk_a}k_a + k_s + e^{2gk_a}k_s)}\right]
\end{aligned}
\tag{5.42}
$$

Substituting ϕ from the last equation of (5.42) in the first boundary condition at $y = g + h$, one can eliminate ϕ and find the transcendental equation as [12]

$$
\begin{aligned}
k_c h = &\ \text{Arctan}\left[\frac{k_a}{k_c}\right] \\
&+ \text{Arctan}\left[\frac{k_a}{k_c}\tanh\left(\text{Arctan}\left[\frac{k_s}{k_a}\right] + g k_a\right)\right] \qquad N = 0,1,2,\ldots \\
&+ N\pi
\end{aligned}
\tag{5.43}
$$

Using the first boundary condition at $y = g$, substituting ϕ from (5.42), and writing a_2 in terms of a_3, one will find the relation for a_3 as

$$
a_3 = \frac{k_a + k_s}{2M} \tag{5.44}
$$

where

$$
M = \sqrt{\left(\frac{k_a}{k_c}\right)^2 [k_a \sinh(k_a g) + k_s \cosh(k_a g)]^2 + [k_s \sinh(k_a g) + k_a \cosh(k_a g)]^2} \tag{5.45}
$$

Figure 5.4 shows n_{eff} as a function of the gap size, calculated using Eq. 5.43, for a 110 nm thick slab waveguide for $\lambda_0 = 1.55$ μm, $n_a = 1$, $n_c = 3.5$, and $n_c = 1.5$. The effective mode index approaches to the value for a free waveguide as the gap size increases. The inset of the Fig. 5.4 shows the electric field map calculated by finite element method (FEM), using COMSOL [13]. A very good agreement between the calculations (dotted line) and the FEM simulation results (solid line) can be observed.

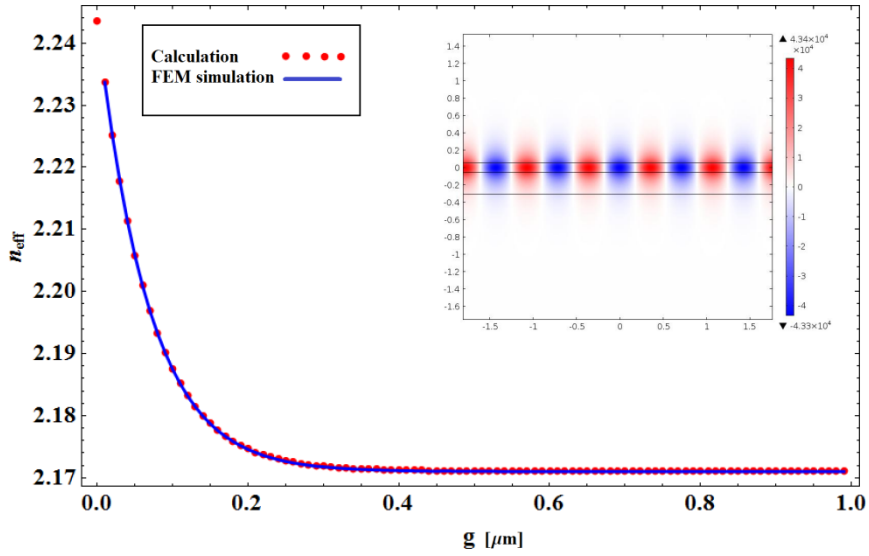

Fig. 5.4 n_{eff} as a function of the gap size for a slab waveguide above a substrate. Inset: FEM simulated electric field map

5.2.3. Waveguide with a rectangular cross section near a substrate

In order to generalize the one dimensional problem of the slab waveguide to the two dimensional problem of a waveguide with a rectangular cross section, one can use approximations such as the *effective index method* [12]. Consider the waveguide in Fig. 5.5(a). The effective mode index of this waveguide can be found by calculating the effective mode index of the slab waveguide in Fig. 5.5(b) n_{eff}^1, and then using it to calculate the effective mode index of the vertical slab waveguide in Fig. 5.5(c). The vertical slab waveguide is equivalent to a horizontal slab waveguide in the opposite polarization.

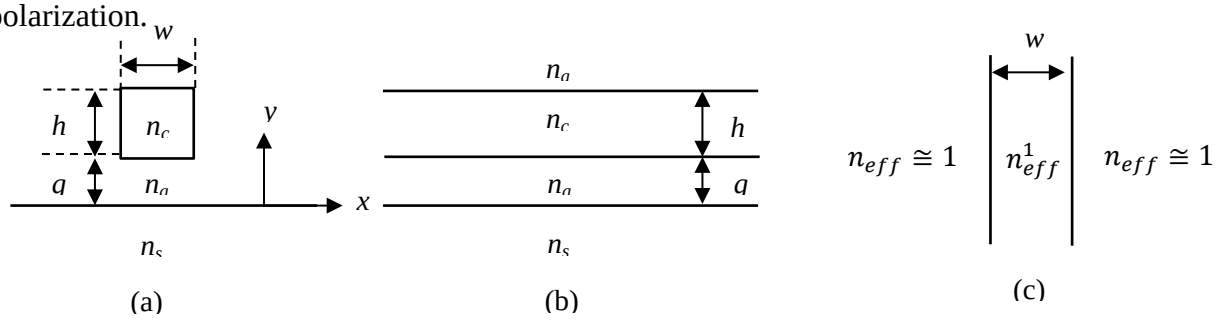

Fig. 5.5 (a) Rectangular cross section waveguide; (b) and (c), its components according to the effective index method.

Figure 5.6 and 5.7 show n_{eff} of a waveguide with a rectangular cross section, corresponding to the first and second symmetric modes respectively, calculated using the effective index method together with the FEM simulation result, for a waveguide with $h = 110$ nm, $w = 2$ μm, $\lambda_0 = 1.55$ μm, $n_a = 1$, $n_c = 3.5$, and $n_s = 1.5$.

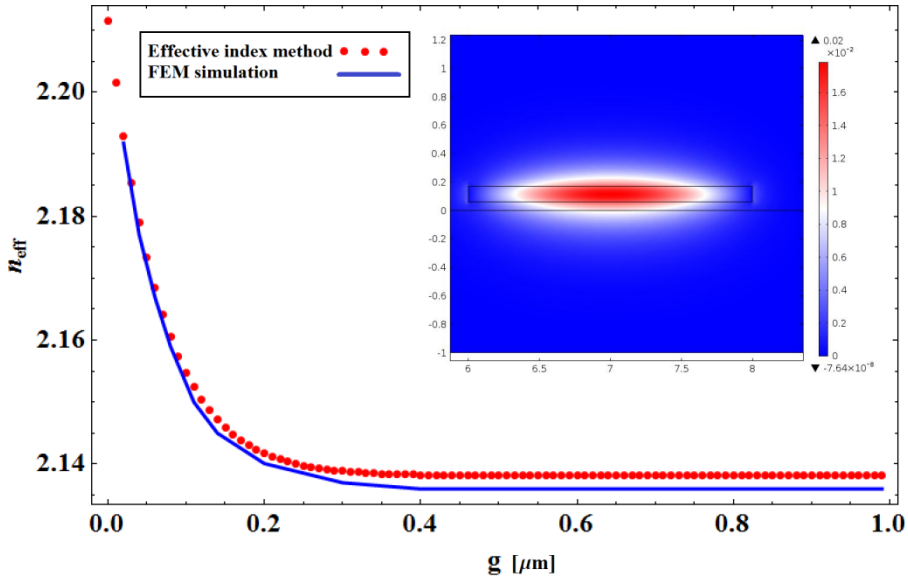

Fig. 5.6 n_{eff} as a function of the gap size for the first symmetric mode of a waveguide with a rectangular cross section above a substrate with $w = 2$ μm. Inset: FEM simulated electric field map

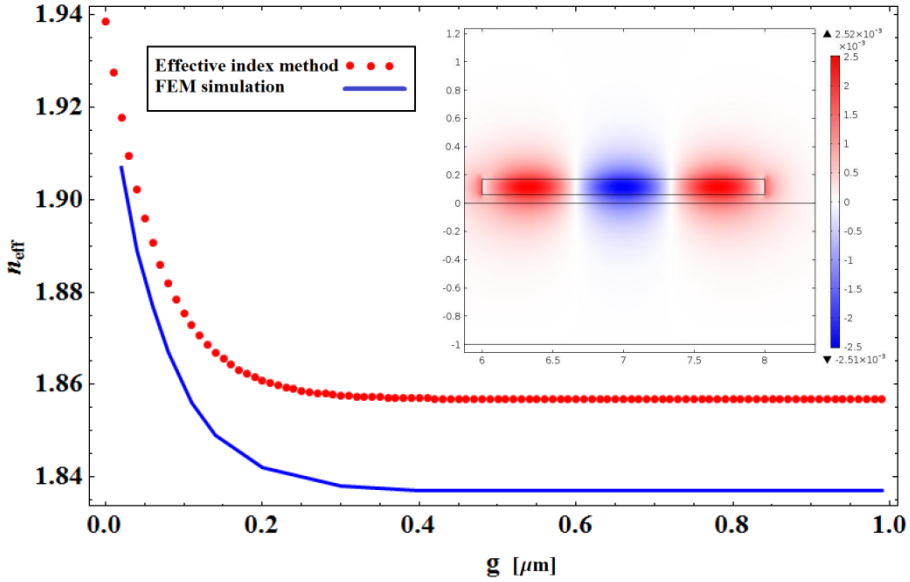

Fig. 5.7 n_{eff} as a function of the gap size for the second symmetric mode of a waveguide with a rectangular cross section above a substrate with $w = 2$ μm. Inset: FEM simulated electric field map

Figure 5.8 shows n_{eff} of the above mentioned waveguide when $w = 0.5$ μm, for the first symmetric mode which becomes the only existing guided mode when w is decreased to 0.5 μm. As the width of the waveguide becomes smaller than the wavelength, the effective index method breaks down, and its results significantly deviate from the FEM simulation results.

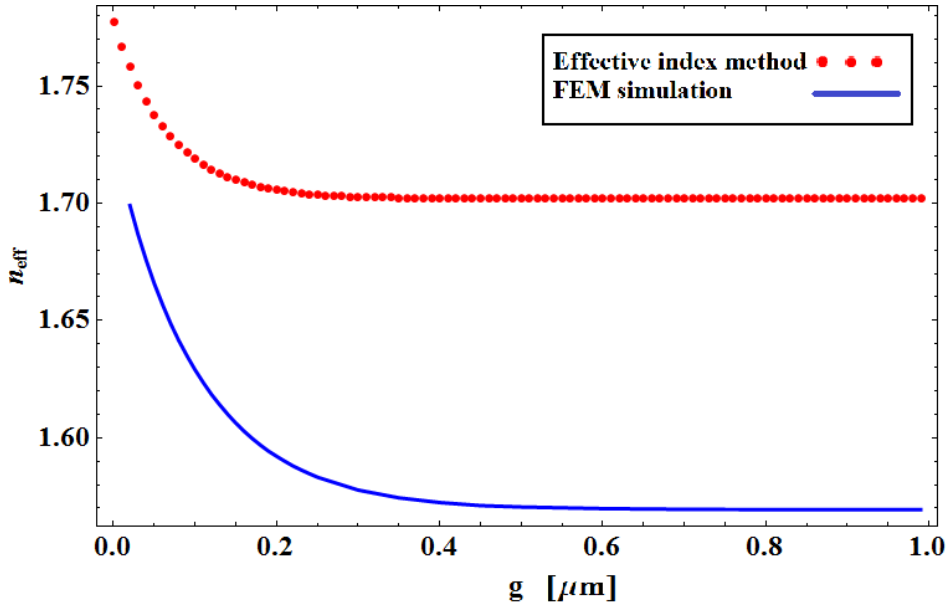

Fig. 5.8 n_{eff} as a function of the gap size for the first symmetric mode of a waveguide with a rectangular cross section above a substrate with $w = 0.5$ μm

5.2.4. Optical forces due to evanescent-wave bonding

Maxwell stress tensor, which is derived by substituting Maxwell equations in the Lorentz force law, can be used to calculate the optically induced forces which arise due to the coupling of the evanescent tail of the guided waves to the substrate.

The Lorentz force law defines the force **F**, that is exerted on a particle with charge q as it moves with velocity **V** in presence of the electric and magnetic fields **E** and **B**:

$$\mathbf{F} = q(\mathbf{E} + \mathbf{V} \times \mathbf{B}) . \tag{5.46}$$

Using the relations for **E** and **B** from Maxwell equations, after some mathematical manipulations [14], the force per unit volume will be found as

$$\mathbf{f} = \varepsilon_0[(\nabla.\mathbf{E})\mathbf{E} + (\mathbf{E}.\nabla)\mathbf{E}] + \frac{1}{\mu_0}[(\nabla.\mathbf{B})\mathbf{B} + (\mathbf{B}.\nabla)\mathbf{B}] - \frac{1}{2}\nabla\left(\varepsilon_0 E^2 + \frac{1}{\mu_0}B^2\right) - \varepsilon_0\frac{\partial}{\partial t}(\mathbf{E} \times \mathbf{B}) \tag{5.47}$$

which can be written in compact form as

$$\sigma_{ij} = \varepsilon_0\left(E_i E_j - \frac{1}{2}\delta_{ij}E^2\right) + \frac{1}{\mu_0}\left(B_i B_j - \frac{1}{2}\delta_{ij}B^2\right) \tag{5.48}$$

where δ_{ij} is the Kronecker delta defined as

$$\delta_{ij} = \begin{cases} 1 & \text{for } i = j \\ 0 & \text{for } i \neq j \end{cases} \tag{5.49}$$

For TE polarization $E_y = E_z = H_x = 0$, and σ_{yy} is found to be

$$\sigma_{yy} = -\frac{\varepsilon_0}{2}\left[|E_x|^2 + c^2\mu_0^2\left(|H_z|^2 - \left|H_y\right|^2\right)\right]. \tag{5.50}$$

Since both the electric and the magnetic fields have time dependence in form of $\cos(\omega t)$, $|E_x|^2$, $|H_z|^2$ and $\left|H_y\right|^2$ have time dependence in form of $\cos^2(\omega t)$. The average of $\cos^2(\omega t)$ over a cycle is $\frac{1}{2}$, therefore the time averaged *yy* component of the stress tensor will be

$$\begin{aligned}\bar{\sigma}_{yy} &= -\frac{\varepsilon_0}{4}\left[|E_x|^2 + c^2\mu_0^2\left(|H_z|^2 - \left|H_y\right|^2\right)\right] \\ &= -\frac{\varepsilon_0}{4}\left[|E_x|^2\left(1 - \frac{\beta^2}{k_0^2}\right) + \frac{1}{k_0^2}\left|\frac{\partial E_x}{\partial y}\right|^2\right].\end{aligned} \tag{5.51}$$

For $y \geq g + h$ (Fig. 5.5)

$$E_x = Aa_4 e^{-k_a(y-g-h)}, \tag{5.52}$$

therefore

$$\bar{\sigma}_{yy} = -\frac{\varepsilon_0}{4}\left[(Aa_4)^2\left(1 - \frac{\beta^2}{k_0^2}\right) + \frac{1}{k_0^2}(Aa_4k_a)^2\right]e^{-2k_a(y-g-h)}. \tag{5.53}$$

Regarding that $k_a^2 = \beta^2 - k_0^2 n_a^2$

$$\begin{aligned}\bar{\sigma}_{yy} &= -\frac{\varepsilon_0}{4}\left[(Aa_4)^2\left(1 - \frac{\beta^2}{k_0^2} + \frac{\beta^2 - k_0^2n_a^2}{k_0^2}\right)\right]e^{-2k_a(y-g-h)} \\ &= -\frac{\varepsilon_0}{4}\left[|E_x|^2(1 - n_a^2)\right].\end{aligned} \tag{5.54}$$

For the waveguide in air $n_a = 1$, hence for $y \geq g + h$, $\bar{\sigma}_{yy} = 0$ which is the result of the evanescent nature of the field above the waveguide [15].

For $0 \leq y \leq g$ (Fig. 5.5)

$$E_x = Aa_2 e^{-k_a y} + Aa_3 e^{k_a y} \tag{5.55}$$

therefore

$$\begin{aligned}\bar{\sigma}_{yy} = -\frac{\varepsilon_0}{4}\Bigg[&A^2(a_2^2e^{-2k_ay} + a_3^2e^{2k_ay} + 2a_2a_3)\left(1 - \frac{\beta^2}{k_0^2}\right) \\ &+ \frac{1}{k_0^2}A^2k_a^2(a_2^2e^{-2k_ay} + a_3^2e^{2k_ay} - 2a_2a_3)\Bigg].\end{aligned} \tag{5.56}$$

Regarding that $(n_a^2 - 1) = 0$ and $(n_a^2 + 1) = 2$ [15]

$$\bar{\sigma}_{yy} = -\frac{\varepsilon_0 A^2}{4M^2}(n_s^2 - n_a^2)(k_0^2 - \beta^2) \tag{5.57}$$

where *M* is given by (5.45).

The force is given by

$$F_i = \int_V f_i dV = \int_V \frac{\partial \sigma_{ij}}{\partial x_j} dV = \int_V (\nabla . \sigma_{ij}) dV \, . \tag{5.58}$$

According to the divergence theorem [16]

$$F_i = \oint_S \sigma_{ij} . \hat{n}_j da \, . \tag{5.59}$$

Therefore the time-averaged force per unit area on the bottom surface of the beam in *y* direction will be equal to [15]

$$\mathcal{F}_y = \bar{\sigma}_{yy} \, . \tag{5.60}$$

According to (5.57), if the field amplitude A has the unit newtons per coulomb ($\frac{N}{C}$), $\mathcal{F}_y$'s unit will be $\frac{N}{m^2}$. Figure 5.9 shows the force exerted upon a waveguide with $h = 110$ nm, $w = 0.5$ µm, $\lambda_0 = 1.55$ µm, $n_a = 1$, $n_c = 3.5$, and $n_s = 1.5$. The result agrees well with Fig. 2(b) of [15]. The resulting negative sign of the force indicates that the force is attractive.

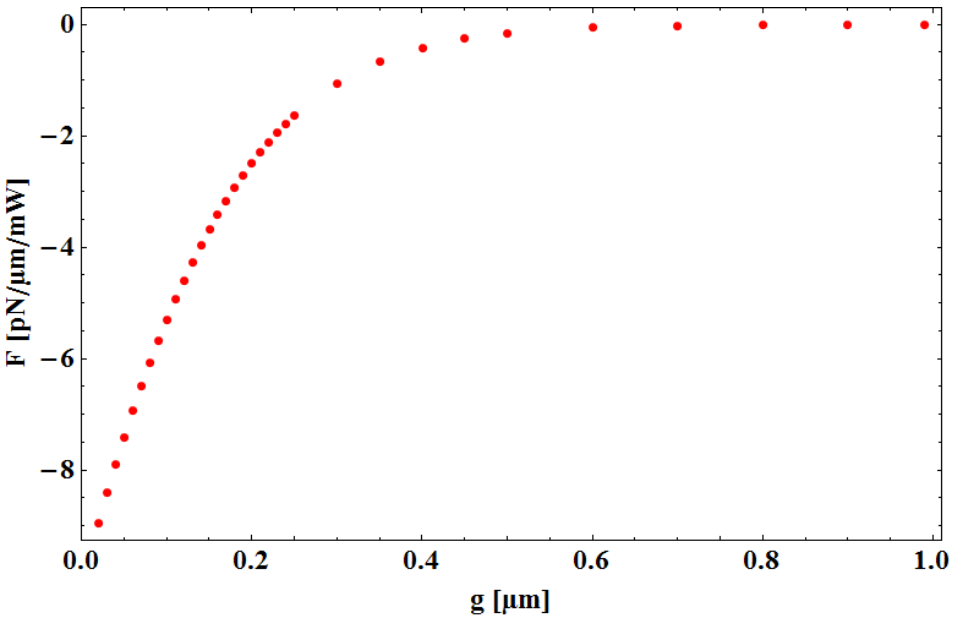

Fig. 5.9 Transverse optical force as a function of the gap size between the waveguide and the substrate

There is another method to calculate the optical force exerted upon a waveguide which is suspended above a substrate, without using the Maxwell stress tensor. Consider the waveguide in Fig. 5.5(a). An adiabatic change in the gap size g will shift the eigen mode frequency of the system by an amount $\Delta\omega$. The total energy conservation implies that the change in the electromagnetic field energy dU is given by

$$dU = -F \, dg \tag{5.61}$$

where

$$U = N\hbar\omega \tag{5.62}$$

in which N is the number of photons and $\hbar$ is the reduced Planck constant.

Therefore

$$F = -\frac{d(N\hbar\omega)}{dg} = -N\hbar\frac{d\omega}{dg} = -\frac{1}{\omega}\frac{d\omega}{dg}U\,. \tag{5.63}$$

The frequency ω is related to the effective mode index of the waveguide by

$$\omega = \frac{\omega_0}{n_{eff}} \tag{5.64}$$

where ω_0 is the frequency of the incoming light.

Therefore [10]

$$F = \frac{1}{n_{eff}}\frac{\partial n_{eff}}{\partial g}U \tag{5.65}$$

where

$$U = PLn_g/c \tag{5.66}$$

in which P is the total optical power, L is the length of the waveguide, c is the speed of light and n_g is the group index defined as

$$n_g = \frac{c}{v_g} = c\frac{\partial k}{\partial\omega} = \frac{\partial}{\partial\omega}\Big(\omega\, n_{eff}(\omega)\Big) = n_{eff}(\omega) + \omega\frac{\partial n_{eff}}{\partial\omega}\,. \tag{5.67}$$

In this way, using FEM, one can find n_{eff} for a range of gap sizes and also for a range of different input wavelengths and calculate $\frac{\partial n_{eff}}{\partial g}$ and $\frac{\partial n_{eff}}{\partial\omega}$ numerically and finally calculate the force.

Figure 5.10 shows the experimentally determined real and imaginary parts of the permittivity and the refractive index for semi-insulating (SI) InP (sample 7 substrate: Chapter 3). These values are used in the "Radio frequency: Electromagnetic wave, frequency domain" module of COMSOL to calculate the effective mode index of a waveguide with a circular cross section, made of SI InP above a glass substrate ($n_s = 1.5$) for a range of gap sizes and frequencies around $\lambda_0 = 20$ μm, using the "Mode analysis study". The mesh size is chosen so that it is between $\lambda_0/10$ and $\lambda_0/8$ in each simulation domain. Figure 5.11(a) shows the simulated electric field at the cross section of the waveguide. Figure 5.12(a) shows the optical force in piconewtons per μm length of the waveguide per milliwatt input power (pN. $\mu m^{-1} mW^{-1}$) on the waveguide, calculated using the above mentioned method. Figure 5.12(b) shows the optical forces when the SI InP waveguide is substituted with a silicon waveguide ($n_c = 3.5$). No guided mode exists for the waveguide diameters below 5.75 μm and 4.25 μm for the SI

InP and the Si waveguides respectively. Figure 5.13 shows the propagation length of light in the SI InP waveguide calculated from

$$L_m = \frac{1}{2\mathrm{Im}\left[n_{eff}\,\frac{\omega}{c}\right]}. \tag{5.68}$$

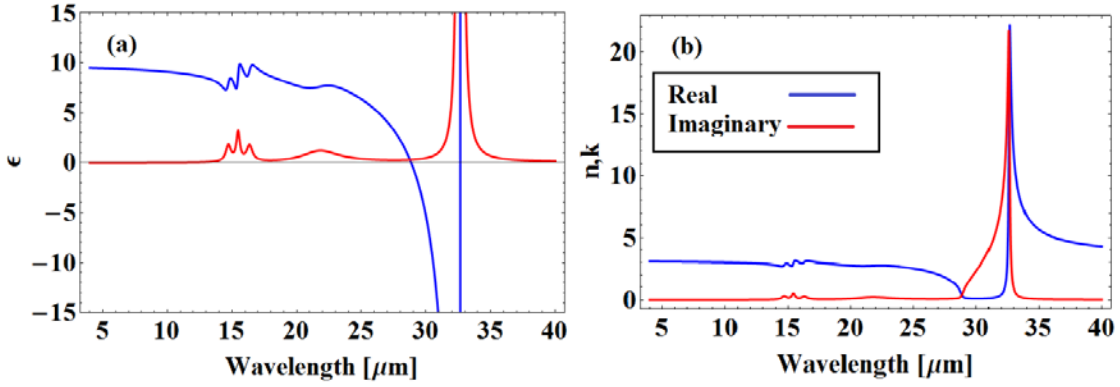

Fig. 5.10 Real and imaginary parts of the (a) permittivity and (b) refractive index of SI InP

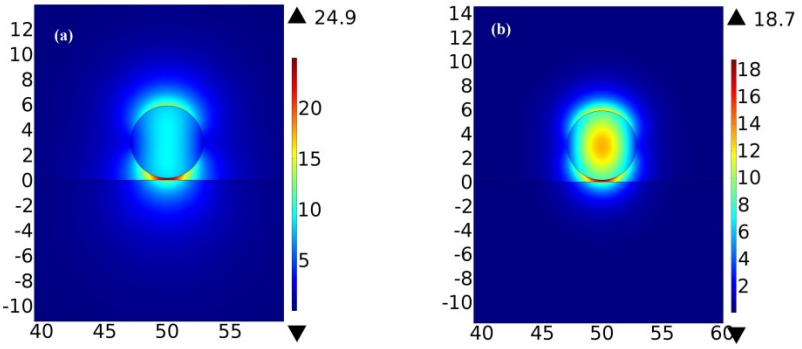

Fig. 5.11 Simulated electric field [V/m] for (a) SI InP waveguide above a glass substrate (b) Si waveguide above a glass substrate at $\lambda_0 = 20$ μm. Spatial dimensions are in μm.

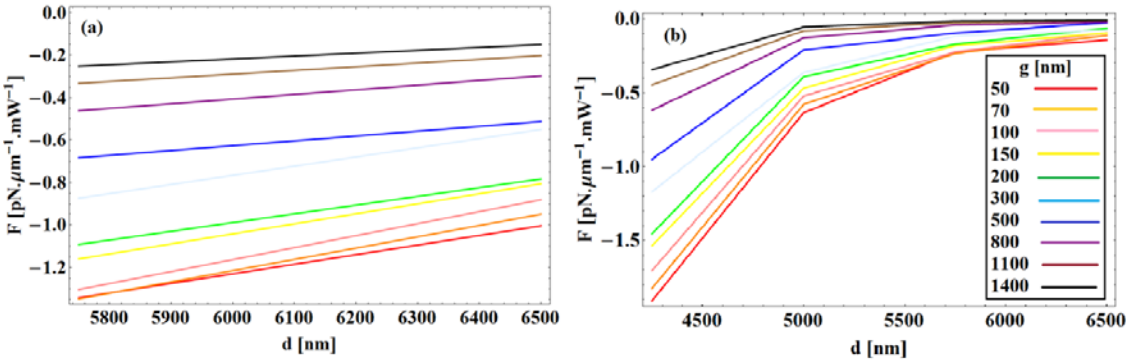

Fig. 5.12 Optical force versus waveguide's diameter for different gap sizes for SI InP waveguide on top of a glass substrate (a) and Si waveguide on top of a glass substrate (b) at $\lambda_0 = 20$ μm.

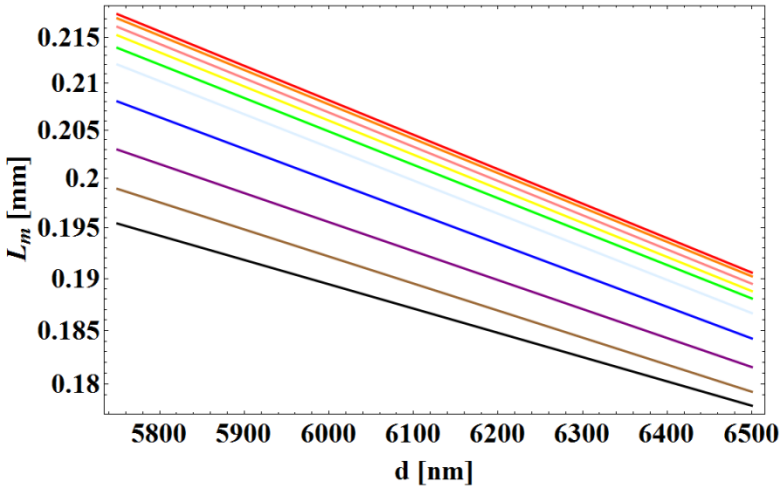

Fig. 5.13 Propagation length versus waveguide's diameter for different gap sizes for SI InP waveguide on top of a glass substrate at $\lambda_0 = 20$ μm. Legend is the same as Fig. 5.12.

In smaller gap sizes, increased field overlap with the lossless substrate will result in lower loss and higher propagation length. In addition, when the waveguide diameter is increased, most of the field will be confined inside the waveguide and affected by losses in SI InP which results in lower propagation length.

5.3. SPP enhanced optical forces

Figure 5.14 shows the experimentally determined real and imaginary parts of the permittivity and the refractive index for highly doped InP:Si (sample 7: Chapter 3). These values are used to calculate the effective mode index of a waveguide with a circular cross section made of SI InP above a InP:Si substrate, using COMSOL, for a range of gap sizes and frequencies around $\lambda_0 = 20$ μm.

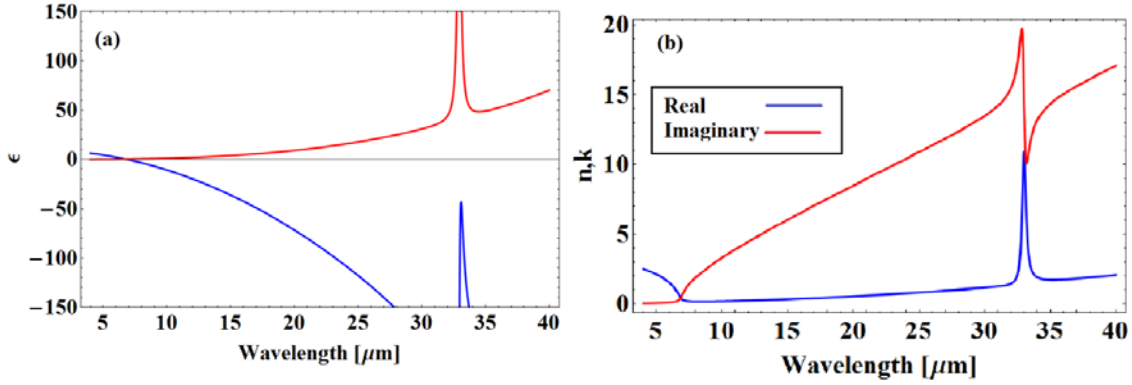

Fig. 5.14 Real and imaginary parts of the (a) permittivity and (b) refractive index of highly doped InP:Si

Figure 5.15 shows the simulated electric field at the cross section of the waveguide. Most of the electric field is confined inside the gap due to the excitation of SPPs. n_{SPP} for SPPs propagating along the interface between air and the substrate, is given by [17]

$$n_{SPP} = \mathrm{Re}\left[\sqrt{\frac{\varepsilon_{substrate}}{\varepsilon_{substrate}+1}}\right]. \tag{5.69}$$

When n_{eff} is close to n_{spp}, the TM polarized input light can excite SPPs on the surface of highly doped InP:Si and this will result in subwavelength confinement of light to the gap between the waveguide and the substrate which gives rise to a hybrid plasmonic guided mode. Figure 5.16 shows n_{eff} as a function of the gap size (g) for different waveguide diameters at $\lambda_0 = 20$ µm. The exerted optical force on the waveguide at $\lambda_0 = 20$ µm is calculated using (5.65) and shown in Fig. 5.17 and the propagation length is shown in Fig. 5.18. In this case, the maximum force of -23.8 $pN.\mu m^{-1}mW^{-1}$ occurs for $d = 3.5$ µm and $g = 50$ nm with a propagation length of 292.86 µm. As the gap size is decreased, high losses in the InP:Si substrate will decrease the propagation length. Decreasing the gap size below 50 nm will increase the force, but this may not be feasible from the fabrication point of view.

Upon coupling to surface plasmons, the force will increase an order of magnitude in comparison to the waveguide above a dielectric substrate in Fig. 5.11, which is the result of the amplified electric field below the waveguide [11].

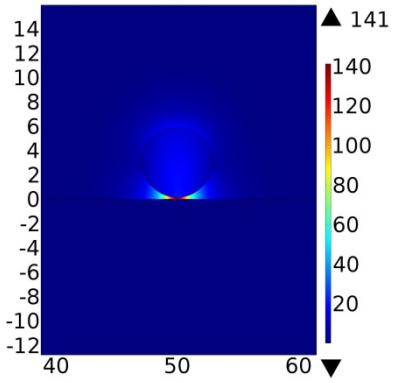

Fig. 5.15 Simulated electric field [V/m] for SI InP waveguide above an InP:Si substrate at $\lambda_0 = 20$ µm. Spatial dimensions are in µm.

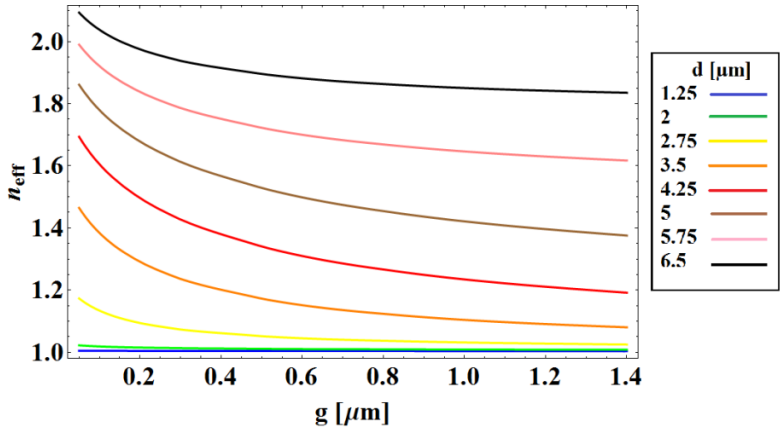

Fig. 5.16 n_{eff} as a function of the gap size for SI InP waveguide above InP:Si substrate with different waveguide diameters at $\lambda_0 = 20$ µm

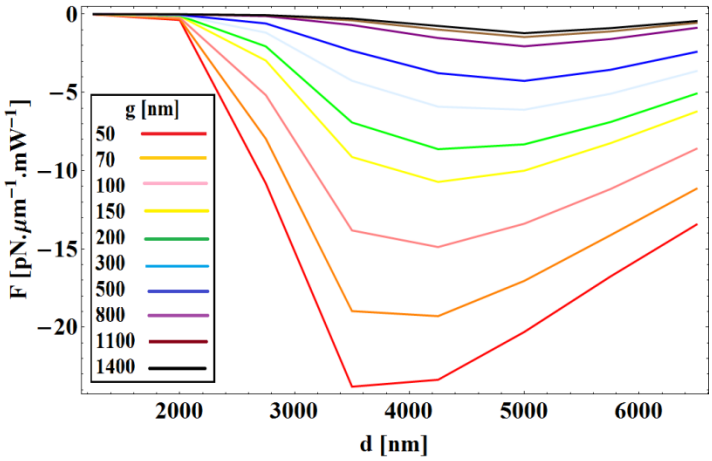

Fig. 5.17 SPP enhanced optical force versus waveguide's diameter for SI InP waveguide above InP:Si substrate with different gap sizes at $\lambda_0 = 20$ µm

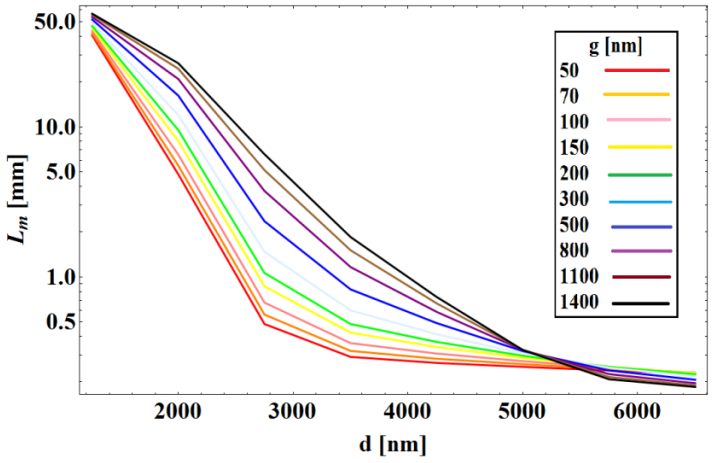

Fig. 5.18 Propagation length vs waveguide's diameter for SI InP waveguide above InP:Si substrate with different gap sizes at $\lambda_0 = 20$ µm

5.4. Phonon enhanced optical forces

According to (5.67), optical forces between the waveguide and the substrate are proportional to $\frac{\partial n_{eff}}{\partial \omega}$. InP has a strong phonon absorption resonance at around 33 μm (Fig. 5.14) that results in very large $\frac{\partial n_{eff}}{\partial \omega}$ which can be used to amplify the optical forces. The physical origin of this amplification is the strong enhancement of the optical near-field coupling by lattice vibrations (phonons) of InP [18]. The optical force is calculated for the SI InP waveguide on top of InP:Si substrate at $\lambda_0 = 32.56$ μm in order to proof this concept. Figure 5.19 shows the simulated electric field at the cross section of the waveguides. Figure 5.20 shows the optical force and figure 5.21 shows the propagation length for this case. A maximum force of -1685 $pN.\mu m^{-1}mW^{-1}$ occurs for $d = 6$ μm and $g = 50$ nm with a propagation length of 466 μm in this case. The force is about three orders of magnitude higher than that for the waveguide above a dielectric substrate, whereas the propagation length is also increased by a factor of two. High propagation length in this case is a result of lower damping in phonon polaritons in comparison to SPPs [18] and also confinement of the field in the air gap instead of the waveguide or the substrate.

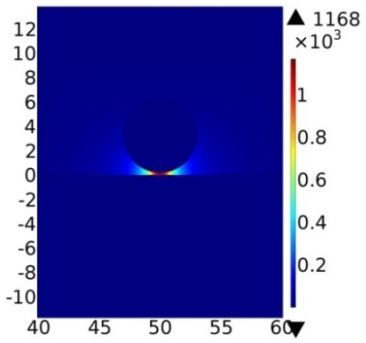

Fig. 5.19 Simulated electric field [V/m] for SI InP waveguide above an InP:Si substrate at $\lambda_0 = 32.56$ μm. Spatial dimensions are in μm.

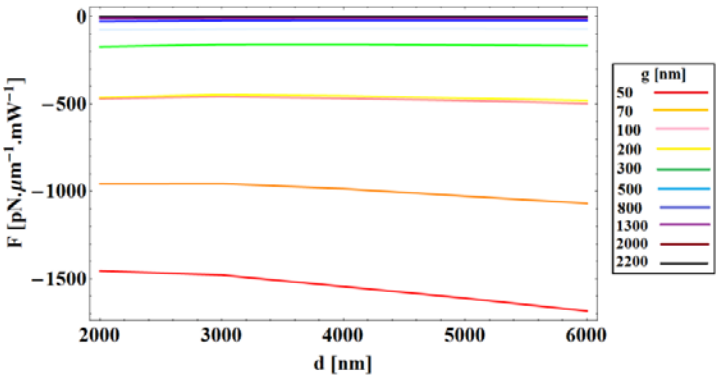

Fig. 5.20 Phonon enhanced optical forces for the SI InP waveguide on top of a InP:Si substrate at $\lambda_0 = 32.56$ μm

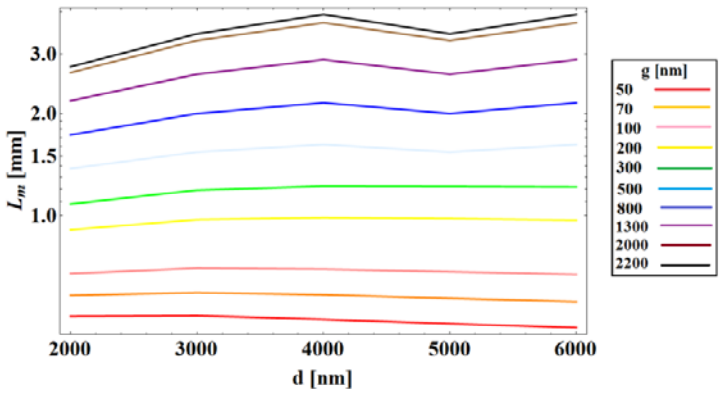

Fig. 5.21 Propagation length for the SI InP waveguide on top of a InP:Si substrate at $\lambda_0 = 32.56$ μm

5.5. Optical forces in the epsilon-near-zero regime

It is intriguing to estimate optomechanical interactions in the ENZ regime, which is appealing for strongly facilitated nonlinear optical effects [19-21]. Forces exerted on electric dipole sources and polarized particles suspended above metamaterials are investigated before, and found to be repulsive in the ENZ regime [22-24]. This effect, which is similar to diamagnetic repulsion, can be used for levitation of particles which is of interest in optofluidics and low friction devices.

The optical forces between a SI InP waveguide and a InP:Si substrate are calculated at $\lambda_0 = 6.8$ μm where the real part of the permittivity of the InP:Si substrate is close to zero ($\mathrm{Re}[\varepsilon_{substrate}] = 0.12$). Figure 5.22 shows the simulated electric field at the cross section of the waveguide. Figure 5.23 shows the force versus the waveguide diameter for different gap sizes, and Fig. 5.24 shows the propagation length. In this case, the resulting positive sign of the force indicates that the force is repulsive, which is a consequence of the positive sign of $\frac{\partial n_{eff}}{\partial g}$ in the epsilon-near-zero (ENZ) regime. This repulsive force can be used to prevent adhesion and stiction in MEMS devices. Another interesting phenomenon which happens in the ENZ regime is that the maximum force of 6.12 $pN.\mu m^{-1}mW^{-1}$ occurs for $g = 100$ nm, and afterwards decreasing the gap size will slightly decrease the force. In this case, unlike all of the former cases, there exists an optimum gap size which results in the maximum repulsive force between the waveguide and the substrate. No guided mode exists for waveguide diameters below 1600 nm when the gap size becomes smaller than 200 nm. In the ENZ regime, InP:Si substrate has higher losses than the SI InP waveguide which results in lower propagation length as the gap size is decreased.

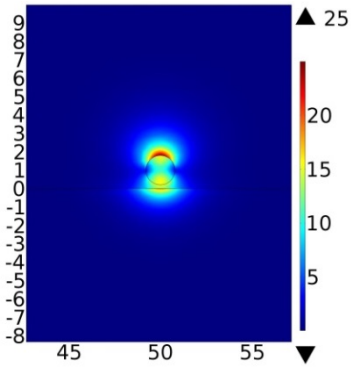

Fig. 5.22 Simulated electric field [V/m] for SI InP waveguide above a InP:Si substrate at $\lambda_0 = 6.8$ µm. Spatial dimensions are in µm.

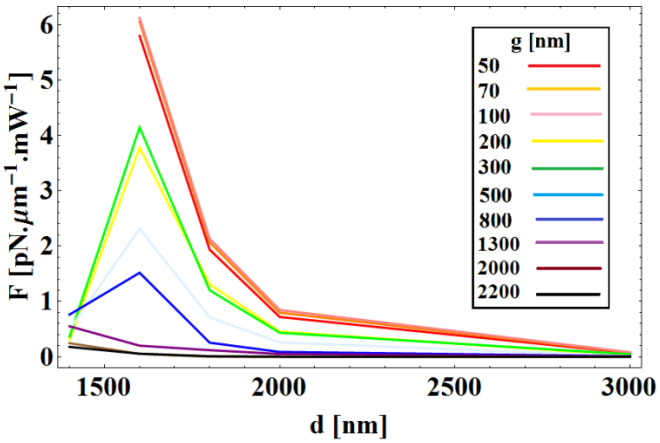

Fig. 5.23 Optical forces for the SI InP waveguide on top of a InP:Si substrate at $\lambda_0 = 6.8$ µm

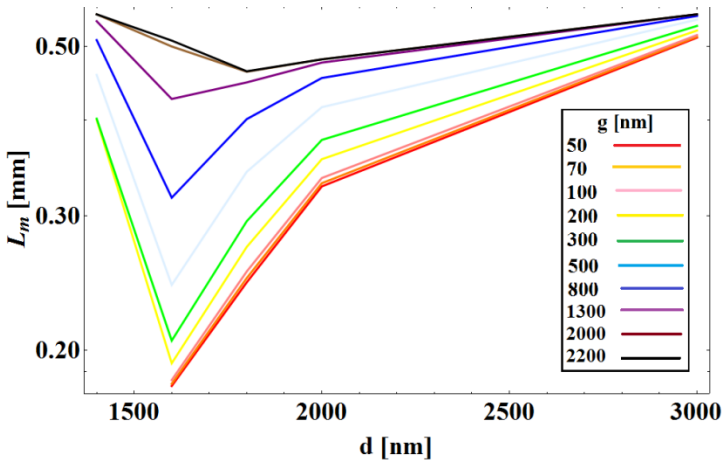

Fig. 5.24 Propagation length for the SI InP waveguide on top of a InP:Si substrate at $\lambda_0 = 6.8$ µm

5.6. Summary

In this chapter we first solved Maxwell equations for a slab waveguide and then generalized the solution to a slab waveguide above a substrate. Afterwards the calculated effective mode indices (n_{eff}) of the slab waveguides were used to find n_{eff} of a waveguide with rectangular cross section above a substrate, using an approximation known as the "effective index method". It was observed that when the dimensions of the waveguide's cross section become smaller than the wavelength of the light, the effective index method fails to comply with the FEM simulation results. Afterwards, Maxwell stress tensor was derived for the waveguide with rectangular cross section above a substrate, in order to find the forces that are exerted upon the waveguide as a result of the coupling of the evanescent tail of the guided modes to the substrate. An alternative method for calculating the force was introduced and used to calculate the force for a Si waveguide and a SI InP waveguide above a glass substrate. Afterwards, the glass substrate was replaced with a highly doped InP:Si substrate and the force was calculated in the SPP excitation wavelength range, in the phonon absorption wavelength and in the ENZ regime. An order of magnitude amplification of the force was observed upon coupling to SPPs and three orders of magnitude amplification was observed when phonons are excited. The force in the ENZ regime was observed to be repulsive and larger than the force for the waveguide above a dielectric substrate. This repulsive force can be applied to prevent stiction of the micro-cantilever to the substrate. The propagation length of the light in the waveguide in all of the above mentioned cases is greater than 15 times the input light's wavelength which is a result of low losses in InP:Si.

Transverse deflection in the middle of a fixed-fixed beam under a line force *F* is given by

$$w = \frac{F\left(\frac{L}{2}\right)^4}{24EI} \tag{5.70}$$

where *L* is the length of the beam, *E* is the Young modulus of the beam's material which is equal to 71 GPa [25] for InP, and *I* is the second moment of area for the beam's cross section which is given by $\frac{\pi}{4}\left(\frac{d}{2}\right)^4$ for a circular cross section. Using the above equation and the forces found in the previous sections, the maximum static deflection of a waveguide with $d = 3.5$ μm and $L = 200$ μm for the SPP enhanced case and the phonon enhanced case are found to be equal to 0.19 and 12.08 nm/mW respectively. Deflection will be much larger for the waveguides with rectangular cross section (e.g. considering the width and the height of the rectangular cross section equal to *d* and *d*/3) due to the larger effective mode area under the waveguide and also smaller second moment of area of the rectangular cross section. In addition, applying a periodic

force using a pulsed input with a frequency close to one of the natural mechanical frequencies of the waveguide will drastically increase the deflection amplitude.

In conclusion, this chapter can be regarded as a proof of concept, showing that InP and similar semiconductors, considering the tunability of their optical properties, can play a key role in optical actuation of MEMS devices.

References

1. H. G. Craighead, "Nanoelectromechanical systems," Science **290**(5495), 1532-1535 (2000).
2. M. Suhonen, J. Graeffe, T. Sillanpää, H. Sipola, and M. Eiden, "Scanning micromechanical mirror for fine-pointing units of intersatellite optical links," Smart Mater. Struct. **10**(6), 1204–1210 (2001).
3. T. Ansbæk, I.-S., Chung, E. S. Semenova, O. Hansen, and K. Yvind, "Resonant MEMS tunable VCSEL," IEEE J. Sel. Topics Quantum Electron. **19**(4), 1702306 (2013).
4. B. Ilic, H.G. Craighead, S. Krylov, W. Senaratne, C. Ober, and P. Neuzil, "Attogram detection using nanoelectromechanical oscillators," J. Appl. Phys. **95**(7), 3694- 3703 (2004).
5. Y. T. Yang, C. Callegari, X. L. Feng, K. L. Ekinci, and M. L. Roukes, "Zeptogram-scale nanomechanical mass sensing," Nano Lett. **6**(4), 583-586 (2006).
6. R. Datar, S. Kim, S. Jeon, P. Hesketh, S. Manalis, A. Boisen, and T. Thundat, "Cantilever sensors: nanomechanical tools for diagnostics," MRS Bull. **34**(6), 449-454 (2009).
7. M. Li, W. H. P. Pernice, C. Xiong, T. Baehr-Jones, M. Hochberg and H. X. Tang, "Harnessing optical forces in integrated photonic circuits," Nature **457**, 480-484 (2008).
8. https://en.wikipedia.org/wiki/Radiation_pressure
9. V. B. Braginskii, and A. B. Manukin, "Ponderomotive effects of electromagnetic radiation," Sov. Phys. JETP, **25**(4), (1967).
10. M. L. Povinelli, M. Lončar, M. Ibanescu, E. J. Smythe, S. G. Johnson, F. Capasso, and J. D. Joannopoulos, "Evanescent-wave bonding between optical waveguides," Opt. Lett. **30**(22), 3042-3044 (2005).
11. M. Li, W. H. P. Pernice, and H. X. Tang, "Broadband all-photonic transduction of nanocantilevers," Nat. Nanotechnol. **4**, 377-382 (2009).
12. M. J. Adams, *An introduction to optical waveguides* (John Wiley & Sons, 1981).
13. COMSOL Multiphysics® v. 5.0. www.comsol.com. COMSOL AB, Stockholm, Sweden.
14. J. D. Jackson, *Classical electrodynamics* (John Wiley & Sons, 1962).
15. W. H. P. Pernice, M. Li, and H. X. Tang, "Theoretical investigation of the transverse optical force between a silicon nanowire waveguide and a substrate," Opt. Express **17**(3), 1806-1816 (2009).
16. F.B. Hildebrand, *Advanced Calculus for Applications* (Prentice-Hall, Englewood, 1976).
17. S. A. Maier, *Plasmonics: Fundamentals and Applications* (Springer, 2007).
18. R. Hillenbrand, T. Taubner and F. Keilmann, "Phonon-enhanced light-matter interaction at the nanometre scale," Nature **418**, 159-162 (2002).

19. M. Z. Alam, I. De Leon, and R. W. Boyd, “Large optical nonlinearity of indium tin oxide in its epsilon-near-zero region,” Science **352**, 795-797 (2016).
20. S. Campione, et al., “Epsilon-near-zero modes for tailored light-matter interaction,” Phys. Rev. Applied **4**, 044011 (2015).
21. L. Caspani, et al., “Enhanced nonlinear refractive index in ε-near-zero materials,” Phys. Rev. Lett. **116**, 233901 (2016).
22. F. J. Rodríguez-Fortuño, A. Vakil, and N. Engheta, “Electric levitation using ε-near-zero metamaterials,” Phys. Rev. Lett. **112**, 033902 (2014).
23. F. J. Rodríguez-Fortuño, and A. V. Zayats, “Repulsion of polarised particles from anisotropic materials with a near-zero permittivity component,” Light Sci. Appl. **5**, e16022 (2016).
24. S. Krasikov, I. V. Iorsh, A. Shalin, and P. A. Belov, “Levitation of finite-size electric dipole over epsilon-near-zero metamaterial,” Phys. Status Solidi RPL **8**, 1015–1018 (2014).
25. www.ioffe.ru

6. CONCLUSION AND OUTLOOK

6.1. Conclusion

In this work silicon doped indium phosphide (InP:Si) is introduced as an alternative plasmonic material for the mid-infrared (mid-IR) range. InP:Si is grown by metal-organic vapor phase epitaxy (MOVPE) using phosphine (PH_3), trimethylindium (TMIn) and disilane (Si_2H_6) as the precursors for phosphorus, indium and silicon respectively. Effect of the growth conditions, namely PH_3 to TMIn (V/III) ratio and disilane flux, on the free carrier concentration is studied. Direct proportionality between the disilane flux and the carrier concentration is observed, up to a threshold point above which the layer morphology will be deteriorated. The doping efficiency is also found to slightly depend on the phosphine to TMIn molar ratio (V/III ratio). A maximum free carrier concentration of 3.87×10^{19} cm^{-3} is achieved and the compensation ratio (ratio of the ionized acceptors to the ionized donor concentration) in all of the grown samples is found to be smaller than the measurement limits.

Reflectance spectra of the samples are measured by Fourier transform infrared spectroscopy (FTIR) and also calculated using the intensity transfer matrix method and the Drude-Lorentz model for the dielectric function of InP:Si. The calculated reflectance spectra are then fitted to the measured ones, using a curve fitting algorithm based on the Levenberg-Marquardt method, in order to find the parameters of the Drude-Lorentz model including the free carriers' plasma frequency and damping. The minimum plasma wavelength of 5.93 μm is achieved. Effective mass of the free electrons in highly doped InP:Si is consequently determined and a semi-empirical formula for the plasma frequency of InP:Si as a function of the free carrier concentration (N) in the range between $0.35\text{-}4\times10^{19}$ cm^{-3} is presented.

The retrieved dielectric function is used to simulate surface plasmon polaritons (SPPs) propagation on flat and structured surfaces, and the simulation results are

verified in direct experiments. SPPs at the top and bottom interfaces of the grown epilayer are excited by the prism coupling technique. Measured SPPs dispersion is in a good agreement with simulations which indicates the accuracy of the fitted dielectric function. An InP:Si grating is fabricated and diffraction of light in different orders is studied. Appearance of the orders prohibited by the conventional Bragg law manifests the efficient SPPs assistance in light diffraction on plasmonic gratings.

In order to demonstrate one of the novel applications of semiconductors in the mid-IR range, optically induced forces exerted upon a semi-insulating InP waveguide suspended above a highly doped InP:Si substrate are investigated, in three different regimes: in the epsilon-near-zero (ENZ) case, with excitation of surface plasmon polaritons (SPPs) and phonons. The above mentioned experimentally determined dielectric function of InP is used in simulations. An order of magnitude amplification of the force is observed when light is coupled to SPPs, and three orders of magnitude amplification is achieved in the phonon excitation regime. In the ENZ regime, the force is found to be repulsive and higher than that in a waveguide above a dielectric substrate. This repulsive force can be used prevent unwanted adhesion of the waveguide to the substrate. Low losses in InP:Si result in a big propagation length. The induced deflection can be detected by measuring the phase change of the light when passing through the waveguide, which enables all-optical functioning, and paves the way towards integration and miniaturization of micro-cantilevers. In addition, tunability of the ENZ and the SPP excitation wavelength ranges, via adjusting the carrier concentration, provides an extra degree of freedom for designing MEMS devices.

Owing to its lower losses, InP:Si shows better performance as a plasmonic material, in terms of the propagation length and localization, in comparison to the other doped semiconductors with a similar plasma frequency. In comparison to noble metals, in the mid-IR range, both real and imaginary parts of the permittivity of InP:Si are two orders of magnitude smaller which leads to better confinement of SPPs in expense of shorter propagation length. Nevertheless, tuanability of the plasma wavelength and damping is a very important feature of semiconductors which cannot be achieved in metals.

6.2. Future works

There may still be room for more investigation of the effect of the growth conditions on the free carrier concentration in InP:Si and possibly increasing it. For example, increasing the growth temperature may slightly increase the free carrier concentration due to improving the cracking efficiency of silane (SiH_4) which is produced by the reaction (2.5). In addition, using other precursors, for example tributyl phosphate (TBP)

for phosphorus, may affect the resulting free carrier concentration. Furthermore, annealing the samples after the growth can affect the doping efficiency and the mobility.

Although the model that is used to calculate the reflectance spectra of the samples, which includes the epilayer and the substrate (epilayer, substrate, air gap and the mirror in case of AZO metamaterials) is enough to retrieve the optical properties of InP (or AZO metamaterials) accurately, but using a more precise model which includes the roughness of the backside of the substrate and the thin carrier diffusion layer between the epilayer and the substrate, will result in more accurate results for other cases to be investigated in future.

The provided library of the electrical and the mid-IR optical properties of InP:Si together with the growth recipes can be useful for design and fabrication of optoelectronic and mid-IR plasmonic devices, including plasmonic waveguides and sensors, which benefit from low losses in InP. In addition, they can be used to design and fabricate single-material low loss metamaterials for mid-IR made of multilayers of doped and undoped InP. One of the advantages of these metamaterials is that they can be grown in a single run using MOVPE and also the fabrication process, for example wet or dry etching, will be facilitated due to the fact that the above mentioned metamaterials consist of a single material.

The optical forces in InP-based waveguides that are theoretically investigated in chapter 5 can be used as a novel actuation method for MEMS devices which enables all optical actuation and detection and paves the way towards miniaturization and integration of these devices.

APPENDIX A

In this section, the computer program which is used to calculate the reflectance spectra of multilayer structures under normal incidence is presented. Wolfram Mathematica 9 is used to develop the program.

Parameters

```
c = 300 000 000 * 10^6; (*μm/s*)
ε0 = 8.85 * 10^-12 (* c^2/Nm^2 *);
εair = 1;
ε∞ = 9.55;
```

Intensity T - matrix method

```
r1[i_, ω_, s_, Γ_, ωf_, γ_, ωp_] := (n[i + 1, ω, s, Γ, ωf, γ, ωp] - n[i, ω, s, Γ, ωf, γ, ωp]) / (n[i + 1, ω, s, Γ, ωf, γ, ωp] + n[i, ω, s, Γ, ωf, γ, ωp]);
r2[i_, ω_, s_, Γ_, ωf_, γ_, ωp_] := (n[i + 1, ω, s, Γ, ωf, γ, ωp] - n[i + 2, ω, s, Γ, ωf, γ, ωp]) / (n[i + 1, ω, s, Γ, ωf, γ, ωp] + n[i + 2, ω, s, Γ, ωf, γ, ωp]);
t1[i_, ω_, s_, Γ_, ωf_, γ_, ωp_] := Sqrt[1 - (r1[i, ω, s, Γ, ωf, γ, ωp])^2];
t2[i_, ω_, s_, Γ_, ωf_, γ_, ωp_] := Sqrt[1 - (r2[i, ω, s, Γ, ωf, γ, ωp])^2];
n[i_, ω_, s_, Γ_, ωf_, γ_, ωp_] := Sqrt[ε[i][ω, s, Γ, ωf, γ, ωp]];
β[i_, ω_, s_, Γ_, ωf_, γ_, ωp_] := 2 π n[i, ω, s, Γ, ωf, γ, ωp] ω / c * 10^12;
ε[1][ω_, s_, Γ_, ωf_, γ_, ωp_] := εair;
ε[2][ω_, s_, Γ_, ωf_, γ_, ωp_] :=
  SetPrecision[ε∞ (1 - ωp^2 / (ω^2 + i ω γ)) + Sum[(s[j] ωf[j]^2) / (ωf[j]^2 - ω^2 - i ω Γ[j]), {j, 1, kk}], Infinity]; (*Epilayer*)
ε[3][ω_, s_, Γ_, ωf_, γ_, ωp_] :=
 SetPrecision[ε∞s (1 - ωps^2 / (ω^2 + i ω γs)) + Sum[(ss[j] ωfs[j]^2) / (ωfs[j]^2 - ω^2 - i ω Γs[j]), {j, 1, kks}], Infinity];
(*Substrate*)
ε[4][ω_, s_, Γ_, ωf_, γ_, ωp_] := εair;

L[1] = 0.516; (*μm*) (*Epilayer*)
L[2] = 363; (*μm*) (*Substrate*)

T[i_, ω_, s_, Γ_, ωf_, γ_, ωp_] :=
  SetPrecision[
   {{1 / (t1[i, ω, s, Γ, ωf, γ, ωp] t2[i, ω, s, Γ, ωf, γ, ωp]
      (e^(-i β[i+1, ω, s, Γ, ωf, γ, ωp] L[i]) - r1[i, ω, s, Γ, ωf, γ, ωp] r2[i, ω, s, Γ, ωf, γ, ωp] e^(i β[i+1, ω, s, Γ, ωf, γ, ωp] L[i])),
```

```
      -1/(t1[i, ω, s, Γ, ωf, γ, ωp] t2[i, ω, s, Γ, ωf, γ, ωp])
       (r1[i, ω, s, Γ, ωf, γ, ωp] e^(i β[i+1,ω,s,Γ,ωf,γ,ωp] L[i]) - r2[i, ω, s, Γ, ωf, γ, ωp] e^(-i β[i+1,ω,s,Γ,ωf,γ,ωp] L[i]))},
     {-1/(t1[i, ω, s, Γ, ωf, γ, ωp] t2[i, ω, s, Γ, ωf, γ, ωp])
       (r1[i, ω, s, Γ, ωf, γ, ωp] e^(-i β[i+1,ω,s,Γ,ωf,γ,ωp] L[i]) - r2[i, ω, s, Γ, ωf, γ, ωp] e^(i β[i+1,ω,s,Γ,ωf,γ,ωp] L[i])),
      1/(t1[i, ω, s, Γ, ωf, γ, ωp] t2[i, ω, s, Γ, ωf, γ, ωp])
       (e^(i β[i+1,ω,s,Γ,ωf,γ,ωp] L[i]) - r1[i, ω, s, Γ, ωf, γ, ωp] r2[i, ω, s, Γ, ωf, γ, ωp] e^(-i β[i+1,ω,s,Γ,ωf,γ,ωp] L[i]))}},
    Infinity];
T2[i_, ω_, s_, Γ_, ωf_, γ_, ωp_] :=
  SetPrecision[
   {{1/(t1[i, ω, s, Γ, ωf, γ, ωp] t2[i, ω, s, Γ, ωf, γ, ωp])
       (e^(-i β[i+1,ω,s,Γ,ωf,γ,ωp] L[i]) - r1[i, ω, s, Γ, ωf, γ, ωp] r2[i, ω, s, Γ, ωf, γ, ωp] e^(i β[i+1,ω,s,Γ,ωf,γ,ωp] L[i])),
     -1/(t1[i, ω, s, Γ, ωf, γ, ωp] t2[i, ω, s, Γ, ωf, γ, ωp])
       (r2[i, ω, s, Γ, ωf, γ, ωp] e^(i β[i+1,ω,s,Γ,ωf,γ,ωp] L[i]) - r1[i, ω, s, Γ, ωf, γ, ωp] e^(-i β[i+1,ω,s,Γ,ωf,γ,ωp] L[i]))},
    {-1/(t1[i, ω, s, Γ, ωf, γ, ωp] t2[i, ω, s, Γ, ωf, γ, ωp])
       (r2[i, ω, s, Γ, ωf, γ, ωp] e^(-i β[i+1,ω,s,Γ,ωf,γ,ωp] L[i]) - r1[i, ω, s, Γ, ωf, γ, ωp] e^(i β[i+1,ω,s,Γ,ωf,γ,ωp] L[i])),
      1/(t1[i, ω, s, Γ, ωf, γ, ωp] t2[i, ω, s, Γ, ωf, γ, ωp])
       (e^(i β[i+1,ω,s,Γ,ωf,γ,ωp] L[i]) - r1[i, ω, s, Γ, ωf, γ, ωp] r2[i, ω, s, Γ, ωf, γ, ωp] e^(-i β[i+1,ω,s,Γ,ωf,γ,ωp] L[i]))}},
    Infinity];
ℜtotal[ω_, s_, Γ_, ωf_, γ_, ωp_] :=
  SetPrecision[(Abs[(T[1, ω, s, Γ, ωf, γ, ωp])[[2, 1]]]/Abs[(T[1, ω, s, Γ, ωf, γ, ωp])[[1, 1]]])^2 +
    ((1/Abs[(T[1, ω, s, Γ, ωf, γ, ωp])[[1, 1]]])^2 (1/Abs[(T2[1, ω, s, Γ, ωf, γ, ωp])[[1, 1]]])^2
      (r1[3, ω, s, Γ, ωf, γ, ωp])^2 e^(-4*2 π Im[√ε[3][ω,s,Γ,ωf,γ,ωp]] L[2]/c ω*10^12))/
     (1 - (Abs[(T2[1, ω, s, Γ, ωf, γ, ωp])[[2, 1]]]/Abs[(T2[1, ω, s, Γ, ωf, γ, ωp])[[1, 1]]])^2 (r1[3, ω, s, Γ, ωf, γ, ωp])^2
      e^(-4*2 π Im[√ε[3][ω,s,Γ,ωf,γ,ωp]] L[2]/c ω*10^12)), Infinity];
```

APPENDIX B

In this section, the computer program which is used to calculate the reflectance spectra of multilayer structures under oblique incidence is presented. Wolfram Mathematica 9 is used to develop the program.

Parameters

```
c = 300 000 000 * 10^6; (*μm/s*)
ε0 = 8.85 * 10^-12 (* c^2/Nm^2 *);
εair = 1;
```

Intensity T - matrix method

```
θinc = 76 * π/180 ;(*Angle of incidence*)
ϕ = 0.92;(*TM polarization percentage*)
```

R_a and T_a

```
NoOfMedia = 3;

ε[1][ω_, s_, Γ_, ωf_, γ_, ωp_, εω_] := εair;
ε[2][ω_, s_, Γ_, ωf_, γ_, ωp_, εω_] := εω (1 - ωp^2/(ω^2 + i ω γ)) + Sum[(s[j] ωf[j]^2) / (ωf[j]^2 - ω^2 - i ω Γ[j]), {j, 1, kk}];
ε[3][ω_, s_, Γ_, ωf_, γ_, ωp_, εω_] := εωs + Sum[(ss[j] ωfs[j]^2) / (ωfs[j]^2 - ω^2 - i ω Γs[j]), {j, 1, kks}];
(*Si substrate*)
ε[4][ω_, s_, Γ_, ωf_, γ_, ωp_, εω_] := 1; (*Air gap*)
ε[5][ω_, s_, Γ_, ωf_, γ_, ωp_, εω_] := 1 - (0.523 * 3622.14^2)/(ω^2 + i * 11.36 * ω); (*Mirror*)


n[i_, ω_, s_, Γ_, ωf_, γ_, ωp_, εω_] := √ε[i][ω, s, Γ, ωf, γ, ωp, εω] ;

θ[1][ω_, s_, Γ_, ωf_, γ_, ωp_, εω_] := θinc;
θ[2][ω_, s_, Γ_, ωf_, γ_, ωp_, εω_] :=
  ArcSin[n[1, ω, s, Γ, ωf, γ, ωp, εω] Sin[θ[1][ω, s, Γ, ωf, γ, ωp, εω]] / n[2, ω, s, Γ, ωf, γ, ωp, εω]];
θ[3][ω_, s_, Γ_, ωf_, γ_, ωp_, εω_] :=
  ArcSin[n[2, ω, s, Γ, ωf, γ, ωp, εω] Sin[θ[2][ω, s, Γ, ωf, γ, ωp, εω]] / n[3, ω, s, Γ, ωf, γ, ωp, εω]];
θ[4][ω_, s_, Γ_, ωf_, γ_, ωp_, εω_] :=
  ArcSin[n[3, ω, s, Γ, ωf, γ, ωp, εω] Sin[θ[3][ω, s, Γ, ωf, γ, ωp, εω]] / n[4, ω, s, Γ, ωf, γ, ωp, εω]];
```

```
L[2] = 1.8;
L[3] = 500;
L[4] = 1;
```

Transverse TM

```
rTrnsTM[i_, ω_, s_, Γ_, ωf_, γ_, ωp_, ϵω_] :=
  (((n[i + 1, ω, s, Γ, ωf, γ, ωp, ϵω]/n[i, ω, s, Γ, ωf, γ, ωp, ϵω])^2 Cos[θ[i][ω, s, Γ, ωf, γ, ωp, ϵω]] -
     Sqrt[((n[i + 1, ω, s, Γ, ωf, γ, ωp, ϵω]/n[i, ω, s, Γ, ωf, γ, ωp, ϵω])^2 - Sin[θ[i][ω, s, Γ, ωf, γ, ωp, ϵω]]^2)])/
   ((n[i + 1, ω, s, Γ, ωf, γ, ωp, ϵω]/n[i, ω, s, Γ, ωf, γ, ωp, ϵω])^2 Cos[θ[i][ω, s, Γ, ωf, γ, ωp, ϵω]] +
     Sqrt[((n[i + 1, ω, s, Γ, ωf, γ, ωp, ϵω]/n[i, ω, s, Γ, ωf, γ, ωp, ϵω])^2 - Sin[θ[i][ω, s, Γ, ωf, γ, ωp, ϵω]]^2)]);

tTrnsTM[i_, ω_, s_, Γ_, ωf_, γ_, ωp_, ϵω_] := Sqrt[1 - (rTrnsTM[i, ω, s, Γ, ωf, γ, ωp, ϵω])^2];

βTrnsTM[i_, ω_, s_, Γ_, ωf_, γ_, ωp_, ϵω_] :=

  2 π n[i, ω, s, Γ, ωf, γ, ωp, ϵω] ω/c Cos[θ[i][ω, s, Γ, ωf, γ, ωp, ϵω]] * 10^12;

TempTrnsTM[ω_, s_, Γ_, ωf_, γ_, ωp_, ϵω_] :=
  {{1, rTrnsTM[1, ω, s, Γ, ωf, γ, ωp, ϵω]}, {rTrnsTM[1, ω, s, Γ, ωf, γ, ωp, ϵω], 1}};

Do[
  TempTrnsTM[ω_, s_, Γ_, ωf_, γ_, ωp_, ϵω_] =
    TempTrnsTM[ω, s, Γ, ωf, γ, ωp, ϵω].{{e^(-i βTrnsTM[i,ω,s,Γ,ωf,γ,ωp,ϵω] L[i]), 0}, {0, e^(i βTrnsTM[i,ω,s,Γ,ωf,γ,ωp,ϵω] L[i])}}.
     {{1, rTrnsTM[i, ω, s, Γ, ωf, γ, ωp, ϵω]}, {rTrnsTM[i, ω, s, Γ, ωf, γ, ωp, ϵω], 1}};,
  {i, 2, NoOfMedia - 1}];

TTrnsTM[ω_, s_, Γ_, ωf_, γ_, ωp_, ϵω_] :=
  (Product_{i=1}^{NoOfMedia-1} (1/tTrnsTM[i, ω, s, Γ, ωf, γ, ωp, ϵω])) * TempTrnsTM[ω, s, Γ, ωf, γ, ωp, ϵω];

RaTM[ω_, s_, Γ_, ωf_, γ_, ωp_, ϵω_] :=
  (Abs[TTrnsTM[ω, s, Γ, ωf, γ, ωp, ϵω][[2, 1]]] / Abs[TTrnsTM[ω, s, Γ, ωf, γ, ωp, ϵω][[1, 1]]])^2;

TaTM[ω_, s_, Γ_, ωf_, γ_, ωp_, ϵω_] := (1 / Abs[TTrnsTM[ω, s, Γ, ωf, γ, ωp, ϵω][[1, 1]]])^2;
```

Transverse TE

```
rTrnsTE[i_, ω_, s_, Γ_, ωf_, γ_, ωp_, ϵω_] :=
  (Sqrt[((n[i + 1, ω, s, Γ, ωf, γ, ωp, ϵω]/n[i, ω, s, Γ, ωf, γ, ωp, ϵω])^2 - Sin[θ[i][ω, s, Γ, ωf, γ, ωp, ϵω]]^2)] -
```

```
      Cos[θ[i][ω, s, Γ, ωf, γ, ωp, εω]]]) /
   (Sqrt[((n[i + 1, ω, s, Γ, ωf, γ, ωp, εω] / n[i, ω, s, Γ, ωf, γ, ωp, εω])^2 - Sin[θ[i][ω, s, Γ, ωf, γ, ωp, εω]]^2]) +
      Cos[θ[i][ω, s, Γ, ωf, γ, ωp, εω]]);

tTrnsTE[i_, ω_, s_, Γ_, ωf_, γ_, ωp_, εω_] := Sqrt[1 - (rTrnsTE[i, ω, s, Γ, ωf, γ, ωp, εω])^2];

βTrnsTE[i_, ω_, s_, Γ_, ωf_, γ_, ωp_, εω_] :=
  2 π n[i, ω, s, Γ, ωf, γ, ωp, εω] ω / c Cos[θ[i][ω, s, Γ, ωf, γ, ωp, εω]] * 10^12;

TempTrnsTE[ω_, s_, Γ_, ωf_, γ_, ωp_, εω_] :=
  {{1, rTrnsTE[1, ω, s, Γ, ωf, γ, ωp, εω]}, {rTrnsTE[1, ω, s, Γ, ωf, γ, ωp, εω], 1}};

  Do[
    TempTrnsTE[ω_, s_, Γ_, ωf_, γ_, ωp_, εω_] =
      TempTrnsTE[ω, s, Γ, ωf, γ, ωp, εω].{{e^(-i βTrnsTE[i,ω,s,Γ,ωf,γ,ωp,εω] L[i]), 0}, {0, e^(i βTrnsTE[i,ω,s,Γ,ωf,γ,ωp,εω] L[i])}}.
       {{1, rTrnsTE[i, ω, s, Γ, ωf, γ, ωp, εω]}, {rTrnsTE[i, ω, s, Γ, ωf, γ, ωp, εω], 1}};,
    {i, 2, NoOfMedia - 1}];

  TTrnsTE[ω_, s_, Γ_, ωf_, γ_, ωp_, εω_] :=
    (Product[1 / tTrnsTE[i, ω, s, Γ, ωf, γ, ωp, εω], {i, 1, NoOfMedia - 1}]) * TempTrnsTE[ω, s, Γ, ωf, γ, ωp, εω];

  RaTE[ω_, s_, Γ_, ωf_, γ_, ωp_, εω_] :=
    (Abs[TTrnsTE[ω, s, Γ, ωf, γ, ωp, εω][[2, 1]]] / Abs[TTrnsTE[ω, s, Γ, ωf, γ, ωp, εω][[1, 1]]])^2;

  TaTE[ω_, s_, Γ_, ωf_, γ_, ωp_, εω_] := (1 / Abs[TTrnsTE[ω, s, Γ, ωf, γ, ωp, εω][[1, 1]]])^2;
```

R_a' and T_a'

Transverse TM

```
  rTrnsTM2[i_, ω_, s_, Γ_, ωf_, γ_, ωp_, εω_] :=
    ((n[i, ω, s, Γ, ωf, γ, ωp, εω] / n[i + 1, ω, s, Γ, ωf, γ, ωp, εω])^2 Cos[θ[i + 1][ω, s, Γ, ωf, γ, ωp, εω]] -
      Sqrt[((n[i, ω, s, Γ, ωf, γ, ωp, εω] / n[i + 1, ω, s, Γ, ωf, γ, ωp, εω])^2 - Sin[θ[i + 1][ω, s, Γ, ωf, γ, ωp, εω]]^2]]) /
    ((n[i, ω, s, Γ, ωf, γ, ωp, εω] / n[i + 1, ω, s, Γ, ωf, γ, ωp, εω])^2 Cos[θ[i + 1][ω, s, Γ, ωf, γ, ωp, εω]] +
      Sqrt[((n[i, ω, s, Γ, ωf, γ, ωp, εω] / n[i + 1, ω, s, Γ, ωf, γ, ωp, εω])^2 - Sin[θ[i + 1][ω, s, Γ, ωf, γ, ωp, εω]]^2]]);

tTrnsTM2[i_, ω_, s_, Γ_, ωf_, γ_, ωp_, εω_] := Sqrt[1 - (rTrnsTM2[i, ω, s, Γ, ωf, γ, ωp, εω])^2];

TempTrnsTM2[ω_, s_, Γ_, ωf_, γ_, ωp_, εω_] :=
  {{1, rTrnsTM2[NoOfMedia - 1, ω, s, Γ, ωf, γ, ωp, εω]},
   {rTrnsTM2[NoOfMedia - 1, ω, s, Γ, ωf, γ, ωp, εω], 1}};

Do[
  TempTrnsTM2[ω_, s_, Γ_, ωf_, γ_, ωp_, εω_] =
    TempTrnsTM2[ω, s, Γ, ωf, γ, ωp, εω].{{e^(-i βTrnsTM[i,ω,s,Γ,ωf,γ,ωp,εω] L[i]), 0}, {0, e^(i βTrnsTM[i,ω,s,Γ,ωf,γ,ωp,εω] L[i])}}.
     {{1, rTrnsTM2[i - 1, ω, s, Γ, ωf, γ, ωp, εω]}, {rTrnsTM2[i - 1, ω, s, Γ, ωf, γ, ωp, εω], 1}};,
```

```
  {i, NoOfMedia - 1, 2, -1}];

TTrnsTM2[ω_, s_, Γ_, ωf_, γ_, ωp_, ϵω_] :=
  (∏_{i=1}^{NoOfMedia-1} (1 / tTrnsTM2[i, ω, s, Γ, ωf, γ, ωp, ϵω])) * TempTrnsTM2[ω, s, Γ, ωf, γ, ωp, ϵω];

RaTM2[ω_, s_, Γ_, ωf_, γ_, ωp_, ϵω_] :=
  (Abs[TTrnsTM2[ω, s, Γ, ωf, γ, ωp, ϵω][[2, 1]]] / Abs[TTrnsTM2[ω, s, Γ, ωf, γ, ωp, ϵω][[1, 1]]])^2;

TaTM2[ω_, s_, Γ_, ωf_, γ_, ωp_, ϵω_] := (1 / Abs[TTrnsTM2[ω, s, Γ, ωf, γ, ωp, ϵω][[1, 1]]])^2;
```

Transverse TE

```
rTrnsTE2[i_, ω_, s_, Γ_, ωf_, γ_, ωp_, ϵω_] :=
  (√((n[i, ω, s, Γ, ωf, γ, ωp, ϵω] / n[i + 1, ω, s, Γ, ωf, γ, ωp, ϵω])^2 - Sin[θ[i + 1][ω, s, Γ, ωf, γ, ωp, ϵω]]^2) -
    Cos[θ[i + 1][ω, s, Γ, ωf, γ, ωp, ϵω]]) /
  (√((n[i, ω, s, Γ, ωf, γ, ωp, ϵω] / n[i + 1, ω, s, Γ, ωf, γ, ωp, ϵω])^2 - Sin[θ[i + 1][ω, s, Γ, ωf, γ, ωp, ϵω]]^2) +
    Cos[θ[i + 1][ω, s, Γ, ωf, γ, ωp, ϵω]]);

tTrnsTE2[i_, ω_, s_, Γ_, ωf_, γ_, ωp_, ϵω_] := √(1 - (rTrnsTE2[i, ω, s, Γ, ωf, γ, ωp, ϵω])^2);

TempTrnsTE2[ω_, s_, Γ_, ωf_, γ_, ωp_, ϵω_] :=
  {{1, rTrnsTE2[NoOfMedia - 1, ω, s, Γ, ωf, γ, ωp, ϵω]},
   {rTrnsTE2[NoOfMedia - 1, ω, s, Γ, ωf, γ, ωp, ϵω], 1}};

Do[
  TempTrnsTE2[ω_, s_, Γ_, ωf_, γ_, ωp_, ϵω_] =
    TempTrnsTE2[ω, s, Γ, ωf, γ, ωp, ϵω].{{e^(-i βTrnsTE[i,ω,s,Γ,ωf,γ,ωp,ϵω] L[i]), 0}, {0, e^(i βTrnsTE[i,ω,s,Γ,ωf,γ,ωp,ϵω] L[i])}}.
     {{1, rTrnsTE2[i - 1, ω, s, Γ, ωf, γ, ωp, ϵω]}, {rTrnsTE2[i - 1, ω, s, Γ, ωf, γ, ωp, ϵω], 1}};,
  {i, NoOfMedia - 1, 2, -1}];

TTrnsTE2[ω_, s_, Γ_, ωf_, γ_, ωp_, ϵω_] :=
  (∏_{i=1}^{NoOfMedia-1} (1 / tTrnsTE2[i, ω, s, Γ, ωf, γ, ωp, ϵω])) * TempTrnsTE2[ω, s, Γ, ωf, γ, ωp, ϵω];

RaTE2[ω_, s_, Γ_, ωf_, γ_, ωp_, ϵω_] :=
  (Abs[TTrnsTE2[ω, s, Γ, ωf, γ, ωp, ϵω][[2, 1]]] / Abs[TTrnsTE2[ω, s, Γ, ωf, γ, ωp, ϵω][[1, 1]]])^2;

TaTE2[ω_, s_, Γ_, ωf_, γ_, ωp_, ϵω_] := (1 / Abs[TTrnsTE2[ω, s, Γ, ωf, γ, ωp, ϵω][[1, 1]]])^2;
```

R_b

Transverse TM and Transverse TE

```
RbTM[ω_, s_, Γ_, ωf_, γ_, ωp_, ϵω_] :=
  (Abs[(1 / (tTrnsTM[3, ω, s, Γ, ωf, γ, ωp, ϵω] * tTrnsTM[4, ω, s, Γ, ωf, γ, ωp, ϵω])) *
       {{1, rTrnsTM[3, ω, s, Γ, ωf, γ, ωp, ϵω]}, {rTrnsTM[3, ω, s, Γ, ωf, γ, ωp, ϵω], 1}}.
        {{e^(-i βTrnsTM[4,ω,s,Γ,ωf,γ,ωp,ϵω] L[4]), 0}, {0, e^(i βTrnsTM[4,ω,s,Γ,ωf,γ,ωp,ϵω] L[4])}}.
        {{1, rTrnsTM[4, ω, s, Γ, ωf, γ, ωp, ϵω]}, {rTrnsTM[4, ω, s, Γ, ωf, γ, ωp, ϵω], 1}})[[2, 1]] /
    Abs[(1 / (tTrnsTM[3, ω, s, Γ, ωf, γ, ωp, ϵω] * tTrnsTM[4, ω, s, Γ, ωf, γ, ωp, ϵω])) *
       {{1, rTrnsTM[3, ω, s, Γ, ωf, γ, ωp, ϵω]}, {rTrnsTM[3, ω, s, Γ, ωf, γ, ωp, ϵω], 1}}.
        {{e^(-i βTrnsTM[4,ω,s,Γ,ωf,γ,ωp,ϵω] L[4]), 0}, {0, e^(i βTrnsTM[4,ω,s,Γ,ωf,γ,ωp,ϵω] L[4])}}.
        {{1, rTrnsTM[4, ω, s, Γ, ωf, γ, ωp, ϵω]}, {rTrnsTM[4, ω, s, Γ, ωf, γ, ωp, ϵω], 1}})[[
      1, 1]]])^2;

RbTE[ω_, s_, Γ_, ωf_, γ_, ωp_, ϵω_] :=
  (Abs[(1 / (tTrnsTE[3, ω, s, Γ, ωf, γ, ωp, ϵω] * tTrnsTE[4, ω, s, Γ, ωf, γ, ωp, ϵω])) *
       {{1, rTrnsTE[3, ω, s, Γ, ωf, γ, ωp, ϵω]}, {rTrnsTE[3, ω, s, Γ, ωf, γ, ωp, ϵω], 1}}.
```

```
        {{e^(-i βTrnsTE[4,ω,s,Γ,ωf,γ,ωp,εω] L[4]), 0}, {0, e^(i βTrnsTE[4,ω,s,Γ,ωf,γ,ωp,εω] L[4])}}.
        {{1, rTrnsTE[4, ω, s, Γ, ωf, γ, ωp, εω]}, {rTrnsTE[4, ω, s, Γ, ωf, γ, ωp, εω], 1}})[[2, 1]]] /
    Abs[(1 / (tTrnsTE[3, ω, s, Γ, ωf, γ, ωp, εω] * tTrnsTE[4, ω, s, Γ, ωf, γ, ωp, εω]) *
       {{1, rTrnsTE[3, ω, s, Γ, ωf, γ, ωp, εω]}, {rTrnsTE[3, ω, s, Γ, ωf, γ, ωp, εω], 1}}.
        {{e^(-i βTrnsTE[4,ω,s,Γ,ωf,γ,ωp,εω] L[4]), 0}, {0, e^(i βTrnsTE[4,ω,s,Γ,ωf,γ,ωp,εω] L[4])}}.
        {{1, rTrnsTE[4, ω, s, Γ, ωf, γ, ωp, εω]}, {rTrnsTE[4, ω, s, Γ, ωf, γ, ωp, εω], 1}})[[
      1, 1]]])^2;
```

ℜtotal

```
ℜtotal[ω_, s_, Γ_, ωf_, γ_, ωp_, εω_] :=
  ϕ
    (RaTM[ω, s, Γ, ωf, γ, ωp, εω] +
      (TaTM[ω, s, Γ, ωf, γ, ωp, εω] TaTM2[ω, s, Γ, ωf, γ, ωp, εω] (RbTM[ω, s, Γ, ωf, γ, ωp, εω]) *
         e^(-4*2 π Im[√ε[NoOfMedia][ω,s,Γ,ωf,γ,ωp,εω]] L[NoOfMedia] ω / c Cos[θ[NoOfMedia][ω,s,Γ,ωf,γ,ωp,εω]]*10^12)) /
       (1 - RaTM2[ω, s, Γ, ωf, γ, ωp, εω] (RbTM[ω, s, Γ, ωf, γ, ωp, εω]) *
          e^(-4*2 π Im[√ε[NoOfMedia][ω,s,Γ,ωf,γ,ωp,εω]] L[NoOfMedia] ω / c Cos[θ[NoOfMedia][ω,s,Γ,ωf,γ,ωp,εω]]*10^12))) +
  (1 - ϕ)
    (RaTE[ω, s, Γ, ωf, γ, ωp, εω] +
      (TaTE[ω, s, Γ, ωf, γ, ωp, εω] TaTE2[ω, s, Γ, ωf, γ, ωp, εω] (RbTE[ω, s, Γ, ωf, γ, ωp, εω]) *
         e^(-4*2 π Im[√ε[NoOfMedia][ω,s,Γ,ωf,γ,ωp,εω]] L[NoOfMedia] ω / c Cos[θ[NoOfMedia][ω,s,Γ,ωf,γ,ωp,εω]]*10^12)) /
       (1 - RaTE2[ω, s, Γ, ωf, γ, ωp, εω] (RbTE[ω, s, Γ, ωf, γ, ωp, εω]) *
          e^(-4*2 π Im[√ε[NoOfMedia][ω,s,Γ,ωf,γ,ωp,εω]] L[NoOfMedia] ω / c Cos[θ[NoOfMedia][ω,s,Γ,ωf,γ,ωp,εω]]*10^12)));
```

APPENDIX C

In this section, the computer program which is used to perform the curve fittings, based on the Levenberg-Marquardt algorithm, is presented. Wolfram Mathematica 9 is used to develop the program.

```
Data

SetDirectory["C:\\Mohammad\\PhD\\Codes\\DL reflection fit\\D1627 fit"];

D1627 = Import["D1627, refined, modified.xlsx"][[1]];

σ = Table[1, {i, Dimensions[D1627][[1]]}];

SetDirectory["C:\\Mohammad\\PhD\\Experiments\\mesm Test71\\D1627"];

Temp = Import["D1627, all points merged.xlsx"][[1]];

Do[If[D1627[[i, 1]] == Temp[[j, 1]], σ[[i]] = Temp[[j, 3]]], {i, 1, Dimensions[D1627][[1]]},
 {j, 1, Dimensions[Temp][[1]]}]

LM fit, second order terms not included in Hessians

NN = Dimensions[D1627][[1]];

kk = 1;
a = Join[Table[s[i], {i, 1, kk}, {j, 1}], Table[Γ[i], {i, 1, kk}, {j, 1}],
   Table[ωf[i], {i, 1, kk}, {j, 1}], Table[γ, {i, 1}, {j, 1}], Table[ωp, {i, 1}, {j, 1}]];

y[ω_, s_, Γ_, ωf_, γ_, ωp_] := SetPrecision[Abs[ℜtotal[ω, s, Γ, ωf, γ, ωp]], Infinity];
χ2[s_, Γ_, ωf_, γ_, ωp_] :=
  SetPrecision[∑_{i=1}^{NN} (1/σ[[i]] (D1627[[i, 2]] - y[c/D1627[[i, 1]] * 10^-12, s, Γ, ωf, γ, ωp]))^2, Infinity];

Needs["NumericalCalculus`"]

aNew = {{2.13}, {0.092}, {9.123}, {2.548}, {45.63}};
ϵ∞ = 9.55;
γ = 2.548;
ωp = 45.63;
s[1] = 2.13;
Γ[1] = 0.092;
ωf[1] = 9.123;

λNew = 0.0001;
aTemp = aNew;
FOM = χLast = χ2[s, Γ, ωf, γ, ωp];
counter = 0;
temp2 = 0;
α = Table[0, {i, 1, Dimensions[a][[1]]}, {j, 1, Dimensions[a][[1]]}];
ββ = Table[{0}, {i, 1, Dimensions[a][[1]]}];
```

```
While[FOM ≥ 10^-20 χLast,
 counter = counter + 1;
 precision = 20;
 Do[
  Do[
   Clear[s, Γ, ωf, γ, ωp];
   Do[If[l ≠ i, s[l] = aTemp[[l, 1]];], {l, 1, kk}];
   Do[If[l + kk ≠ i, Γ[l] = aTemp[[l + kk, 1]]], {l, 1, kk}];
   Do[If[l + 2 kk ≠ i, ωf[l] = aTemp[[l + 2 kk, 1]]], {l, 1, kk}];
   If[3 kk + 1 ≠ i, γ = aTemp[[3 kk + 1, 1]]];
   If[3 kk + 2 ≠ i, ωp = aTemp[[3 kk + 2, 1]]];
   temp = SetPrecision[ND[y[c/D1627[[k, 1]] * 10^-12, s, Γ, ωf, γ, ωp], a[[i, 1]], aTemp[[i, 1]],
      WorkingPrecision → precision, Terms → precision/2], Infinity];
   Clear[s, Γ, ωf, γ, ωp];
   Do[If[l ≠ j, s[l] = aTemp[[l, 1]];], {l, 1, kk}];
   Do[If[l + kk ≠ j, Γ[l] = aTemp[[l + kk, 1]]], {l, 1, kk}];
   Do[If[l + 2 kk ≠ j, ωf[l] = aTemp[[l + 2 kk, 1]]], {l, 1, kk}];
   If[3 kk + 1 ≠ j, γ = aTemp[[3 kk + 1, 1]]];
   If[3 kk + 2 ≠ j, ωp = aTemp[[3 kk + 2, 1]]];
   temp =
    SetPrecision[temp * ND[y[c/D1627[[k, 1]] * 10^-12, s, Γ, ωf, γ, ωp], a[[j, 1]], aTemp[[j, 1]],
       WorkingPrecision → precision, Terms → precision/2], Infinity];
   temp2 = SetPrecision[temp2 + 1/σ[[k]]^2 temp, Infinity];
   , {k, 1, NN}];
  α[[i, j]] = temp2;
  temp2 = 0;
  , {j, 1, Dimensions[a][[1]]}, {i, 1, Dimensions[a][[1]]}];
 If[Det[α] == 0, Print["Singular Hessian; Pseudo-inverse will be used"];];
 Do[
  Clear[s, Γ, ωf, γ, ωp];
  Do[If[l ≠ i, s[l] = aTemp[[l, 1]];], {l, 1, kk}];
  Do[If[l + kk ≠ i, Γ[l] = aTemp[[l + kk, 1]]], {l, 1, kk}];
  Do[If[l + 2 kk ≠ i, ωf[l] = aTemp[[l + 2 kk, 1]]], {l, 1, kk}];
```

```
 If[3 kk + 1 ≠ i, γ = aTemp[[3 kk + 1, 1]]];
 If[3 kk + 2 ≠ i, ωp = aTemp[[3 kk + 2, 1]]];
 ββ[[i, 1]] =
  SetPrecision[(-1/2) ND[χ2[s, Γ, ωf, γ, ωp], a[[i, 1]], aTemp[[i, 1]], WorkingPrecision → precision,
     Terms → precision/2], Infinity];
 , {i, 1, Dimensions[a][[1]]}];
Label[try with larger λ];
αmodified[λ_] :=
 SetPrecision[Table[If[i == j, α[[i, j]] (1 + λ), α[[i, j]]], {i, 1, Dimensions[α][[1]]},
   {j, 1, Dimensions[α][[2]]}], Infinity];
aNew = aTemp + (SetPrecision[PseudoInverse[αmodified[λNew]].ββ, Infinity]);
Do[s[i] = aNew[[i, 1]], {i, 1, kk}];
Do[Γ[i] = aNew[[i + kk, 1]], {i, 1, kk}];
Do[ωf[i] = aNew[[i + 2 kk, 1]], {i, 1, kk}];
γ = aNew[[3 kk + 1, 1]];
ωp = aNew[[3 kk + 2, 1]];
Do[sTemp[i] = aTemp[[i, 1]], {i, 1, kk}];
Do[ΓTemp[i] = aTemp[[i + kk, 1]], {i, 1, kk}];
Do[ωfTemp[i] = aTemp[[i + 2 kk, 1]], {i, 1, kk}];
γTemp = aTemp[[3 kk + 1, 1]];
ωpTemp = aTemp[[3 kk + 2, 1]];
If[χ2[s, Γ, ωf, γ, ωp] ≥ χ2[sTemp, ΓTemp, ωfTemp, γTemp, ωpTemp], λNew = λNew * 10;
  Print[aTemp // N, "  λNew:", λNew // N, "  FOM:", FOM // N, "  χLast:", χLast // N,
   "  Iteration=", counter // N, "   Derivation precision=", precision];
  counter = counter + 1;
  Goto[try with larger λ];
  , λNew = λNew/10; FOM = χ2[sTemp, ΓTemp, ωfTemp, γTemp, ωpTemp] - χ2[s, Γ, ωf, γ, ωp];
  χLast = χ2[sTemp, ΓTemp, ωfTemp, γTemp, ωpTemp];
  aTemp = aNew;
  , λNew = λNew * 10^50;
  Print[aTemp // N, "  λNew:", λNew // N, "  FOM:", FOM // N, "  χLast:", χLast // N,
   "  Iteration=", counter // N, "   Derivation precision=", precision];
  counter = counter + 1;
  Goto[try with larger λ];]
 Print[aTemp // N, "  λNew:", λNew // N, "  FOM:", FOM // N, "  χLast:", χLast // N,
  "  Iteration=", counter // N, "   Derivation precision=", precision];]
```

APPENDIX D

Optical characterization of hyperbolic metamaterials

In this section the method that was explained in chapter 3 is used to find the optical properties of trench structures made of aluminum doped zinc oxide (AZO) slabs in Si or air (Fig. A2). It is shown that the AZO trench structure works as a hyperbolic metamaterial in the mid-infrared (mid-IR) range.

The effective uniaxial permittivity tensor can be defined by $\varepsilon_x = \varepsilon_e$, $\varepsilon_y = \varepsilon_z = \varepsilon_o$ where ε_o and ε_e are the effective ordinary and extraordinary permittivities, respectively. Dielectric function of a 100 nm thick AZO film as well as the ordinary and extraordinary permittivities (ε_o and ε_e) for the trench structures in air and silicon are determined experimentally. In this regard, the intensity transfer matrix method, by which the Fabry-Perot interference fringes from the metamaterial structure or the AZO film will be retained whereas the fringes from the substrate will vanish, is used to calculate the normal incidence reflectance spectra of the metamaterial/substrate system. Drude-Lorentz dielectric function (Eq. 3.12) is used to model the ordinary permittivity of the trench structures. In case of the plain AZO film only the Drude part, and in case of the extraordinary permittivity of the trench structures, as well as the Si substrate, only the Lorentzian terms of the dielectric function are used.

The calculated reflectance spectra are then fitted to the reflectance spectra measured by VERTEX 70 Fourier transform infrared (FTIR) spectrometer from Bruker in order to retrieve the parameters of the dielectric functions. Measurements are done at five different points on each sample and the error bars are considered in the curve fitting algorithm which is based on the Levenberg-Marquardt method.

AZO film

In order to find the optical properties of the AZO film we first need to characterize the 500 μm thick double side polished (DSP) silicon substrate on top of which the films are deposited. Since the IR transmission measurements showed that the DSP Si wafers are transparent in this wavelength range, the spectrometer sample holder's mirror and the airgap below the samples have to be considered in the fitting. Five Lorentzian terms together with ε_∞ are used as the dielectric function of the Si. Fig. A1 (a) shows the measured reflectance spectrum together with the fitted curve and Table A1 shows the fitted parameters for Si. The fitted value for ε_∞ is 12.04. Figure A1 (b) summarizes the real and imaginary parts of the Si permittivity. Although the dispersion of Si is very minute in this wavelength range, it affects the reflectance spectra from samples in some cases. The thickness of the airgap is also fitted and found to be around 8 μm.

Using the retrieved permittivity for the substrate, the curve fitting procedure is done for the 100 nm thick AZO film, considering Drude dielectric function for AZO. Figure A1 (c) shows the measured reflectance spectrum together with the fitted curve for the AZO films and Table A2 summarizes the retrieved parameters of the Drude model. The dips at around 11 and 16.5 μm originate from the absorption in the Si substrate, and 9 and 13.5 μm from SiO_2 on the Si surface. Figure A1 (d) shows the permittivity of the AZO film.

Table A1 Retrieved dielectric function parameters for Si

j	1	2	3	4	5
S_j	0.000389	0.000618	9.81 E-5	0.000136	2.72 E-5
Γ_j [THz]	3.07	1.468	1.37	2.97	0.72
ω_{fj} [THz]	15.24	18.32	22.396	26.69	33.18

Table A2 Retrieved dielectric function parameters for AZO.

γ [THz]	ω_p [THz]	ε_∞
35	147.8	3.45

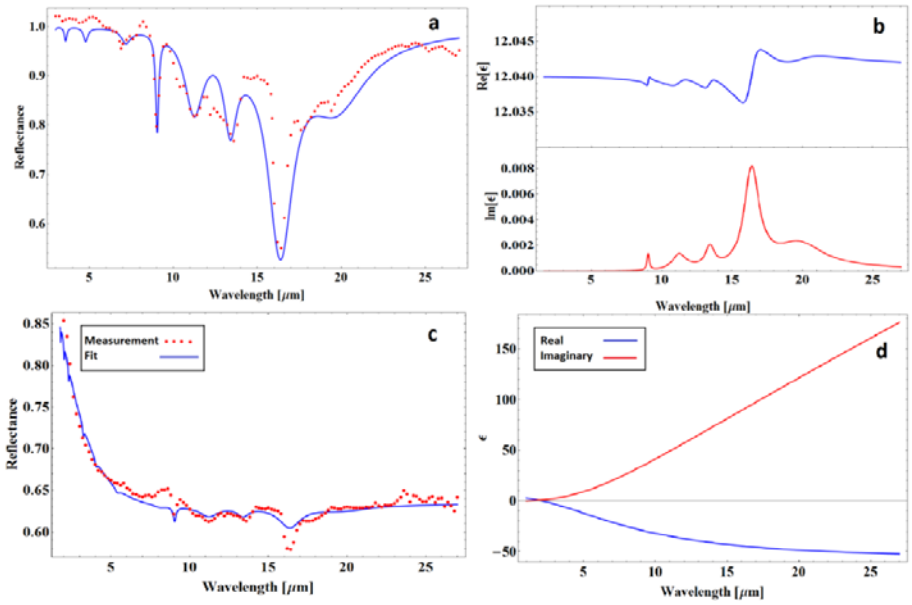

Fig. A1 (a) Measured and fitted reflectance spectra from the Si substrate. (b) Real and imaginary parts of the permittivity of the Si substrate. (c) Measured and fitted reflectance spectra from 100 nm AZO film on DSP Si substrate. (d) Real and imaginary parts of the permittivity of the AZO film.

AZO trench structures

In order to find ε_o and ε_e, reflectance spectra from the samples are measured at 12° angle of incidence using a TE-polarized light with the sample placed such that the electric field is parallel or perpendicular to the trench layers, respectively (Fig. A2).

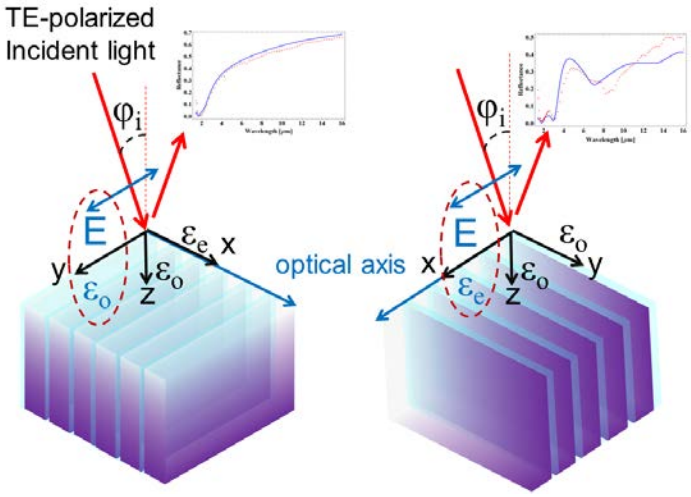

Fig. A2 Orientation of the electric field with respect to the trench layers for measuring ε_o and ε_e.

Drude-Lorentz dielectric function with two Lorentzian terms is used to model the ordinary permittivity of the AZO trench structure in Si (AZO/Si). Figure A3 (a) shows the measured and fitted reflectance spectra for this case. Figure A3 (b) shows the real and imaginary parts of ε_o for AZO/Si structure.

Two Lorentzian terms together with ε_∞ are considered for the extraordinary permittivity of the AZO/Si trench structure. The measured reflectance spectrum together with the fitted curve are shown in Fig. A3 (c). In this case Fabry-Perot oscillations start from 10 µm onwards.

The above-mentioned fitted dielectric functions are used as the permittivity of the 100 nm thick AZO/Si layer underneath the AZO/air trench structure in order to calculate the reflectance spectra and fit them with the measured ones. Drude-Lorentz dielectric function with one Lorentzian term is used to describe the ordinary permittivity of the AZO/air trench structure. Figure A3 (e) shows the measured and fitted reflectance spectra for this case.

Two Lorentzians together with ε_∞ are used to describe the extraordinary permittivity of the AZO/air trench structure. The measured and the fitted reflectance spectra for this case are shown in Fig. A3 (g). The absorption dips originating from the Si substrate are observed at around 9, 11, 13.5, and 16.5 µm and the features below 3

Table A3 Retrieved dielectric function parameters for trench structures.

	S_1	S_2	Γ_1	Γ_2	$\omega_{f,1}$	$\omega_{f,2}$	γ	ω_p	ε_∞
AZO/Si: ε_o	0.23	50.2	4.44	2.87	32.43	7.24	66.02	67.81	8.88
AZO/Si: ε_e	16.74	5.74	76.79	15.84	69.93	31.43	-	-	4.63
AZO/air: ε_o	7.18	-	103.51	-	47.2	-	16.06	84.24	1.6
AZO/air: ε_e	0.283	0.0136	40	9.05	134.63	43.17	-	-	1.24

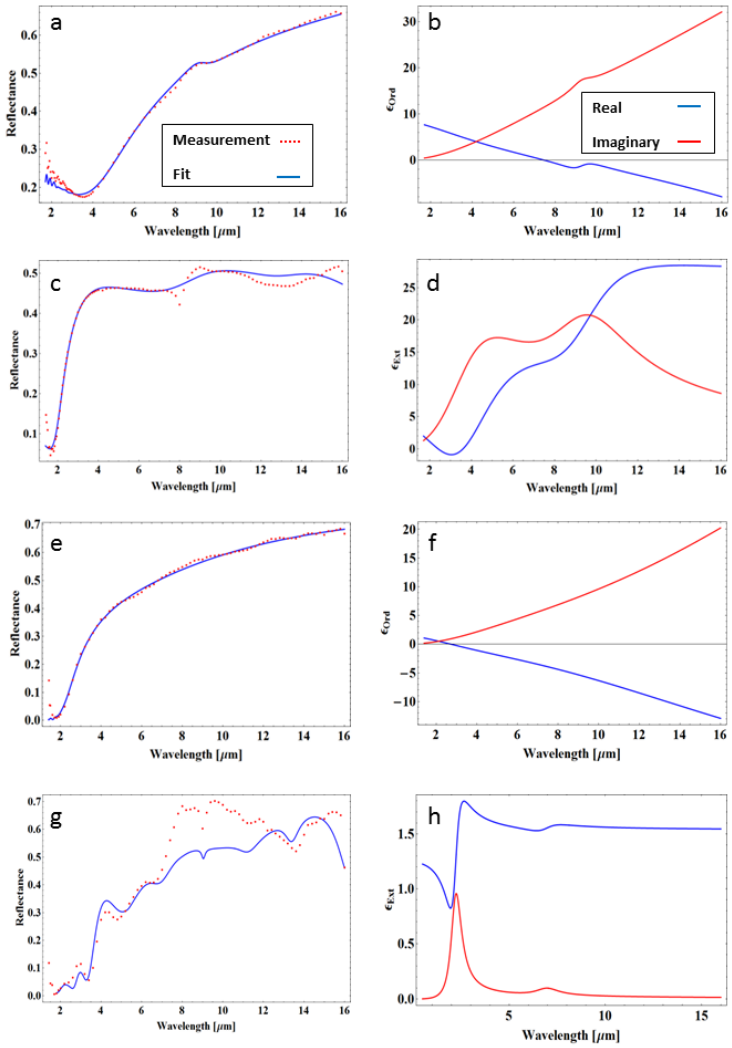

Fig. A3 Measured and fitted reflectance spectra for (a) AZO/Si trench ordinary ε_o, (c) AZO/Si trench extraordinary ε_e, (e) AZO/air trench ordinary ε_o and (g) AZO/air trench extraordinary ε_e together with (b), (d), (f), and (h) their pertaining fitted permittivities.

μm are attributed to Fabry-Perot oscillations. Table A3 summarizes the fitted parameters of the dielectric function of the trench structures.